# Macroscopic Modelling of the Phase Interface in Non-equilibrium Evaporation/Condensation Based on the Enskog-Vlasov Equation

by

Hamidreza Jahandideh

B.Sc., Ferdowsi University of Mashhad, 2016

A Thesis Submitted in Partial Fulfillment of the Requirements for the Degree of

MASTER OF APPLIED SCIENCE

in the Department of Mechanical Engineering

© Hamidreza Jahandideh, 2022
University of Victoria

All rights reserved. This thesis may not be reproduced in whole or in part, by photocopy or other means, without the permission of the author.

Macroscopic Modelling of the Phase Interface in Non-equilibrium Evaporation/Condensation Based on the Enskog-Vlasov Equation

by

Hamidreza Jahandideh

B.Sc., Ferdowsi University of Mashhad, 2016

Supervisory Committee

---

Dr. Henning Struchtrup, Supervisor

(Department of Mechanical Engineering)

---

Dr. Ben Nadler, Committee Member

(Department of Mechanical Engineering)

# Abstract

Considerable jump and slip phenomena are observed at the non-equilibrium phase interface in microflows. Hence, accurate modelling of the liquid-vapour interface transport mechanisms that matches the observations is required, e.g. in applications such as micro/nanotechnology and micro fuel cells. In the sharp interface model, the classical Navier-Stokes-Fourier (NSF) equations can be used in the liquid and vapour phases, while the interface resistivities describe the jump and slip phenomena at the interface. However, resistivities are challenging to find from the measurements, and most of the classical kinetic theories consider them as constants. One possible approach is to determine them from a model that resolves the phase interface.

In order to resolve the interface and the transport processes at and in front of the interface in high resolutions, there are two ways in general, microscopic or macroscopic. The microscopic studies are based either on molecular dynamics (MD) or kinetic models, such as the Enskog-Vlasov (EV) equation. The EV equation modifies the Boltzmann equation by considering dense gas effects, such as the interaction forces between the particles and their finite size. It can be solved by the Direct Simulation Monte Carlo (DSMC) method, which considers sample particles that stand in for thousands to hundred thousands of particles and determine most likely collisions based on interaction probabilities, but it is time-consuming and costly.

Here, a closed set of 26-moment equations is numerically solved to resolve the liquid-vapour interface macroscopically while considering the dense gas and phase change effects.

The 26-moment set of equations is derived by Struchtrup & Frezzotti as an approximation of the EV equation using Grad's moment method. The macroscopic moment equations resolve the phase interface in a high resolution competitive to the microscopic studies. The resolved interface visualizes the interface structure and the changes of the system variables between the two phases at the interface.

The 26-moment equations are solved for a one-dimensional steady-state system for non-equilibrium evaporation/condensation process. Then, solutions are used to find the jump and slip conditions at the interface, which leads to determining the interface resistivities at different interface temperatures and non-equilibrium strengths from the Linear Irreversible Thermodynamics (LIT). The interface resistivities show their dependence on the temperature of the liquid at the interface as well as the strength of the non-equilibrium process.

As a result, in further studies, similar systems can be modelled using the sharp interface method with the appropriate jump conditions at the phase interface that can be found from the determined EV interface resistivities.

# Contents

# List of Tables

# List of Figures

# Nomenclature

## Abbreviations

| | |
|---|---|
| *CE* | Chapman-Enskog |
| *DSMC* | Direct Simulation Monte Carlo |
| *EV* | Enskog-Vlasov |
| *EV*26 | 26-moment set of equations |
| *LIT* | Linear Irreversible Thermodynamics |
| *LTE* | Local Thermodynamic Equilibrium |
| *MD* | Molecular Dynamics |
| *NSF* | Navier-Stokes-Fourier |

## Symbols

| | |
|---|---|
| $A$ | System configuration in the forced evaporation process |
| $a$ | Particle's diameter |
| $B$ | System configuration in the forced evaporation process |
| $b$ | van-der-Waals equation's constant |
| $C$ | Peculiar velocity |
| $c$ | van-der-Waals equation's constant |
| $c_k$ | Microscopic velocity of the particles |
| $\chi_1$ | Power potential order constitutive relation representer |
| $\chi_3$ | Power potential order constitutive relation representer |

| | |
|---|---|
| $\Delta x$ | Finite distance between the two nodes |
| $\Delta$ | Non-equilibrium part of the full trace of 4th moment |
| $\overline{\Delta}$ | Dimensionless non-equilibrium part of the full trace of 4th moment |
| $\Delta T$ | Temperature jump at the interface |
| $\Delta p$ | Deviation of system pressure from saturation pressure |
| $\delta_{ij}$ | Kronecker delta |
| $e_c$ | Condensation probability |
| $\eta$ | Volume ratio |
| $F_k$ | Vlasov force |
| $f$ | Distribution function |
| $f_E$ | Equilibrium distribution function |
| $f_G$ | Grad's distribution function |
| $f_M$ | Maxwellian distribution function |
| $f^*$ | Helmholtz free energy |
| $f_f^*$ | Saturated liquid Helmholtz free energy |
| $f_g^*$ | Saturated vapour Helmholtz free energy |
| $\phi$ | Potential |
| $\phi_a$ | Potential when two particles are tangent |
| $G_k$ | Applied external forces |
| $g$ | Gibbs free energy |
| $g_L$ | Gibbs free energy of the liquid at the interface |
| $g_V$ | Gibbs free energy of the vapour at the interface |
| $g^*$ | Magnitude of the relative velocities of two particles |
| $\gamma$ | Order of the power potential |
| $h_V$ | Enthalpy of the vapour at the interface |
| $J_A$ | Thermodynamic fluxes |
| $J$ | Mass flux |

| | |
|---|---|
| $Kn$ | Knudsen number |
| $k$ | Boltzmann constant |
| $k_k$ | Collision unit vector |
| $L$ | Total length of the system |
| $L_0$ | Length of the liquid |
| $L_l$ | Length of the liquid in MD simulation |
| $L_v$ | Length of the vapour in MD simulation |
| $l_a$ | Average distance between the particles |
| $\lambda$ | Mean free path |
| $\lambda_A$ | Expansion coefficients |
| $m$ | Particle mass |
| $m_{ijk}$ | Trace-free part of the third moments |
| $\overline{m}_{111}$ | Dimensionless trace-free part of the third moments |
| $N$ | Number of prescribed nodes in the discretized system |
| $n$ | Number density |
| $v$ | Specific volume |
| $v_f$ | Saturated liquid specific volume |
| $v_g$ | Saturated vapour specific volume |
| $p$ | Pressure |
| $p_0$ | Standard environmental pressure |
| $p_L$ | Liquid's pressure at the interface |
| $p_{sat}$ | Saturation pressure |
| $p_V$ | Vapour's pressure at the interface |
| $\overline{p}$ | Dimensionless pressure |
| $\prod_{11}$ | Viscous stress in the Navier-Stokes form |
| $Q_k$ | Overall non-convective heat flux |
| $Q_V$ | Overall non-convective heat flux of the vapour at the interface |

| | |
|---|---|
| $q_k$ | Kinetic heat flux |
| $\overline{q}_k$ | Dimensionless kinetic heat flux |
| $R$ | Ideal gas constant |
| $R_{ij}$ | Trace-free part of the single trace of 4th moment |
| $\overline{R}_{11}$ | Dimensionless trace-free part of the single trace of 4th moment (11 components) |
| $r$ | Distance between the two particles |
| $r_{\alpha\beta}$ | Interface resistivities |
| $\rho$ | Mass density |
| $\rho_0$ | Reference mass density |
| $\rho_f$ | Saturated liquid mass density at liquid's temperature of the interface |
| $\rho_g$ | Saturated vapour mass density at liquid's temperature of the interface |
| $\rho_L$ | Mass density of the liquid at the interface |
| $\rho_V$ | Mass density of the vapour at the interface |
| $\bar{\rho}$ | Dimensionless mass density |
| $S$ | Boltzmann collision term |
| $S_{En}$ | Enskog collision term |
| $s$ | Specific entropy |
| $\psi_A$ | Polynomial function |
| $\sigma_S$ | Entropy production |
| $\sigma_{ij}$ | Kinetic stress |
| $\overline{\sigma}_{11}$ | Dimensionless kinetic stress |
| $T$ | Temperature |
| $T_0$ | Standard reference temperature |
| $T_L$ | Liquid's temperature at the interface |
| $T_{LW}$ | Left-boundary temperature |
| $T_{RW}$ | Right-boundary temperature |
| $T_V$ | Vapour's temperature at the interface |

| | |
|---|---|
| $t$ | Time |
| $t_{ik}$ | Overall stress |
| $\Theta$ | Collision angle |
| $\theta$ | Temperature with the specific energy unit |
| $\theta_0$ | Reference temperature with specific energy unit |
| $\theta_L$ | Temperature of the liquid at the interface with specific energy unit |
| $\theta_{LW}$ | Left-wall controlled temperature with specific energy unit |
| $\theta_{RW}$ | Right-wall controlled temperature with specific energy unit |
| $\theta_V$ | Temperature of the vapour at the interface with specific energy unit |
| $\bar{\theta}$ | Dimensionless temperature with specific energy unit |
| $U_A$ | Moment |
| $u$ | Specific internal energy |
| $v$ | Macroscopic velocity |
| $\bar{v}$ | Dimensionless macroscopic velocity |
| $\vartheta$ | Arbitrary variable |
| $w_k$ | Magnitude of the relative velocity |
| $X_A$ | Thermodynamic forces |
| $x_k$ | Location in the space |
| $Y$ | Correlation function |

# Aknowledgment

Firstly, I would like to express my deepest appreciation to my supervisor, Dr. Henning Struchtrup, for his encouragement, guidance, patience, and support. This project would not have been possible without his assistance. I must also thank my committee member, Dr. Ben Nadler, for his helpful advice, practical suggestions, and support. I am also grateful to Dr. Boualem Khouider for his participation in examining my thesis.

Secondly, I'm deeply indebted to my parents and my brother, Ahmad Jahandideh, for supporting me over the years. Finally, my special thanks to Ayda Mirzarasoulzadeh for her companionship over the past years.

# Dedication

To my parents

Mohammadreza Jahandideh

Maryam Shaleh

# Chapter 1

# Introduction

Evaporation and condensation are important phenomena found everywhere in nature and technology [1]. Many attempts have been made to develop the models and theories of evaporation/condensation to describe it for over a century [1–5]. These attempts led to finding models and theories of evaporation/condensation, such as the classical hydrodynamic [1]. However, knowledge about the transport mechanisms and changes of the variables from one phase to another at the interface is limited [1]. Modelling the phase interface in the evaporation/condensation process is challenging because each phase has its properties that need to be considered [6, 7]. Based on the classical hydrodynamic, it often is assumed that either no or no considerable discontinuities exist between the liquids and vapour variables at the interface, even in the non-equilibrium state [8]. It is primarily based on speculations rather than experimental data or computer simulations [1].

The limitations of this assumption have become evident from some experiments that found the considerable temperature jump at the phase interface in the non-equilibrium state [1–3].

For instance, experiments performed by Ward, Fang, and Stanga showed a significant temperature jump between the two phases at the liquid-vapour interface of a water droplet in the steady-state evaporation process [9–11]. For this experiment, Ward et al. used the

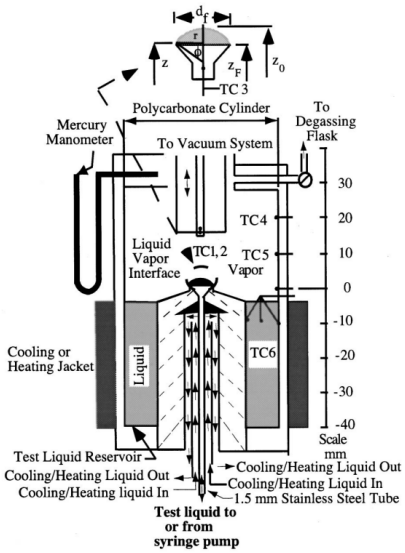


(a)

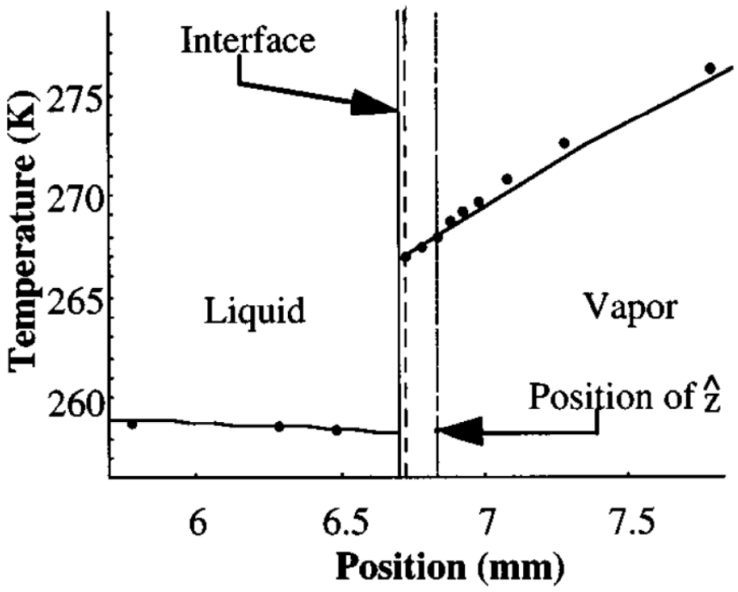


(b)

Figure 1.1: (a) The apparatus used by Ward et al. to measure the temperature jump at the water droplet interface in a steady-state evaporation process [9]. (b) The considerable temperature jump of around $7.8K$ measured at the liquid-vapour interface in the steady-state evaporation process in the Ward et al.'s experiments [10].

apparatus shown in Figure 1.1a to create a liquid droplet resting in a funnel connected to a liquid reservoir to accurately measure the temperatures of the two phases at the water droplet interface in the steady-state evaporation process [9]. Figure 1.1b shows the noticeable temperature jump of around $7.8K$ at the liquid-vapour interface, such that the vapour is at a higher temperature than the liquid. However, as mentioned above, the classical hydrodynamics assumes zero jumps at the interface.

Also, studies based on classical kinetic theory with simple jump conditions at the interface [12–15] predicted a temperature jump of about $2.7 \times 10^{-2}K$, and the liquid was predicted at a higher temperature than the vapour [10]. This temperature jump prediction was considerably smaller and in the opposite direction than the experimental results [1].

Hence, neither the classical hydrodynamics nor the classical kinetic theory can be used for modelling jump and slip conditions at the interface. Models that show a better picture of the liquid-vapour interface transport mechanisms by taking a more detailed and closer look at the liquid-vapour interface are required.

Having an accurate model of the liquid-vapour interface is essential not only from the fundamental point of view but also for various applications, such as the design and optimization of the micro-channels, cooling microsystems [16], micro fuel cells [17, 18] and other small-scale systems.

## 1.1 Phase Equilibrium vs Non-Equilibrium

In order to model the system appropriately to study the changes at the interface, it is essential to have a clear understanding of the equilibrium state and the non-equilibrium evaporation/condensation state.

The studied system is one-dimensional, and variables change only in the $x$ direction. Figure 1.2a shows the closed 1-D system containing a substance in both liquid and vapour phases, and the boundaries are kept at the same temperature $T_W$, so that the system is in

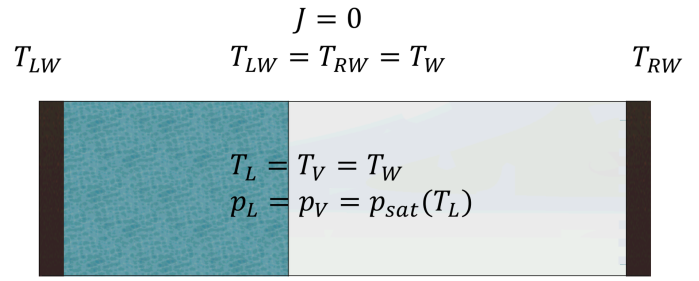


(a)

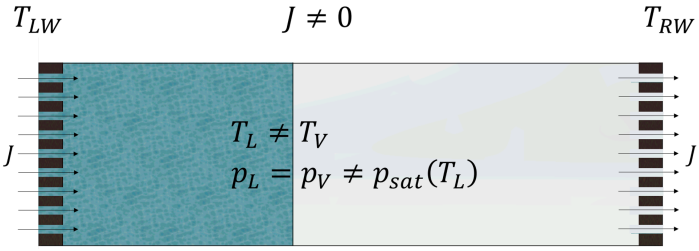


(b)

Figure 1.2: (a) The 1-D system in the global phase equilibrium. It is closed, and the temperatures of the two sides are identical. The temperature is homogeneous, the pressure is constant and equal to the saturation pressure at the homogeneous temperature. (b) The 1-D system in the non-equilibrium state. It is opened, and the vapour is pumping out so that the steady-state evaporation process occurs at the interface. The temperature is not homogeneous. At the interface, the temperatures of the two phases are not the same, and the system pressure deviates from the equilibrium state.

the global equilibrium state. In this phase equilibrium, the temperature is homogeneous, which implies the same temperatures for both phases at the interface. The pressures of the two phases are identical and equal to the saturation pressure at the homogeneous temperatures $p_{sat}(T_W)$. The liquid and vapour have different homogeneous mass densities. Hence, the mass density changes from the liquid to the vapour at the interface. In general, the interface has a thickness of a few particle diameters. As a result, depending on the scale of the resolution of the interface, the mass density changes appear as a jump or steep continuous changes.The continuous changes can be found when the system is resolved in high resolutions.

Lowering the vapour pressure from the saturation pressure creates a non-equilibrium state in the system, and evaporation occurs to increase the pressure to its equilibrium value. Therefore, as shown in Figure 1.2b, a non-equilibrium steady-state evaporation process occurs when the mass flux $J$ of the vapour is pumped out from the system. In order to have the steady-state evaporation process similar to the Ward et al. experiments [9–11], the same mass flux $J$ is added to the liquid side to keep the total mass inside the system constant.

To maintain the lower pressure leading to the non-equilibrium evaporation process, it is required to keep pumping out the vapour.

The non-equilibrium system's pressure deviates from the saturation pressure $p_{sat}(T_L)$, such that the pressure deviation $\Delta p = p - p_{sat}(T_L)$ occurs in the system. For the evaporation process, the heat of evaporation is drawn from the phase interface; as a result, the temperature is inhomogeneous, and in general, the interface becomes colder than the equilibrium temperature $T_W$. As it is observed in the experiments, the liquid and vapour phases have different temperatures at the interface, which leads to the temperature jump $\Delta T = T_V - T_L$ at the interface, and it needs to be considered in models.

However, in classical hydrodynamics, these jump and slip conditions are ignored. Also, studies based on classical kinetic theory could not predict the jump and slip conditions in the agreement with the observations [1, 10].

The system is in a highly non-equilibrium state when the thermodynamic fluxes such as mass flux or heat flux are relatively large. Only slight deviations from the equilibrium are observed when the fluxes are small.

This research intends to model the jump and slip conditions to find a better agreement with the experiment [9–11]. The jump and slip conditions are noticeable and need to be considered in the small-scale system, where the total length of the system is on the order of hundred particle diameters. It will be seen that the large heat flux implies a large jump. For instance, in Ward et al.'s experiment [9–11], the considerable temperature jump was observed because of the large heat flux at the phase interface caused by the geometry of the system.

## 1.2 Sharp Interface Method

The thickness of the interface is small, and changes of the variables at the interface can be considered as jumps like the temperature changes observed in the experiments, see Figure 1.1b. The sharp interface method is a way for studying the process by considering the jump and slip conditions at the interface based on Linear Irreversible Thermodynamics (LIT).

The LIT describes the transport processes in the systems not in the global equilibrium. It assumes that the liquid and vapour are in the Local Thermodynamic Equilibrium (LTE) [19]. Therefore, it is assumed that the NSF equations are valid in both phases, while the jump and slip conditions need to be determined and considered at the interface.

Based on the LIT, the interface is modelled in a non-equilibrium evaporation/condensation process by formulating the entropy production at the interface. For this, the conservation laws of mass, momentum and energy are used together with the Gibbs equation to formulate the entropy production with the jump and slip conditions at the phase interface, see Sec. 5.1.

Then, based on the LIT, the thermodynamic fluxes and forces are related linearly with

the matrix of interface resistivities $r_{\alpha\beta}$. A detailed description of the LIT can be found in [20–23]. For small deviations from the equilibrium state, the LIT formulation reads [24, 25]

$$\begin{bmatrix} -\left(1-\frac{\rho_g}{\rho_f}\right)\frac{\Delta p}{\sqrt{2\pi RT_L}} \\ -\frac{\rho_g}{\sqrt{2\pi RT_L}}\Delta T \end{bmatrix} = \begin{bmatrix} r_{11} & r_{12} \\ r_{21} & r_{22} \end{bmatrix} \begin{bmatrix} J \\ \frac{Q_V}{RT_L} \end{bmatrix}, \tag{1.1}$$

where $\rho_f$ and $\rho_g$ are the saturated liquid and the saturated vapour mass densities at the liquid's temperature of the interface $T_L$, respectively. Also, $Q_V$ is the overall non-convective heat flux in the vapour phase at the interface. The equation (1.1) is constructed such that the second law of thermodynamics is obeyed at all times, which requires the positive definiteness of the resistivities matrix.

The dimensionless matrix of interface resistivities $r_{\alpha\beta}$ linearly connects the mass and heat fluxes with the temperature jump $\Delta T = T_V - T_L$ and the deviation of the system's pressure from the saturation pressure of the liquid at the interface $\Delta p = p - p_{sat}(T_L)$.

The sharp interface method can be used only when the interface resistivities values are available as an additional input for calculating the temperature jump and the pressure deviation from equation (1.1). However, the resistivities are challenging to determine, and the macroscopic thermodynamics can not predict them.

Some studies have been done to determine the interface resistivities based on classical kinetic theory using the LIT and the solutions of the Boltzmann equation with simple interface jump conditions, and the studies found the symmetric matrix of resistivities as [12, 26–28]

$$r_{\alpha\beta} = \begin{bmatrix} \frac{1}{e_c} - 0.40044 & 0.126 \\ 0.126 & 0.294 \end{bmatrix}, \tag{1.2}$$

where $e_c$ is the condensation probability at the interface which is typically considered as a constant [2]. The interface resistivities in (1.2) are not dependent on the temperature

of the interface, and they do not give the jump and slip conditions in agreement to the experiments.

Hence, a full picture of the interface resistivities that shows their dependence on the system properties, particularly the interface temperature, is required.

The resistivities can be determined from the measurements. However, due to the smallness of the interface thickness, measuring the system's variables of the two phases at the interface is challenging and almost impossible.

Instead of the measurements, resolving the system in high resolutions that give steep and continuous changes of the variables at the interface. The resolved solutions can be used to find the jumps and slip conditions and determine the interface resistivities from the LIT.

Hence, it is required to resolve the interface in high resolutions on the order of particle diameter.

## 1.3 Liquid, Interface, Vapour

Defining the different length scales in the system that we are interested in is helpful to understand how the flow can be resolved in high resolutions. It also clarifies why the jump and slip conditions become considerable in small-scale systems.

The first scale number is the gas particle's diameter $a$ which is typically on the order of

$$a = (2, \cdots, 6) \times 10^{-10} m. \tag{1.3}$$

The next length scale is the average distance between the particles $l_a$

$$l_a = \sqrt[3]{\frac{1}{n}} = \sqrt[3]{\frac{m}{\rho}}, \tag{1.4}$$

where $n$ is the number density.

For air as an ideal gas under standard conditions $(p_0 = 1bar, T_0 = 298K)$

$$l_a = \sqrt[3]{\frac{kT_0}{p_0}} = 3.452 \times 10^{-9} m, \tag{1.5}$$

where $k = 1.38066 \times 10^{-23} \frac{J}{K}$ is the Boltzmann constant.

As found in equation (1.4), the order of the magnitude of $l_a$ depends on the density. In dense vapour, the distance between the particles is smaller than the calculated value for the air as an ideal gas in (1.5). In liquids, where the molecules are in contact, $l_a$ is on the same order as the particles' diameter.

The average distance between the particles is also important in considering the appropriate equation of state for the different flows. In dense vapour, the mass density is larger than the dilute gases, such that the ideal gas law does not hold, and an equation of state that considers the particles' interactions and their finite size is required. For example, the van-der-Waals equation of state [29] is a simple and instructive equation that considers real gas effects

$$p = \frac{RT}{\frac{1}{\rho} - b} - c\rho^2, \tag{1.6}$$

where the constant $b$ defines the reduction of the accessible volume due to the finite size of the particles, and the constant $c$ accounts for the reduction of the pressure due to the attractive forces between the particles. For sufficiently small mass densities as observed in the systems with low pressures or large temperatures, the van-der-Waals equation simplifies to the ideal gas equation.

The third scale is the mean free path $\lambda$, which is the average distance that a gas particle travels freely between the two collisions. For an ideal gas of hard-sphere particles, under the standard conditions, the mean free path is on the order of [30]

$$\lambda = \frac{m}{\sqrt{2}\pi a^2 \rho} = 2.31 \times 10^{-7} m \cdots 2.57 \times 10^{-8} m. \tag{1.7}$$

To find the mean free path of the dense vapour, a correction for the particle sizes should

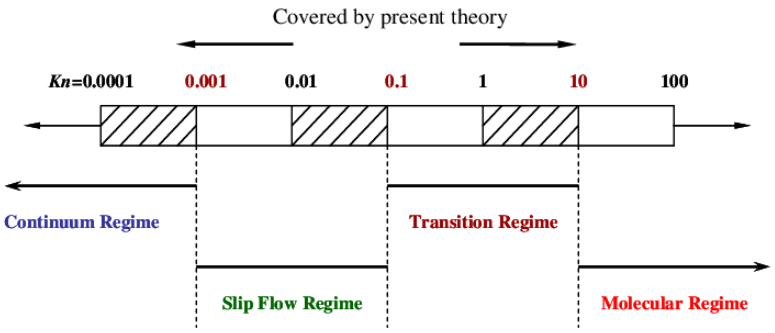


Figure 1.3: The classifications of the flow regimes in the microchannels as a small-scale system [31].

be included.

Similar to the average distance $l_a$, the mean free path depends on the mass density so that it is considerably smaller in dense vapours than in the ideal gases. In contrast, at low pressures, the mean free path is greater than in the ideal gases.

The Knudsen $Kn$ number is defined as the ratio between the mean free path and a typical characteristic length of the system $L$

$$Kn = \frac{\lambda}{L}. \tag{1.8}$$

The Knudsen number determines the transport properties of the flow, and according to the length scales of the system, one considers the following regimes, see Figure 1.3

- Continuum regime: The Knudsen number is small, e.g., approximately less than $10^{-3}$ in the vapour, and the NSF equations are valid for describing the flow.

- Slip regime: The jump and slip conditions need to be considered at the phase interfaces, while the classical NSF equations are still valid for the pure phases. For the vapour phase, the slip regime occurs when the Knudsen number is approximately from $10^{-3}$ to $10^{-1}$.

- Transition regime: The Knudsen number is relatively large, e.g., approximately from

$10^{-1}$ to 10 in the vapour. The particles' interactions and their finite size start to affect the flow. In this regime, the classical NSF equations are not valid and need to be modified.

- Free molecular regime: The Knudsen number is large, e.g., approximately greater than 10 in the vapour. The flow properties depend strongly on the particles' motions and collisions.

The following cases are the well-known conditions, with relatively large $Kn$ numbers [30]

- In the rarefied gas, the vacuum flows, due to the low number density, the mean free path $\lambda$ is large, so that even for the considerable system lengths such as a space shuttle, the Knudsen number $Kn$ is large.

- In the micro/Nano flows systems that we are interested in modelling them in this research, the small system's length leads to a relatively large Knudsen number even for the small mean free paths, especially at relatively low pressures.

The length scales are advantageous in dividing the small-scale system into the three regions, see Figure 1.4a. Understanding the physical length scales in each of the following regions is helpful to consider the appropriate model for modelling the system.

- Liquid bulk region: The substance is in the liquid phase only, the particles are in contact, the microscopic effects are negligible.

- Interface region: From the liquid to vapour, the interface has a thickness of a few particle diameters. When the characteristic length is on the order of the particle diameter, the particles' interactions and their finite size become considerable and resolving the interface in high resolutions is required. The resolved liquid-vapour interface shown in Figure 1.4b, shows the steep but continuous changes of the mass density. The resolved mass density curve in Figure 1.4b shows the interface structure. Taking a look at the resolved temperature shows more complicated steep and continuous changes

at the interface that extend into the vapour region according to the interface structure, which creates an overall jump effect. The small distance in front of the interface on the vapour side defines the transitions layers, known as the Knudsen layers. It will be presented in the next chapters that how the interface is resolved and the temperature or mass density curves are obtained. The thickness of the Knudsen layers depends on the pressure. At the low temperatures, due to the larger mean free path, it will be wider, while in higher pressures and smaller mean free paths, it is thinner. Hence, in high-resolution studies, particles' interactions and their finite size at the interface and in transition layers in front of it are considerable.

- Vapour bulk region: As shown in Figure 1.4, the vapour bulk phase is in front of the Knudsen layers, and no steep deviations of the temperature are seen anymore. In the bulk vapour region, the microscopic effects are negligible.

## 1.4 Resolving the Interface

The small-scale system is dense in all three regions. The liquid-interface-vapour system needs to be resolved to show how the system's variables change from liquid to vapour across the interface in the non-equilibrium evaporation/condensation process.

Resolving the system is possible using the Molecular Dynamics (MD) method, which studies the system microscopically by considering every particle. Figure 1.5 shows a Molecular Dynamics simulation of a non-equilibrium evaporation system that contains both liquid and vapour phases with the lengths of $L_l$ and $L_v$, respectively, done by Heinen & Vrabec [32]. The length of the vapour considered $L_v = 400$ relative to the particle diameter $a$, and the liquid had a length of around $L_l = 35$ [32]. It was connected to the liquid reservoir on the left side, which kept the liquid length stationary by replacing the evaporated liquid [32].

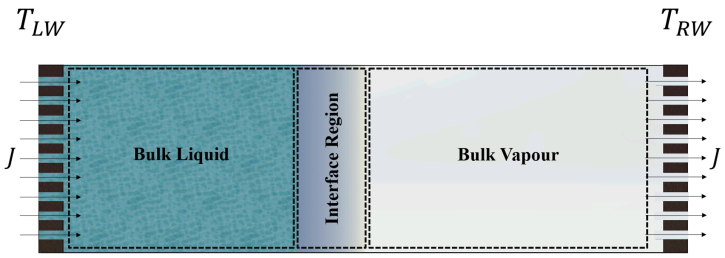


(a)

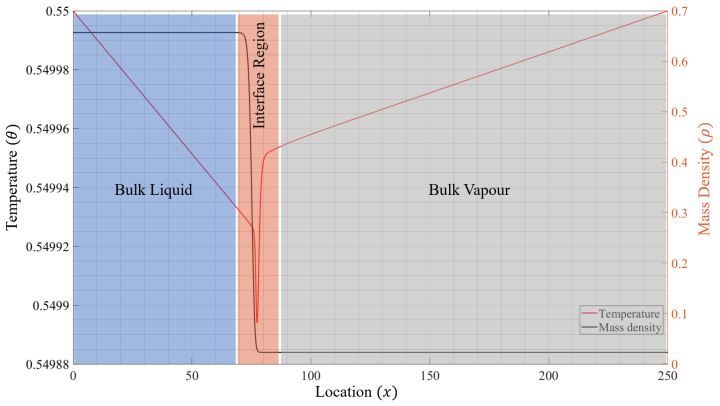


(b)

Figure 1.4: (a) The divided system into the three regions with different importance of the real-gas effects. (b) Resolved mass density and temperature curves in the system for non-equilibrium evaporation process that are found by resolving the interface in high resolution.

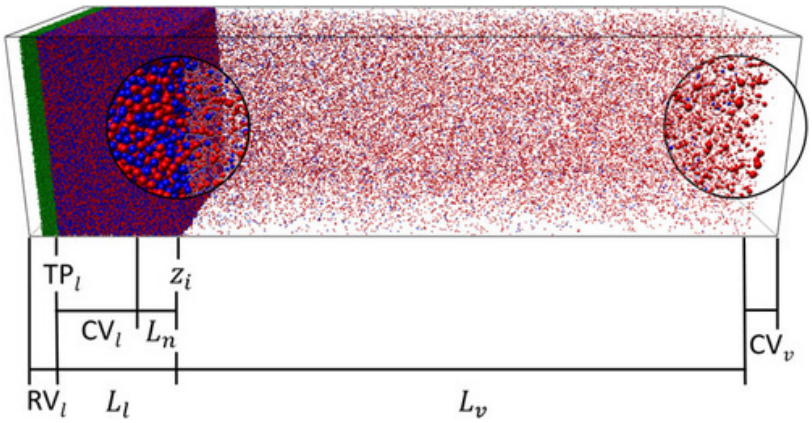


Figure 1.5: Snapshot of the simulated evaporation process at the stationary phase interface in a system consisting of the liquid and vapour phases with the lengths of $L_l$ and $L_v$, respectively, from Molecular Dynamics (MD) method, performed by Heinen & Vrabec [32].

The microscopic models are theoretically helpful and exact, however having many particles in a system makes them expensive and time consuming. For instance, in the studies performed by Heinen & Vrabec approximately $1.5 \times 10^6$ particles were considered [32]. The particle method needs to resolve the collision time scale, which means small time steps and large numbers. Hence, the MD method is time-consuming and expensive.

In another approach, the Boltzmann equation, the core equation of the kinetic theory, is first modified to the Enskog-Vlasov (EV) equation that can be used to solve the flow in high resolutions in all three regions. Although the Boltzmann equation is not valid for the liquid and is not exact for describing the dense vapour, the EV model describes the liquid, interface, and vapour [33]. Hence, in the small-scale system that dense substance is in both liquid and vapour phases, the EV is helpful for studying the flow in the required high resolutions.

The EV equation can be solved using the Direct Simulation Monte Carlo (DSMC) method [34]. In the DSMC method, sample particles that stand in for thousands of the particles are considered instead of studying every particle. The sample particles travel freely with different microscopic velocities, and the collisions between random pairs of the particles near each other are considered, where the collision details are based on the statistical stochastic models [30]. After performing the collision parameters for a short

time, the procedure repeats for the next short period that the collisions occurred between the particles with new microscopic velocities and so on [30]. This method can be used for different molecule models [30]; for instance, it solves the Boltzmann or the EV equations. More detail about the DSMC method can be found in Refs. [34–36].

Although the DSMC method considers fewer particles than the MD method and is more affordable than the MD, it is still a microscopic method that is costly and time-consuming, too.

Hence, in another approach, to resolve the flow quicker and cheaper in high resolutions, instead of solving the EV equation, it is approximated by the Grad's moment method. The approximation method leads to the derivation of the macroscopic sets of equations that are solved relatively quickly and cheaper than the DSMC but less exact than it.

A new macroscopic set of transport equations, known as the 26-moment equations, derived by Struchtrup & Frezzotti based on EV equation using the Grad's moment method [37]. The equations are solved here to test the quality of the model in resolving the interface as well as using it for determining the interface resistivities.

## 1.5 Purpose and Scope

This research focuses on modelling the non-equilibrium evaporation/condensation process that predicts the considerable jump and slip conditions at the phase interface in a better agreement than the classical studies with the one observed in the experiments. For this, the steady-state evaporation/condensation process is modelled in a 1-D system, shown in Figure 1.6.

Having a full picture of interface resistivities is essential to model the jump and slip conditions at the interface using the sharp interface method. Therefore, the interface resistivities are determined in this research based on the resolved system in high resolution on the order of particle diameter. For this, the 26-moment set of macroscopic equations is

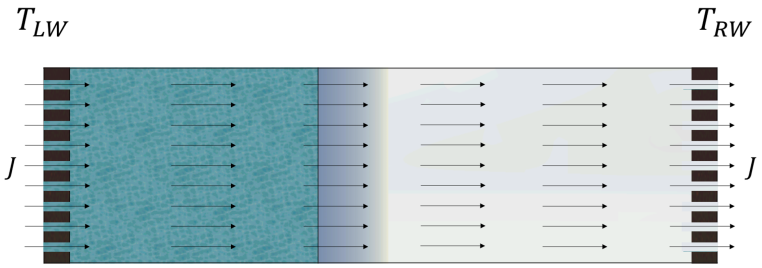


Figure 1.6: Steady-state 1-D non-equilibrium evaporation system with two temperature boundaries.

solved numerically.

The 26-moment equations resolve the liquid-interface-vapour as a dense system. The equations are solved for the different processes and system configurations. The resolved system shows the interface structure and the continuous changes of the variables from liquid to vapour across the interface that defines the jump and slip conditions. The interface resistivities are determined for the different interface temperatures and non-equilibrium strengths based on the solutions of the 26-moment equations.

Also, to test the 26-moment set of macroscopic equations, the solutions are compared with the results from the DSMC method as a microscopic method.

## 1.6 Thesis Structure

This work has been divided into six chapters, including Chap. 1. In Chap. 2, first a short review of the kinetic theory and the modifications of the Boltzmann equation into the EV equation is presented, and then the procedure of constructing the required macroscopic model is shortly reviewed.

Chapter 3 presents the 26-moment equations derived by Struchtrup & Frezzotti, which are the equations solved here to resolve the interface macroscopically while considering the microscopic and phase change effects in the system. Also, in this chapter, the equations are simplified and made dimensionless for the one-dimensional steady-state system. It is shown that the 26-moment equations can be simplified to NSF equations far enough from

the interface in bulk phases.

Chapter 4 presents the methodology of finding the numerical solutions of the 26-moment transport equations as a boundary condition problem using MATLAB for different system configurations. Resolved phase interface from the solutions of the 26-moment equations is presented and discussed for various processes. The comparisons between the 26-moment results and the DSMC results as well as the experimental observations are shown.

Chapter 5 demonstrates how the resolved interface is used to determine the interface resistivities as the functions of the interface temperatures and the strength of the non-equilibrium for different processes. Then, the EV interface resistivities are presented and discussed.

Finally, in Chap. 6, a conclusion and some recommendations for future studies are given.

# Chapter 2

# Enskog-Vlasov Theory and its Approximation

In order to resolve the system that gives the changes of the variables from one phase to another at the interface macroscopically, a transport set of equations that considers the real gas effects, as well as the phase change effects, is required.

Derivation of the appropriate set of equations using methods like Grad's moments first requires a modified kinetic theory equation that counts the real gas and phase change effects. Therefore, the Boltzmann equation, the central equation of the kinetic theory that is based on the ideal gas assumptions, is modified to the Enskog-Vlasov (EV) equation.

After giving a short review of the kinetic theory, the Enskog-Vlasov (EV) equation is presented as the modification of the Boltzmann equation for counting the real gas effects. The EV equation describes both the liquid phase, which the Boltzmann equation can not, and the non-ideal gas vapour, while the Boltzmann equation is based on ideal gas assumptions. As a result, it can be used to study the flow in the entire system, which leads to resolving the system.

## 2.1 Overview of Kinetic Theory

Classical kinetic theory considers monatomic ideal gases with binary collisions; more information and overviews on the kinetic theory can be read in Refs. [30, 38–41]. Extensins of this, e.g., to polyatomic molecules, mixtures etc., can be found in Refs. [40, 42–44].

The Boltzmann equation is the central equation of the kinetic theory of gases [45]

$$\frac{\partial f}{\partial t} + c_k \frac{\partial f}{\partial x_k} + G_k \frac{\partial f}{\partial c_k} = S(f, f), \tag{2.1}$$

where the distribution function $f$ is the number density of particles with a microscopic velocity $c_k$ at the location of $x_k$ at any time $t$. Also, $G_k$ is the external forces like gravity, and $S$ is the Boltzmann collision term, and it is written in the form of $S(f, f)$ to indicate its non-linear nature. The Boltzmann equation is a non-linear integro-differential equation for the distribution function $f$ [30].

## 2.2 Enskog-Vlasov (EV) Equation

The ideal gas assumptions are valid when a system is at relatively low pressures and high temperatures, that is sufficiently dilute gases. In dense gases, the ideal gas assumptions might be valid only in extreme cases when the temperature is large so that the kinetic energy of the particles is so much larger than the attractive potential that it can be ignored.

In the system with the phase interface that we are interested in, the system's state is always below the critical point. In the critical point, all the properties are the same between the liquid and the vapour, and for the states above the critical point, only one phase exists [19]. A saturated liquid-vapour equilibrium is not possible when either the temperature or the pressure is above the critical point [19]. As a result, in the evaporation/condensation process, the temperature is never extremely large in the system. The phase change and real gas effects are important and need to be considered in the small-scale system.

These real gas effects, such as the long-range forces between many particles or the finite size of the particles, are not considered in the Boltzmann equation, which is based on the ideal gas assumptions. [25]. Also, the Boltzmann equation can not be used to model the liquid in the system.

The Enskog-Vlasov (EV) equation is a useful modification of the Boltzmann equation for studying the systems that the real gas effects are important. As a result, the EV equation is valid for describing the liquid-interface-vapour in the system by considering the real gas as well as the phase change effects.

The EV equation considers the size of the particles and the interactions between a particle and the other particles, by replacing the Boltzmann collision term with the Enskog collision term and adding the Vlasov force term to the external force term, so that [37]

$$\frac{\partial f}{\partial t} + c_k \frac{\partial f}{\partial x_k} + [G_k + F_k(x_l)] \frac{\partial f}{\partial c_k} = S_{En}, \tag{2.2}$$

where $F_k(x_l)$ is the Vlasov force [46] that considers the attraction forces between the particles in a dense gas [37], and $S_{En}$ is the Enskog collision term [47], which takes into account the finite size of the particles.

### 2.2.1 Enskog Term

The Enskog collisional term reads [37, 47, 48]

$$S_{En} = a^2 \iint_0^{2\pi} \int_0^{\pi/2} \left\{ \begin{array}{c} Y\left[n\left(x_r + \frac{ak_r}{2}\right)\right] f(x_s + ak_s, c_s^{1'}) f(x_t, c_t') \\ -Y\left[n\left(x_r - \frac{ak_r}{2}\right)\right] f(x_s - ak_s, c_s^{1}) f(x_t, c_t) \end{array} \right\} w \cos\Theta \sin\Theta d\Theta d\varepsilon dc^1, \tag{2.3}$$

where $k_k$ is the collision unit vector, $c_k$ and $c_k^1$ are the microscopic velocities of the particles before the collision and $c_k'$ and $c_k^{1\prime}$ are the velocities after the collision, $w = |w_k|$ is the magnitude of the relative velocity, and $w_k = c_k - c_k^1$; $\Theta$ is the collision angle. Also, $x$ and

$x \pm ak$ are the locations of the colliding particles, which are hard-sphere and their centers are at distance $a$ in the collision.

The correlation function $Y[n]$ describes how the reduced accessible volume affects the collisions that lead to the change in the distribution function by considering the following effects [37]:

- The reduction of the volume that the particles are free to travel without collision, which means the mean free path is decreased, or the collision frequency is increased.
- The finite size of the colliding particles leads to the reduction of the collision probability

There are many suggestions for the correlation function. We shall use the Carnahan-Starling equation [37, 49] that reads

$$Y[n] = \frac{1}{2}\frac{(2-\eta)}{(1-\eta)^3}, \tag{2.4}$$

where $\eta$ compares the volume of a particle to the portion of volume for one particle, that is the inverse of the number density

$$\eta = \frac{\frac{\pi a^3}{6}}{\frac{1}{n}} = \frac{n\pi a^3}{6} = \frac{\rho}{m}\frac{\pi a^3}{6}. \tag{2.5}$$

When the relative volume of the particles is negligible, for instance, in the dilute gases, the particles' diameter $a$ and the volume ratio $\eta$ are estimated zero, and the correlation equation goes to unity, which means that the Enskog collision term reduces to the Boltzmann collision term [37].

### 2.2.2 Vlasov Force

While the Enskog term deals with the effects of the particles' finite size, the long-range forces between many particles must also be considered when describing the dense gases

[37].

A particle at location $x_k$ interacts with particles at any other locations $x_k^1$ through long-range intermolecular forces. The Vlasov force $F_k$ reveals the total force exerted by all the particles on the particle at the location $x_k$ [37] as

$$F_k(x_k) = \int_{|x_k^1 - x_k|>0} \frac{d\phi}{dr} \frac{x_k^1 - x_k}{|x_k^1 - x_k|} n(x_r^1) dx, \tag{2.6}$$

where $\left|x_k^1 - x_k\right|$ is the distance between the chosen particle and any other particle, and $\phi(r)$ is the potential. From the hard-sphere particles assumption that prevents particles from overlapping, the potential is purely attractive for the distances larger than the diameter of particles $a$, as shown in Figure 2.1, and it can be written as [30, 37]

$$\phi(r) = \begin{cases} \infty & ,when \quad r < a \\ -\phi_a \left(\frac{r}{a}\right)^{-\gamma} & ,when \quad r \geqslant a \end{cases}, \tag{2.7}$$

where $\gamma$ is the order of the power potential, and $\phi_a$ is the potential when the two particles are tangent, $r = a$. The constant order of the power potential $\gamma$ determines the decay of the potential, as shown in Figure 2.1. Here, $\gamma = 6$ is chosen to match the attractive part of the Lennard-Jones potential, which describes the interaction of mon-atomic gases [50, 51].

## 2.3 Solution of the EV Equation

The macroscopic variables of the system, such as the pressure, temperature and density, can be determined from the appropriate weighted averages of the distribution function $f$ [30]. As a result, solving the EV equation for determining the distribution function is helpful. However, the EV equation is a non-linear integro-differential equation for the distribution function $f$ and finding the solution of this equation is highly challenging.

Numerical methods such as the Direct Simulation Monte Carlo (DSMC) solve the EV equation. The method has a high impact on solving the kinetic theory models [36] and

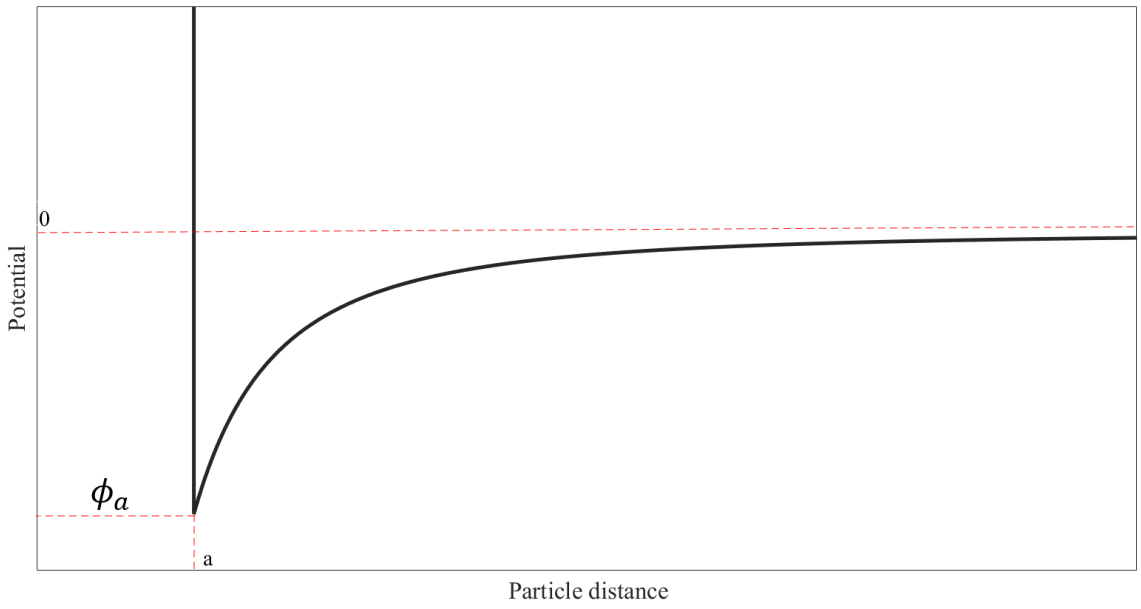


Figure 2.1: The power potential based on the hard-sphere particles assumptions, which is purely attractive for distances greater than the particle diameter $a$ and decays with the increase of the distance $r$.

although it was first introduced for the systems with dilute gases and it is mainly used to solve these kinds of gases, its relatively simple algorithm for describing complicated problems has made this possible to be developed to model the dense gases [34, 35].

In the DSMC method, the physical space is split into cells with a finite size that contains sample particles. These sample particles that stand in for thousands of the particles are considered in the cells instead of all the particles in the system. The sample particles travel freely with different microscopic velocities for a finite short time [30]. Then, the random pairs of particles that are in the same space cell can collide and interact [30]. In the DSMC, the collision details are found from the stochastic models and based on Boltzmann or EV equation. After performing the collision parameters for a short time, the procedure repeats for the next short period that the collisions occurred between the sample particles with new microscopic velocities and so on [30]. Finally, the macroscopic variables are found from averaging the distribution function.

The DSMC is an exact method for solving the EV equation; however, the vast number

of sample particles makes it costly and time-consuming. Therefore, if a macroscopic model approximates the EV kinetic model accurately enough, it can save time and cost.

## 2.4 Approximation the EV Equation

The kinetic theory models like the EV equation can be approximated with a macroscopic set of transport equations.

In all macroscopic studies, the conservation laws of the mass, momentum and energy are the starting point for any approximated equations [30]. The independent variables of these three balances are the mass density $\rho$, macroscopic velocity $v_i$, and temperature $\theta = RT$, which $\theta$ is an abbreviation for the temperature $T$. At the same time, the additional balance equations of the heat flux or the stress can be determined in two main ways.

One way, which is used in Chapman-Enskog (CE) method, is to define the heat flux and the stress as explicit functionals of the independent variables of $\{\rho, v_i, \theta\}$. The CE method is one of the most famous methods for computing the macroscopic transport equations from the microscopic equations like the Boltzmann equation [30]. It was developed by Enskog [47] and Chapman [52, 53], and its fame is mainly due to the calculation of the NSF equations with representing the explicit expressions for the stress and heat flux that depend on the gradients of the velocity and the temperature, respectively. The CE method gives NSF to 1st order in Kn number, and the higher orders produce unstable equations [30].

This clarifies why the classical NSF equations can not resolve the system in high resolutions on the order of particle diameter. The refined scale that needs to be considered for resolving the interface leads to large Kn numbers, such that considering the higher orders of them is required.

The moment method is the best-known alternative to the CE method that can be used for studying the systems in the required high resolutions by considering the higher orders

of the Kn number.

### 2.4.1 Moment Method

The moment method approximates the kinetic theory equations like EV equation by replacing the detailed kinetic equation with the moment equations [30, 37]. Moment is defined as

$$U_A = \int \psi_A(c_i) f dc, (A = 1, \ldots, N), \tag{2.8}$$

where $\psi_A(c_i)$ is any appropriate polynomial that relate the microscopic velocity to the moments. Depending on the required resolution, the number of moments can be extended, which also increases the approximation's accuracy. [30, 37, 54].

In the phase equilibrium, the system can be described only through the five moments of $U_A = \{\rho, v_i, \theta\}_A$ by considering the polynomials

$$\psi_A(c_i) = m \left\{ 1, c_i, \frac{1}{2} C^2 \right\}, \tag{2.9}$$

where $C = c_i - v_i$ is the peculiar velocity.

However, to resolve the system in high resolutions in the non-equilibrium evaporation/condensation process, more moments need to be considered. It is found by Struchtrup that at least 26 moments are required for resolving the system on the order of particle diameter properly [30].

For defining the 26 moments, the chosen polynomials are [25, 30, 37]

$$\psi_A = m \left\{ 1, c_i, \frac{1}{2} C^2, C_{<i} C_{j>}, \frac{1}{2} C^2 C_i, C_{<i} C_j C_{k>}, C^4, C^2 C_{<i} C_{j>} \right\}_A, \tag{2.10}$$

where the angle brackets indicate symmetric and trace-free tensors. A symmetric tensor is a higher order generalization of a symmetric matrix, and it stays invariant under a permu-

tation of its vector arguments [55]. The trace-free tensor denotes that the tensor vanishes.

The corresponding 26 variables from equation (2.10) are

$$\rho = mn = m\int f dc \quad , \quad \rho v_i = m\int c_i f dc \quad , \quad \rho u = \tfrac{3}{2}\rho\theta = \tfrac{m}{2}\int C^2 f dc$$

$$\sigma_{ij} = m\int C_{<i}C_{j>} f dc \quad , \quad q_i = \tfrac{m}{2}\int C^2 C_i f dc$$

$$m_{ijk} = m\int C_{<i}C_j C_{k>} f dc \quad , \quad \Delta = m\int C^4 (f - f_E)\, dc \quad , \quad R_{ij} = m\int C_{<i}C_{j>}\left(C^2 - 7\theta\right) f dc, \tag{2.11}$$

where $u$ is the specific internal energy, and $f_E$ is the phase space in equilibrium

The first line of Equation 2.11 is for the five moments from the mass density $\rho$, momentum density $\rho v_i$, and the internal energy density $\rho u$, respectively.

The second and the third lines of Equation 2.11 are the non-equilibrium moments, which vanish in the equilibrium state. The kinetic stress tensor $\sigma_{ij}$, and kinetic heat flux $q_i$ are the kinetic components of the overall stress and energy flux.

The third line of Equation 2.11 introduces the higher-order moments that give thirteen independent moments. The mass flow tensor $m_{ijk}$ is the trace-free part of the 3rd moment, $\Delta$ is the non-equilibrium part of the full trace of 4th moment, and $R_{ij}$ is the trace-free part of the single trace of 4th moment.

After choosing the moments, the macroscopic transport equations are constructed from multiplying the Boltzmann or EV equation with $\psi_A(c_i)$ and integrating over the velocity space.

As we are interested in describing the liquid, interface and dense vapour in high resolutions, the multiplication of the EV equation (2.2) with $\psi_A(c_i)$ reads [37]

$$\frac{\partial U_A}{\partial t} + \frac{\partial \Lambda_{Ak}}{\partial x_k} = [G_k + F_k(x_l)]\Upsilon_{Ak} + P_A, \tag{2.12}$$

with

$$\Lambda_{Ak} = \int \psi_A(c_i) c_k f dc$$

$$\Upsilon_{Ak} = \int \frac{\partial \psi_A(c_i)}{\partial c_k} f dc \tag{2.13}$$

$$P_A = \int \psi_A(c_i) S_{En} dc.$$

### 2.4.2 Grad's Moment Method

To continue the procedure of constructing the moment equations from equation (2.12), approximating the distribution function as a function of the moments is required [30, 37, 56]. Grad's moment method approximates the distribution function $f_G$ for a non-equilibrium state as a perturbation of the equilibrium distribution $f_E$. The equilibrium phase space is the Maxwellian $f_M$ [30, 57, 58]

$$f_E = f_M = \frac{\rho}{m} \frac{1}{\left(\sqrt{2\pi\theta}\right)^3} \exp\left[-\frac{(c_i - v_i)^2}{2\theta}\right], \tag{2.14}$$

and the Grad's distribution function has the form of [37]

$$f_G \approxeq f_{|M} \left[1 - \lambda_A(U_A)\, \psi_A(c_i)\right], \tag{2.15}$$

where $\lambda_A$ are the expansion coefficients and need to be found as a function of the moments. This can be done by substituting the above Grad's distribution function $f_G$ into the equation (2.8). After determining the $\lambda_A$ the Grad's distribution function is found as a function of the moments, and inserting it in equation (2.13), gives $\Lambda_{Ak}$, $\Upsilon_{Ak}$ and $P_A$. Finally, the closed set of moment equations can be derieved by inserting $\Lambda_{Ak}$, $\Upsilon_{Ak}$ and $P_A$ into the equation (2.12). Further discussions about the derivation of the macroscopic equations can be found in Refs. [30, 57, 59].

# Chapter 3

# 26-Moment Equations

The 26-moment set of macroscopic equations derived by Struchtrup & Frezzotti as an approximation of the EV equation using the Grad's moment method [25]. The equations are presented and they are simplified and made dimensionless for the 1-D steady-state processes.

## 3.1 Partly Linearized Transport Equations

Equations are partly linearized for small deviations from equilibrium. When linearizing around the equilibrium, due to the non-zero mass density gradients in the equilibrium at the interface, the non-linear contributions of the mass density gradients are kept [25]. Also, the non-localities in the Enskog collision term are approximated by Taylor expansions with the particle diameter $a$ as the smallness parameter [25].

The closed set of macroscopic equations for the 26 moments are presented here [25]. The index notation and Einstein's summation are used to write the equations as compact as possible in all of the following balance equations. In order to understand the equations better, in the 26-moment equations, the NSF-like contributions are highlighted in blue. This helps to see how the 26-moment equations resolve the system in high resolutions by considering terms above the NSF equations.

### 3.1.1 Mass Conservation

There is no mass transfer during the collisions of the hard-sphere particles, and it is affected by neither the Enskog nor Vlasov terms, it reads

$$\frac{\partial \rho}{\partial t} + \frac{\partial \left(\rho v_k\right)}{\partial x_k} = 0. \tag{3.1}$$

### 3.1.2 Momentum Balance

Momentum balance which considers terms up to the 4th order for non-equilibrium contributions, and mass density contributions up to 5th order [25, 37] reads

$$\begin{aligned}
\frac{\partial(\rho v_i)}{\partial t} + \frac{\partial}{\partial x_k} \Bigg( & \rho v_i v_k \\
& + \left[\rho\theta\left(1+\tfrac{2\pi}{3}\tfrac{a^3}{m}\rho Y\right) - \tfrac{2\pi a^3}{3}\tfrac{\phi_a}{m}\chi_1\rho^2\right]\delta_{ij} \\
& + \left[1+\tfrac{2}{5}\tfrac{2\pi}{3}\tfrac{a^3}{m}\rho Y\right]\sigma_{ik} \\
& - \tfrac{4}{5}\tfrac{a^4\sqrt{\pi}}{m\sqrt{\theta}}\rho^2 Y\left(\theta\frac{\partial(\delta_{(ik}v_{s)})}{\partial x_s} + \frac{1}{10}\frac{\partial\left(\frac{\delta_{(ik}q_{s)}}{\rho}\right)}{\partial x_s} + \frac{1}{42}\frac{\partial\left(\frac{m_{iks}}{\rho}\right)}{\partial x_s}\right) \\
& + \tfrac{\pi}{60}\tfrac{a^5}{m}\left(\frac{\partial^2\left(Y\rho^2\theta\right)}{\partial x_s\partial x_t} + 3Y\frac{\partial^2\left(\rho^2\theta\right)}{\partial x_s\partial x_t} - 12Y\frac{\partial\rho}{\partial x_s}\frac{\partial(\rho\theta)}{\partial x_t} - \tfrac{1}{2}\theta\rho^2\frac{d^2Y}{d\rho^2}\frac{\partial\rho}{\partial x_s}\frac{\partial\rho}{\partial x_t}\right)\delta_{(ik}\delta_{st)} \\
& - \tfrac{2\pi a^5}{15}\tfrac{\phi_a}{m}\chi_3\left[\left(\rho\frac{\partial^2\rho}{\partial x_r\partial x_r} + \tfrac{1}{2}\frac{\partial\rho}{\partial x_r}\frac{\partial\rho}{\partial x_r}\right)\delta_{ik} - \frac{\partial\rho}{\partial x_i}\frac{\partial\rho}{\partial x_k}\right]
\end{aligned}\Bigg) = \rho G_i, \tag{3.2}$$

where $\chi_1 = \frac{\gamma}{\gamma-3}$ and $\chi_3 = \frac{\gamma}{\gamma-5}$ are defined with the order of the power potentials; $G_i$ is the body force.

For any fluid, the momentum balance has the form

$$\frac{\partial\left(\rho v_i\right)}{\partial t} + \frac{\partial}{\partial x_k}\left(\rho v_i v_k + \left(p + t_{ik}\right)\right) = \rho G_i, \tag{3.3}$$

where $t_{ik}$ is the overall stress. Comparison with equation (3.2) shows that the EV momentum balance is of this form where the expression under the space derivative is the overall momentum flux. The first line of equation (3.2) is the convective momentum transfer, same as the general form of the balance. The second line is the van-der-Waals-like pressure in bulk and will be discussed shortly, whose its first term comes from the Enskog term, and the second term is the Vlasov stress contribution.

Compared to (3.3), in the EV26 momentum balance (3.2), the overall stress $t_{ik}$ consists of a larger number of contributions as follows:

The third line is the kinetic stress $\sigma_{ik}$ contributions with the Enskog correction, and the fourth line is the higher contributions to the stress at different orders in the particles' diameter $a$.

The last two lines are the stresses due to density gradients, which in particular play roles at the interface. They are the surface tension stresses, and due to the phase change, they are non-zero at the interface, even in the global equilibrium state. Therefore, the contributions of the mass density changes are considered up to the 5th order of $a$. In the fifth line, the term highlighted in brown is Maxwell's equal-area rule correction that is discussed in Subsec. 3.2.1.

It is seen from the momentum balance of the 26-moment equations that the kinetic stress $\sigma_{ik}$ contributes to the stress, but the overall stress $t_{ij}$ has more contributions that are defined.

The right-hand side of the momentum balance denotes the external body forces like gravity.

### 3.1.3 Internal Energy Balance

The internal energy balance reads [25, 37]

$$\frac{3}{2}\frac{\partial(\rho\theta)}{\partial t}+\frac{\partial}{\partial x_k}\left[\begin{array}{c}\frac{3}{2}\rho v_k\theta\\ +\left(1+\frac{3}{5}\frac{2\pi}{3}\frac{a^3}{m}\rho Y\right)q_k\\ -\frac{2}{3}\frac{a^4\sqrt{\pi}}{m}\rho^2 Y\sqrt{\theta}\left(\frac{\partial\theta}{\partial x_k}+\frac{2}{5}\frac{\partial\left(\frac{\sigma_{ks}}{\rho}\right)}{\partial x_s}+\frac{1}{60\theta}\frac{\partial\left(\frac{\Delta}{\rho}\right)}{\partial x_k}+\frac{1}{35\theta}\frac{\partial\left(\frac{R_{ks}}{\rho}\right)}{\partial x_s}\right)\end{array}\right] \tag{3.4}$$
$$=-\left[\rho\theta(1+\tfrac{2\pi}{3}\tfrac{a^3}{m}\rho Y)\delta_{kl}+\rho\theta(1+\tfrac{2}{5}\tfrac{2\pi}{3}\tfrac{a^3}{m}\rho Y)\sigma_{kl}\right]\frac{\partial v_k}{\partial x_l}.$$

The internal energy balance for any fluids reads

$$\frac{3}{2}\frac{\partial(\rho\theta)}{\partial t}+\frac{\partial}{\partial x_k}\left(\frac{3}{2}\rho v_k\theta+Q_k\right)=-\xi_{kl}\frac{\partial v_k}{\partial x_l}, \tag{3.5}$$

where $Q_k$ is the overall non-convective heat flux, and $\xi_{kl}$ is the frictional heating. Comparison with equation (3.4) shows that the EV internal energy balance is of this form where the expression under the space derivative is the summation of the convective and non-convective heat fluxes. The first line is the convective contribution.

Compared to (3.5), the EV26 non-convective heat flux $Q_k$ consists of a larger number of contributions as follows:

The second line is the kinetic heat flux $q_k$ with generalizations from the Enskog collision term, and the third line is the heat flux contributions up to the 4th order due to the temperature gradient, the kinetic stress tensor gradient and the gradients of the $\Delta$ and $R_{ks}$.

Hence, the generalized non-convective heat flux $Q_k$ in 26-moment equations reads

$$Q_k=\left(1+\frac{3}{5}\frac{2\pi}{3}\frac{a^3}{m}\rho Y\right)q_k-\frac{2}{3}\frac{a^4\sqrt{\pi}}{m}\rho^2 Y\sqrt{\theta}\left(\frac{\partial\theta}{\partial x_k}+\frac{2}{5}\frac{\partial\left(\frac{\sigma_{ks}}{\rho}\right)}{\partial x_s}+\frac{1}{60\theta}\frac{\partial\left(\frac{\Delta}{\rho}\right)}{\partial x_k}+\frac{1}{35\theta}\frac{\partial\left(\frac{R_{ks}}{\rho}\right)}{\partial x_s}\right). \tag{3.6}$$

The kinetic heat flux $q_k$ contributes to the non-convective heat flux, but the overall non-convective heat flux $Q_k$ has more contributions that are defined.

The right-hand side of the internal energy balance describes the frictional heating that

the contributions of Enskog through the $Y$.

### 3.1.4 Kinetic Stress Balance

The kinetic stress balance reads [25]

$$
\begin{aligned}
&\frac{\partial \sigma_{ij}}{\partial t} + 2\left[\rho\theta\left(1+\tfrac{2}{5}\tfrac{2\pi}{3}\tfrac{a^3}{m}\rho Y\right)\right]\frac{\partial v_{\langle i}}{\partial x_{j\rangle}} + \tfrac{4}{5}\frac{\partial}{\partial x_{\langle i}}\left[\left(1+\tfrac{3}{5}\tfrac{2\pi}{3}\tfrac{a^3}{m}\rho Y\right)q_{j\rangle}\right] \\
&+\frac{\partial}{\partial x_k}\left[\left(1+\tfrac{6}{35}\tfrac{2\pi}{3}\tfrac{a^3}{m}\rho Y\right)m_{ijk}\right] + \tfrac{6}{25}\tfrac{2\pi}{3}\tfrac{a^3}{m}\left[q_{\langle i}\delta_{j\rangle r} + \tfrac{20}{21}m_{ijk}\right]\tfrac{1}{\rho}\frac{\partial\left(\rho^2 Y\right)}{\partial x_r} \\
&-\frac{a^4\sqrt{\pi}}{m}\sqrt{\theta}\left[\tfrac{8}{15}\rho^2\frac{\partial}{\partial x_{\langle i}}\left(Y\frac{\partial\theta}{\partial x_{j\rangle}}\right) + \tfrac{16}{15}\rho Y\frac{\partial\rho}{\partial x_{\langle i}}\frac{\partial\theta}{\partial x_{j\rangle}}\right] \\
&-\frac{a^4\sqrt{\pi}}{m\sqrt{\theta}}\left[\tfrac{2}{225}\rho\frac{\partial}{\partial x_{\langle i}}\left(Y\frac{\partial\Delta}{\partial x_{j\rangle}}\right) - \tfrac{2}{225}\Delta\frac{\partial\rho}{\partial x_{\langle i}}\left(Y\frac{\partial\rho}{\partial x_{j\rangle}}\right)\right] \\
&-\frac{a^4\sqrt{\pi}}{m}\sqrt{\theta}\left[\tfrac{8}{105}\rho\frac{\partial}{\partial x_r}\left(Y\frac{\partial\sigma_{ij}}{\partial x_r}\right) - \tfrac{16}{35}\sigma_{ij}\frac{\partial}{\partial x_r}\left(Y\frac{\partial\rho}{\partial x_r}\right) - \tfrac{2}{21}\rho\sigma_{ij}\frac{\partial^2 Y}{\partial x_r\partial x_r}\right] \\
&-\frac{a^4\sqrt{\pi}}{m}\sqrt{\theta}\left[\begin{array}{c} +\tfrac{16}{105}\rho\frac{\partial}{\partial x_{\langle i}}\left(Y\frac{\partial\sigma_{j\rangle r}}{\partial x_r}\right) - \tfrac{8}{21}\sigma_{r\langle i}\frac{\partial}{\partial x_{j\rangle}}\left(Y\frac{\partial\rho}{\partial x_r}\right) - \tfrac{4}{35}\rho\sigma_{r\langle i}\frac{\partial^2 Y}{\partial x_{j\rangle}\partial x_r} \\ +\tfrac{16}{105}\rho\frac{\partial}{\partial x_r}\left(Y\frac{\partial\sigma_{r\langle i}}{\partial x_{j\rangle}}\right) - \tfrac{8}{21}\sigma_{r\langle i}\frac{\partial}{\partial x_r}\left(Y\frac{\partial\rho}{\partial x_{j\rangle}}\right)\end{array}\right] \\
&-\frac{a^4\sqrt{\pi}}{m\sqrt{\theta}}\left[\tfrac{4}{735}\rho\frac{\partial}{\partial x_r}\left(Y\frac{\partial R_{ij}}{\partial x_r}\right) - \tfrac{2}{105}R_{ij}\frac{\partial}{\partial x_r}\left(Y\frac{\partial\rho}{\partial x_r}\right) - \tfrac{1}{294}\rho R_{ij}\frac{\partial^2 Y}{\partial x_r\partial x_r}\right] \\
&-\frac{a^4\sqrt{\pi}}{m\sqrt{\theta}}\left[\begin{array}{c} +\tfrac{8}{735}\rho\frac{\partial}{\partial x_{\langle i}}\left(Y\frac{\partial R_{j\rangle r}}{\partial x_r}\right) - \tfrac{2}{105}R_{r\langle i}\frac{\partial}{\partial x_{j\rangle}}\left(Y\frac{\partial\rho}{\partial x_r}\right) - \tfrac{1}{245}\rho R_{r\langle i}\frac{\partial^2 Y}{\partial x_{j\rangle}\partial x_r} \\ +\tfrac{8}{735}\rho\frac{\partial}{\partial x_r}\left(Y\frac{\partial R_{r\langle i}}{\partial x_{j\rangle}}\right) - \tfrac{2}{105}R_{r\langle i}\frac{\partial}{\partial x_r}\left(Y\frac{\partial\rho}{\partial x_{j\rangle}}\right)\end{array}\right] \\
&\qquad\qquad = -\left[\tfrac{16}{5}\frac{\rho\sqrt{\pi\theta}a^2}{m}Y\right]\left(\sigma_{ij} + \tfrac{1}{28}\frac{R_{ij}}{\theta}\right),
\end{aligned}
\tag{3.7}
$$

where many terms are showed up in the stress balance that consider the finite size of the particles and the attractive forces between them due to the thermodynamic fluxes as well as the phase change.

### 3.1.5 Kinetic Heat Flux Balance

The kinetic heat flux balance reads [25]

$$
\begin{aligned}
&\frac{\partial q_i}{\partial t}+\frac{5}{2}\rho\theta\left[1+\frac{3}{5}\frac{2\pi}{3}\frac{a^3}{m}\rho Y\right]\frac{\partial\theta}{\partial x_i}\\
&+\theta\frac{\partial}{\partial x_k}\left[\left(1+\frac{3}{5}\frac{2\pi}{3}\frac{a^3}{m}\rho Y\right)\sigma_{ik}\right]+\frac{1}{2}\frac{\partial}{\partial x_k}\left[\left(1+\frac{12}{35}\frac{2\pi}{3}\frac{a^3}{m}\rho Y\right)R_{ik}\right]\\
&+\frac{1}{6}\frac{\partial}{\partial x_i}\left[\left(1+\frac{3}{5}\frac{2\pi}{3}\frac{a^3}{m}\rho Y\right)\Delta\right]-\frac{\sigma_{ik}}{\rho}\theta\frac{\partial}{\partial x_k}\left[\left(1+\frac{9}{10}\frac{2\pi}{3}\frac{a^3}{m}\rho Y\right)\rho\right]\\
&+\frac{2\pi}{3}\frac{a^3}{m}\left[\frac{1}{30}\frac{\Delta}{\rho}\delta_{ik}+\frac{11}{140}\frac{R_{ir}}{\rho}\right]\frac{\partial\left(\rho^2 Y_0\right)}{\partial x_r}\\
&-\frac{a^4\sqrt{\pi}}{m}\sqrt{\theta}\left[-\frac{19}{15}\theta\frac{\partial}{\partial x_r}\left(\rho^2 Y\frac{\partial v_i}{\partial x_r}\right)-\frac{38}{15}\theta\frac{\partial}{\partial x_{\langle i}}\left(\rho^2 Y\frac{\partial v_r}{\partial x_{r\rangle}}\right)\right]\\
&-\frac{a^4\sqrt{\pi}}{m}\sqrt{\theta}\left[\begin{array}{c}+\frac{9}{50}\rho\frac{\partial}{\partial x_r}\left(Y\frac{\partial q_i}{\partial x_r}\right)-\frac{1}{2}q_i\frac{\partial}{\partial x_r}\left(Y\frac{\partial\rho}{\partial x_r}\right)-\frac{2}{25}\rho q_i\frac{\partial^2 Y}{\partial x_r\partial x_r}\\+\frac{9}{25}\rho\frac{\partial}{\partial x_{\langle i}}\left(Y\frac{\partial q_r}{\partial x_r}\right)-\frac{11}{15}q_r\frac{\partial}{\partial x_{\langle i}}\left(Y\frac{\partial\rho}{\partial x_{r\rangle}}\right)-\frac{2}{75}\rho q_r\frac{\partial^2 Y}{\partial x_r\partial x_i}\end{array}\right]\\
&-\frac{a^4\sqrt{\pi}}{m}\sqrt{\theta}\left[\frac{9}{70}\rho\frac{\partial}{\partial x_r}\left(Y\frac{\partial m_{irs}}{\partial x_s}\right)-\frac{1}{6}m_{irs}\frac{\partial}{\partial x_r}\left(Y\frac{\partial\rho}{\partial x_s}\right)-\frac{1}{105}\rho m_{irs}\frac{\partial^2 Y}{\partial x_r\partial x_s}\right]\\
&=-\frac{2}{3}\left[\frac{16}{5}\frac{a^2\rho\sqrt{\pi\theta}}{m}Y\right]q_i.
\end{aligned}
\tag{3.8}
$$

### 3.1.6 $m_{ijk}$ Balance

The balance of $m_{ijk}$ balance as a higher-order moment up to the 4th order contributions is [25]

$$
\begin{aligned}
&\frac{\partial m_{ijk}}{\partial t}+3\theta\frac{\partial}{\partial x_{\langle i}}\left[\left(1+\frac{6}{35}\frac{2\pi}{3}\frac{a^3}{m}\rho Y\right)\sigma_{jk\rangle}\right]\\
&-3\frac{\theta\sigma_{\langle ij}}{\rho}\frac{\partial}{\partial x_{k\rangle}}\left[\left(1+\frac{2}{5}\frac{2\pi}{3}\frac{a^3}{m}\rho Y\right)\rho\right]\\
&+\frac{3}{7}\frac{\partial}{\partial x_{\langle i}}\left[\left(1+\frac{12}{35}\frac{2\pi}{3}\frac{a^3}{m}\rho Y\right)R_{jk\rangle}\right]+\frac{93}{490}\frac{2\pi}{3}\frac{a^3}{m}\frac{R_{\langle ij}}{\rho}\frac{\partial\left(\rho^2 Y\right)}{\partial x_{k\rangle}}\\
&-\frac{a^4\sqrt{\pi}}{m}\sqrt{\theta}\left[\frac{4}{35}\theta\frac{\partial}{\partial x_{\langle i}}\left(\rho^2 Y_0\frac{\partial v_j}{\partial x_{k\rangle}}\right)\right]\\
&-\frac{a^4\sqrt{\pi}}{m}\sqrt{\theta}\left[\frac{54}{175}\rho\frac{\partial}{\partial x_{\langle i}}\left(Y\frac{\partial q_j}{\partial x_{k\rangle}}\right)-\frac{2}{5}q_{\langle i}\frac{\partial}{\partial x_j}\left(Y\frac{\partial\rho}{\partial x_{k\rangle}}\right)-\frac{4}{175}\rho q_{\langle i}\frac{\partial^2 Y}{\partial x_j\partial x_{k\rangle}}\right]\\
&-\frac{a^4\sqrt{\pi}}{m}\sqrt{\theta}\left[+\frac{2}{70}\rho\frac{\partial}{\partial x_r}\left(Y\frac{\partial m_{ijk}}{\partial x_r}\right)-\frac{3}{5}m_{ijk}\frac{\partial}{\partial x_r}\left(Y\frac{\partial\rho}{\partial x_r}\right)-\frac{1}{7}\rho m_{ijk}\frac{\partial^2 Y}{\partial x_r\partial x_r}\right]\\
&-\frac{a^4\sqrt{\pi}}{m}\sqrt{\theta}\left[\begin{array}{c}+\frac{6}{70}\rho\frac{\partial}{\partial x_{\langle i}}\left(Y\frac{m_{jk\rangle r}}{\partial x_r}\right)-\frac{3}{7}m_{r\langle ij}\frac{\partial}{\partial x_{k\rangle}}\left(Y\frac{\partial\rho}{\partial x_r}\right)-\frac{3}{35}\rho m_{r\langle ij}\frac{\partial^2 Y}{\partial x_{k\rangle}x_r}\\+\frac{6}{70}\rho\frac{\partial}{\partial x_r}\left(Y\frac{m_{r\langle ij}}{\partial x_{k\rangle}}\right)-\frac{3}{7}m_{r\langle ij}\frac{\partial}{\partial x_r}\left(Y\frac{\partial\rho}{\partial x_{k\rangle}}\right)-\frac{3}{35}\rho m_{r\langle ij}\frac{\partial^2 Y}{\partial x_{k\rangle}x_r}\end{array}\right]\\
&=-\frac{3}{2}\left[\begin{array}{c}\frac{16}{5}\frac{a^2\rho\sqrt{\pi\theta}}{m}Y\end{array}\right]m_{ijk}.
\end{aligned}
\tag{3.9}
$$

### 3.1.7 $\Delta$ Balance

The balance of $\Delta$ up to the 4th order is [25]

$$
\begin{aligned}
&\frac{\partial \Delta}{\partial t}+8\theta\frac{\partial}{\partial x_k}\left[\left(1+\frac{3}{5}\frac{2\pi}{3}\frac{a^3}{m}\rho Y\right)q_k\right]-8\theta\frac{q_k}{\rho}\frac{\partial}{\partial x_k}\left[\left(1+\frac{4}{5}\frac{2\pi}{3}\frac{a^3}{m}\rho Y\right)\rho\right]\\
&-\frac{a^4\sqrt{\pi}}{m}\sqrt{\theta}\left[\frac{4}{3}\rho^2\theta\frac{\partial}{\partial x_r}\left(Y\frac{\partial\theta}{\partial x_r}\right)+\frac{8}{3}\rho\theta Y\frac{\partial\rho}{\partial x_r}\frac{\partial\theta}{\partial x_r}\right]\\
&-\frac{a^4\sqrt{\pi}}{m}\sqrt{\theta}\left[\frac{8}{15}\rho^2\theta\frac{\partial}{\partial x_r}\left(Y\frac{\partial\left(\frac{\sigma_{rs}}{\rho}\right)}{\partial x_s}\right)-\frac{32}{3}\rho\theta Y\frac{\partial\rho}{\partial x_r}\frac{\partial\left(\frac{\sigma_{rs}}{\rho}\right)}{\partial x_s}\right]\\
&-\frac{a^4\sqrt{\pi}}{m}\sqrt{\theta}\left[\frac{1}{3}\rho\frac{\partial}{\partial x_r}\left(Y\frac{\partial\Delta}{\partial x_r}\right)-\frac{31}{45}\Delta\frac{\partial}{\partial x_r}\left(Y\frac{\partial\rho}{\partial x_r}\right)-\frac{4}{45}\rho\Delta\frac{\partial^2 Y}{\partial x_r\partial x_r}\right]\\
&-\frac{a^4\sqrt{\pi}}{m}\sqrt{\theta}\left[\frac{4}{7}\rho\frac{\partial}{\partial x_r}\left(Y\frac{\partial R_{rs}}{\partial x_s}\right)-\frac{76}{105}R_{rs}\frac{\partial}{\partial x_r}\left(Y\frac{\partial\rho}{\partial x_s}\right)-\frac{4}{105}\rho R_{rs}\frac{\partial^2 Y}{\partial x_r x_s}\right]\\
&=-\frac{2}{3}\left[\frac{16}{5}\frac{a^2\rho\sqrt{\pi\theta}}{m}Y\right]\Delta.
\end{aligned}
\tag{3.10}
$$

### 3.1.8 $R_{ij}$ Balance

Finally, the balance of $R_{ij}$ reads [25]

$$
\begin{aligned}
&\frac{\partial R_{ij}}{\partial t}+\frac{28}{5}\theta\frac{\partial}{\partial x_{\langle i}}\left[\left(1+\frac{12}{35}\frac{2\pi}{3}\frac{a^3}{m}\rho Y\right)q_{j\rangle}\right]+\frac{28}{5}\theta\frac{q_{\langle i}}{\rho}\frac{\partial}{\partial x_{j\rangle}}\left[\left(1+\frac{1}{2}\frac{2\pi}{3}\frac{a^3}{m}\rho Y\right)\rho\right]\\
&+2\theta\frac{\partial}{\partial x_k}\left[\left(1+\frac{12}{35}\frac{2\pi}{3}\frac{a^3}{m}\rho Y\right)m_{ijk}\right]-2\frac{m_{ijk}}{\rho}\theta\frac{\partial}{\partial x_k}\left[\left(1+\frac{11}{14}\frac{2\pi}{3}\frac{a^3}{m}\rho Y\right)\rho\right]\\
&-\frac{a^4\sqrt{\pi}}{m}\sqrt{\theta}\left[\frac{8}{15}\rho^2\theta\frac{\partial}{\partial x_{\langle i}}\left(Y\frac{\partial\theta}{\partial x_{j\rangle}}\right)+\frac{16}{15}\rho\theta Y\frac{\partial\rho}{\partial x_{\langle i}}\frac{\partial\theta}{\partial x_{j\rangle}}\right]\\
&-\frac{a^4\sqrt{\pi}}{m}\sqrt{\theta}\left[\frac{2}{15}\rho\frac{\partial}{\partial x_{\langle i}}\left(Y\frac{\partial\Delta}{\partial x_{j\rangle}}\right)-\frac{38}{225}\Delta\frac{\partial}{\partial x_{\langle i}}\left(Y\frac{\partial\rho}{\partial x_{j\rangle}}\right)-\frac{2}{225}\rho\Delta\frac{\partial^2 Y}{\partial x_{\langle i}\partial x_{j\rangle}}\right]\\
&\frac{a^4\sqrt{\pi}}{m}\sqrt{\theta}\left[+\frac{8}{105}\rho\theta\frac{\partial}{\partial x_r}\left(Y\frac{\partial\sigma_{ij}}{\partial x_r}\right)-\frac{4}{15}\theta\sigma_{ij}\frac{\partial}{\partial x_r}\left(Y\frac{\partial\rho}{\partial x_r}\right)-\frac{1}{21}\rho\theta\sigma_{ij}\frac{\partial^2 Y}{\partial x_r\partial x_r}\right]\\
&-\frac{a^4\sqrt{\pi}}{m}\sqrt{\theta}\left[\begin{array}{c}+\frac{16}{105}\rho\theta\frac{\partial}{\partial x_{\langle i}}\left(Y\frac{\partial\sigma_{j\rangle r}}{\partial x_r}\right)-\frac{4}{15}\theta\sigma_{r\langle i}\frac{\partial}{\partial x_{j\rangle}}\left(Y\frac{\partial\rho}{\partial x_r}\right)-\frac{2}{35}\rho\theta\sigma_{r\langle i}\frac{\partial^2 Y}{\partial x_{j\rangle}\partial x_r}\\+\frac{16}{105}\rho\theta\frac{\partial}{\partial x_r}\left(Y\frac{\partial\sigma_{r\langle i}}{\partial x_{j\rangle}}\right)-\frac{4}{15}\theta\sigma_{r\langle i}\frac{\partial}{\partial x_r}\left(Y\frac{\partial\rho}{\partial x_{j\rangle}}\right)\end{array}\right]\\
&-\frac{a^4\sqrt{\pi}}{m}\sqrt{\theta}\left[+\frac{4}{49}\rho\frac{\partial}{\partial x_r}\left(Y\frac{\partial R_{ij}}{\partial x_r}\right)-\frac{149}{245}R_{ij}\frac{\partial}{\partial x_r}\left(Y\frac{\partial\rho}{\partial x_r}\right)-\frac{129}{980}\rho R_{ij}\frac{\partial^2 Y}{\partial x_r\partial x_r}\right]\\
&-\frac{a^4\sqrt{\pi}}{m}\sqrt{\theta}\left[\begin{array}{c}+\frac{8}{49}\rho\frac{\partial}{\partial x_{\langle i}}\left(Y\frac{\partial R_{j\rangle r}}{\partial x_r}\right)-\frac{275}{735}R_{r\langle i}\frac{\partial}{\partial x_{j\rangle}}\left(Y\frac{\partial\rho}{\partial x_r}\right)-\frac{137}{1470}\rho R_{r\langle i}\frac{\partial^2 Y}{\partial x_{j\rangle}\partial x_r}\\+\frac{8}{49}\rho\frac{\partial}{\partial x_r}\left(Y\frac{\partial R_{r\langle i}}{\partial x_{j\rangle}}\right)-\frac{275}{735}R_{r\langle i}\frac{\partial}{\partial x_r}\left(Y\frac{\partial\rho}{\partial x_{j\rangle}}\right)\end{array}\right]\\
&=-\left[\frac{16}{5}\frac{\rho\sqrt{\pi\theta}a^2}{m}Y\right]\left(\frac{1}{2}\theta\sigma_{ij}+\frac{205}{168}R_{ij}\right).
\end{aligned}
\tag{3.11}
$$

## 3.2 Equilibrium State

In the global phase equilibrium, the temperature is homogeneous and $v_i = q_i = \sigma_{ij} = m_{ijk} = \Delta = R_{ij} = 0$, and mass conservation reduces to $\frac{\partial \rho}{\partial t} = 0$, and by ignoring the external forces, the momentum balance reduces to

$$\left( \begin{array}{c} +\left[\rho\theta(1+\frac{2\pi}{3}\frac{a^3}{m}\rho Y) - \frac{2\pi a^3}{3}\frac{\phi_a}{m}\chi_1\rho^2\right]\delta_{ij} \\ +\frac{\theta\pi}{60}\frac{a^5}{m}\left(\frac{\partial^2(Y\rho^2)}{\partial x_s \partial x_t} + 3Y\frac{\partial^2\rho^2}{\partial x_s \partial x_t} - 12Y\frac{\partial\rho}{\partial x_s}\frac{\partial\rho}{\partial x_t} - \frac{1}{2}\rho^2\frac{d^2Y}{d\rho^2}\frac{\partial\rho}{\partial x_s}\frac{\partial\rho}{\partial x_t}\right)\delta_{(ik}\delta_{st)} \\ -\frac{2\pi a^5}{15}\frac{\phi_a}{m}\chi_3\left[\left(\rho\frac{\partial^2\rho}{\partial x_r \partial x_r} + \frac{1}{2}\frac{\partial\rho}{\partial x_r}\frac{\partial\rho}{\partial x_r}\right)\delta_{ik} - \frac{\partial\rho}{\partial x_i}\frac{\partial\rho}{\partial x_k}\right] \end{array} \right) = P = constant, \tag{3.12}$$

where the right-hand side of the equation is actually the overall stress $P$. In the equilibrium state, all other balances vanish.

The first line of the equation (3.12) is the van-der-Waals-like pressure, and the other two lines are the surface tension stresses due to the mass density changes at the phase interface, determined from the Enskog and Vlasov terms, respectively. In bulk phases, where the mass densities are constant, equation (3.12) reduces to

$$p = \left[\rho\theta(1+\frac{2\pi}{3}\frac{a^3}{m}\rho Y) - \frac{2\pi}{3}\chi_1\frac{\phi_a}{m}\rho^2\right], \tag{3.13}$$

and it is used for finding the saturation liquid-vapour curve. The pressure- specific volume diagram can be plotted for a range of the volumes at different constant temperatures. Note that the specific volume is the inverse of the mass density $v = \frac{1}{\rho}$.

Figure 3.1 shows the isothermal curve in the $p - v$ diagram at the constant temperature of $\theta = 0.6$. The curve is found from the dimensionless form of equation (3.13), where $a = m = \phi_a = 1$, see Subsec. 3.3.3 below for the discussion of this. Equation (3.13) is for the system at the equilibrium state, and thermodynamic stabilities must be held. Figure 3.1 shows that a part of the $p - v$ diagram has a positive slope. The positive slope indicates that the pressure and specific volume increase simultaneously in an isothermal process, which

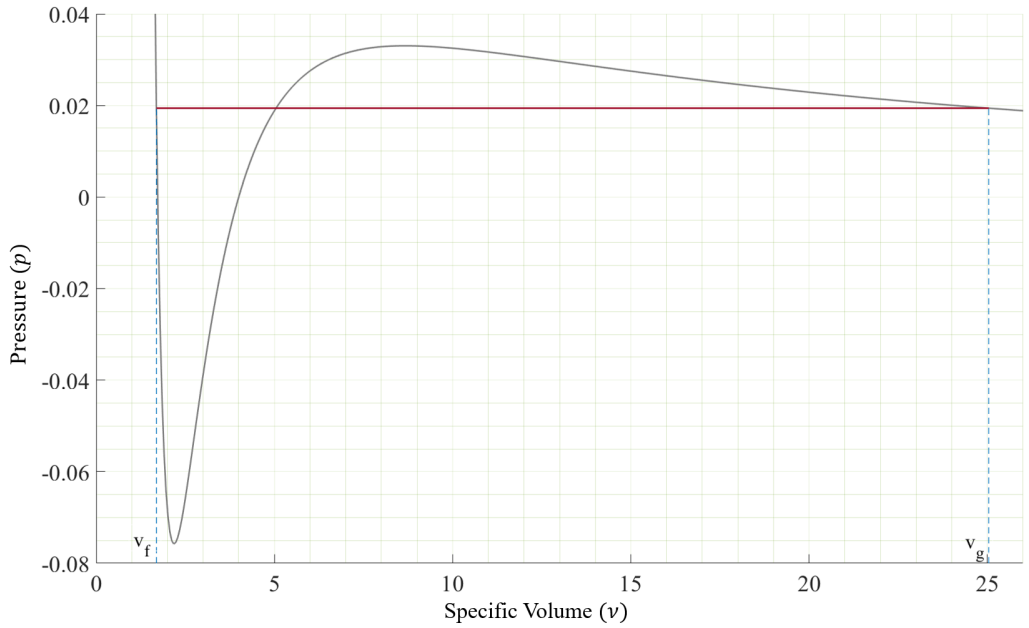


Figure 3.1: The pressure-specific volume diagram at the constant temperature of $\theta = 0.6$. The gray curve is found by plotting the dimensionless van-der-Waals-like pressure, and the horizontal red line is found from the Maxwell's equal-area rule that splits the gas into the liquid and vapour phases.

is impossible and it is unstable.

The instability leads to splitting the $p - v$ diagram into two phases, liquid and vapour, such that the isothermal line is horizontal in the two-phase region, as depicted in Figure 3.1. This is a classical thermodynamic argument that goes back to Maxwell. Maxwell's equal-area rule denotes that the area below the desired horizontal line must be the same as the area below the $p - v$ curve that reads [19]

$$f_f^* - f_g^* = -\int_f^g \left(\frac{\partial f^*}{\partial v}\right)_\theta dv = \int_f^g p dv = p_{sat}(\theta)\left[v_g - v_f\right], \tag{3.14}$$

where $f^* = g - pv$ is the Helmholtz free energy. This uniquely identifies the saturation specific volumes and pressure at different temperatures.

Stitching the determined saturation specific volumes at different temperatures leads to finding the saturation curve shown in Figure 3.2, which is drawn for the temperature range of $\theta = 0.45$ to $\theta = 0.80$. The critical point is at the top of the saturation curve, where

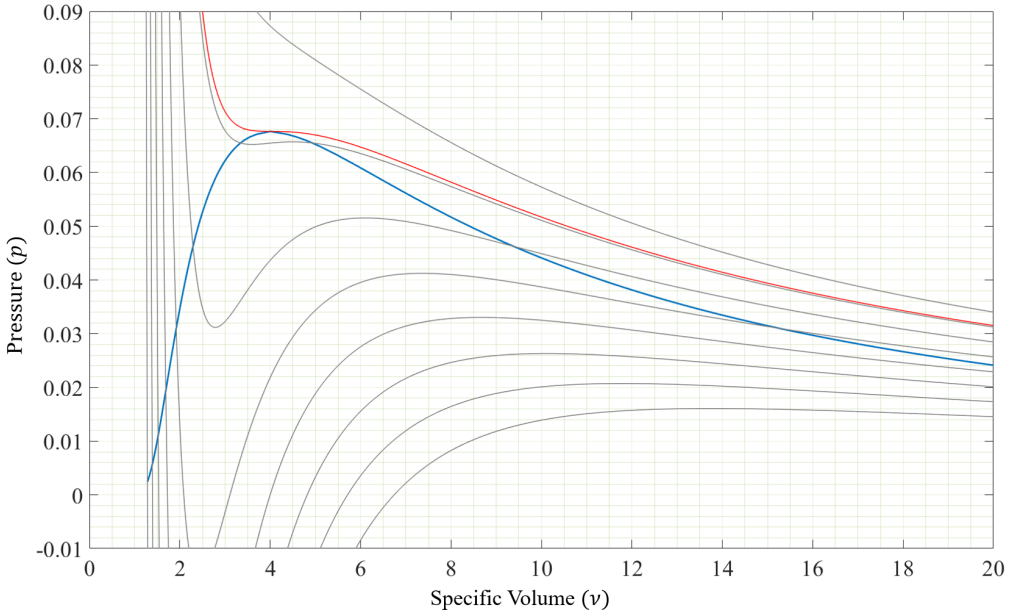


Figure 3.2: The saturation curve in blue that is found by determining the saturation specific volumes at each constant temperature using the Maxwell's equal-area rule. The gray curves are the pressure-specific volume diagrams at the different constant temperatures from the dimensionless van-der-Waals-like pressure. The red curve is the $p-v$ diagram at the critical temperature of $\theta = 0.755$.

the saturation specific volumes of both phases become identical. The calculated critical temperature is drawn in red in Figure 3.2, and it is equal to 0.755. To have the desired two-phase system, the temperatures in the system are always less than the determined critical temperature.

After determining the saturation curve from the van-der-Waals-like pressure, it is helpful to look at the phase interface at the equilibrium state. As found in equation (3.12), the equilibrium pressure at the interface has two lines of Enskog and Vlasov corrections to the van-der-Waals-like pressure due to the considerable density gradients at the interface. Figure 3.3 shows the van-der-Waals-like pressure (black curve), and the added terms (green curve), as well as the total normal stress $P$ (blue line) at the constant temperature of $\theta = 0.6$.

Figure 3.3 shows that far from the interface in bulk phases, the van-der-Waals-like pressure gives the constant saturation pressure and the higher-order stresses are zero. However,

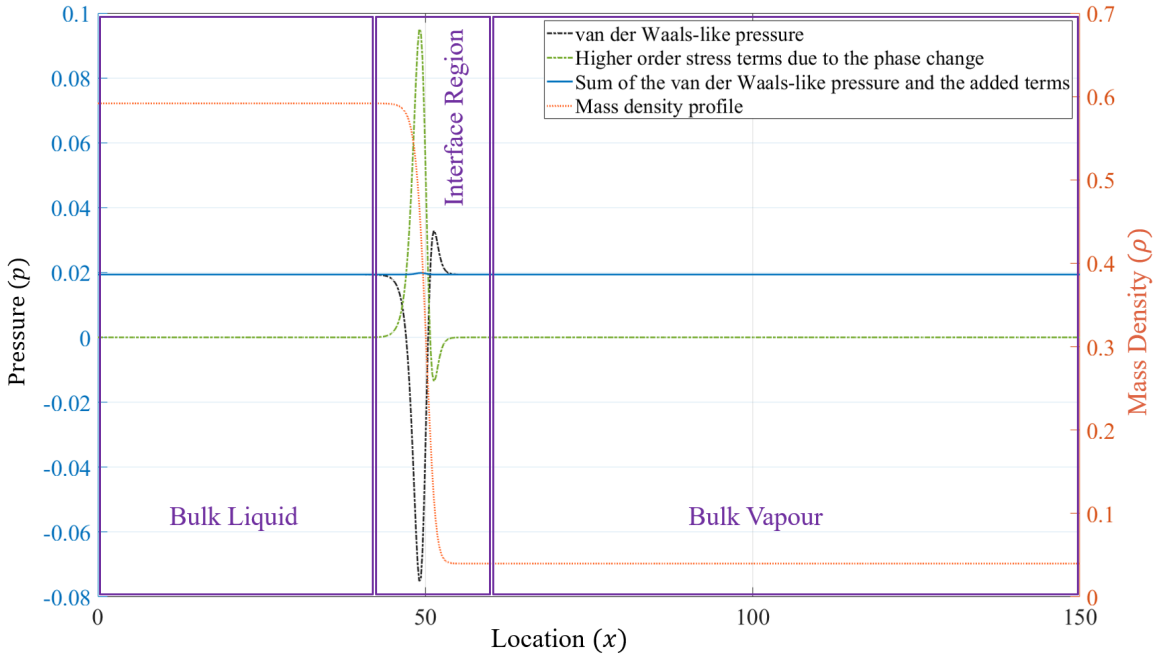


Figure 3.3: System's pressure in the global phase equilibrium together with the mass density curve when the homogeneous temperature is $\theta = 0.6$. The black curve is the van-der-Waals-like pressure, see equation (3.13). The blue curve is the stabilized pressure at the liquid-vapour interface when the surface tension contributions, shown in green, are added to the van-der-Waals-like pressure, see equation (3.12).

the van-der-Waals-like pressure at the interface region gives the non-constant pressure. In this region, the higher-order stresses due to the surface tension found from mass density gradients are non-zero and stabilize the pressure such that $P$ stays constant everywhere in the container.

### 3.2.1 Equal Area Rule in EV26

It is discussed that the equal-area rule is derived as the proper thermodynamic equilibrium condition between the two phases, and it must be valid. However, it appears that the EV equation does not fulfill this condition. As a result, a correction term highlighted in brown is added to the EV momentum balance (3.2), and here it is reviewed how this term fulfills the required equal-area rule.

Aifantis and Serrin have studied diffuse interface conditions and formulated a condition

for interfacial stresses contributions required to fulfill the equal-area rule [60]. Considering their condition with EV, one comes to the conclusion that the EV momentum balance must be corrected with the additional term [25]

$$-\frac{1}{2}\theta\rho^2\frac{d^2Y}{d\rho^2}\frac{\partial\rho}{\partial x_s}\frac{\partial\rho}{\partial x_t}, \tag{3.15}$$

which is the added correction term in the momentum balance. Also, from equation (2.4) $\frac{d^2Y}{d\rho^2} = \frac{\pi^2}{12}\frac{3-\frac{\pi a^3}{6m}\rho}{\left(1-\frac{\pi a^3}{6m}\rho\right)^5}$.

## 3.3 26-Moment Equations for 1-D Steady-State Processes

The eight balances of the closed set of 26-moment equations describe the system in liquid, vapour, and phase interface.

This set of equations can be reduced by considering the specifications of the system we are interested in.

### 3.3.1 Steady-State

Modelling the steady-state process by solving the 26-moment equations is advantageous for different reasons.

Ward et al.'s experimental results are found for a steady-state non-equilibrium process [9–11]. Therefore, to compare the results from the 26-moment equations as a theoretical macroscopic model with the observations, it is helpful to consider the same steady-state process. Also, solving the steady-state problem is easier and faster than the time-variant process.

Finally, the resolved solutions will be used to determine the interface resistivities at different temperatures of the liquid at the interface in Chap. 5. It can be done by solving the steady-state process, where the interface is stationary, and conditions do not change with time such that the liquid temperature at the interface stays constant in the process.

Hence, as shown in Figure 1.6, when the vapour is pumped out, the same mass flux of the liquid is added on the liquid side, keeping the liquid's length and the mass inside the system constant in the process. As a result, it is a steady-state process, and derivatives with respect to time vanish

$$\frac{\partial \vartheta}{\partial t} = 0, \tag{3.16}$$

where $\vartheta$ can be any variables.

### 3.3.2 One-Dimensional Process

A one-dimensional flow along the length of the container is considered, and all variables are dependent on the $x$ direction only. The relevant values variables are

$$\{\rho(x), v_1(x), \theta(x), \sigma_{11}(x), q_1(x), m_{111}(x), \Delta(x), R_{11}(x)\} \ . \tag{3.17}$$

In the general form of the 26-moment equations, there are symmetric tensors in the heat balance equation as well as the symmetric and trace-free tensors in the balances of the kinetic stress $\sigma_{ij}$, $m_{ijk}$ and $R_{ij}$ that can be simplified effectively for the one-dimensional system [61]. For convenience, in the equations for the one-dimensional system, the indices of the vectors are not written.

### 3.3.3 Dimensionless Variables

Working with the dimensionless equations is convenient because the variables have no physical dimension, and results can be used in a wide variety of problems. The appropriate dimensionless variables are introduced here

$$\bar{\rho} = \frac{\rho}{\rho_0} \quad , \quad \bar{\theta} = \frac{\theta}{\theta_0} \quad , \quad \bar{v} = \frac{v}{\sqrt{\theta_0}}$$

$$\bar{q} = \frac{q}{\rho_0 \theta_0 \sqrt{\theta_0}} \quad , \quad \overline{\sigma}_{11} = \frac{\sigma_{11}}{\rho_0 \theta_0} \quad , \quad \overline{p} = \frac{p}{\rho_0 \theta_0} \tag{3.18}$$

$$\overline{m}_{111} = \frac{m_{111}}{\rho_0 \theta_0 \sqrt{\theta_0}} \quad , \quad \overline{\Delta} = \frac{\Delta}{\rho_0 \theta_0^2} \quad , \quad \overline{R}_{11} = \frac{R_{11}}{\rho_0 \theta_0^2},$$

and they can be found from the different combinations of the reference temperature $\theta_0$ and the reference mass density $\rho_0$.

As we are interested in resolving the interface with the thickness on the order of a few particles diameter $a$, the dimensionless equations are found by choosing $\rho_0$, and $\theta_0$ as

$$\begin{aligned} \rho_0 &= \tfrac{m}{a^3} \\ \theta_0 &= \phi_a \end{aligned} \quad , \tag{3.19}$$

where obtained simply by setting $m = a = \phi_a = 1$.

### 3.3.4 1-D Steady-State Dimensionless 26-Moment Equations

The 26-moment equations are non-dimensionalized and simplified for the 1-D steady-state system here. For convenience, the overbars of the dimensionless variables are not written.

The 26-moment equations contain the correlation function, equation (2.4) which in the dimensionless variables becomes

$$Y[\rho] = \frac{1}{2} \frac{\left(2 - \frac{\rho\pi}{6}\right)}{\left(1 - \frac{\rho\pi}{6}\right)^3}. \tag{3.20}$$

The dimensionless 1-D steady-state balances read

**Mass Conservation**

$$\frac{d(\rho v)}{dx} = 0 \Longrightarrow \rho v = J = constant, \tag{3.21}$$

where $J$ is the mass flux in the system.

In the experiment, e.g. Ward et al.'s experiments [9–11], the mass flux $J$ can be controlled and kept constant. For the simulation, it will be chosen as an input value. The experiment is pumping out the vapour, and one can either control the mass flux $J$ or the system's pressure lower than the saturation pressure. For the numerical solution, controlling the mass flux $J$ is rather convenient. As a result, the constant mass flux $J$ is an input of the system, which is considered here.

**Momentum Balance**

$$\frac{d}{dx}\left(\begin{array}{c} \rho vv \\ +\left[\rho\theta\left(1+\frac{2\pi}{3}\rho Y\right)-\frac{2\pi}{3}\chi_1\rho^2\right] \\ +\left[1+\frac{2}{5}\frac{2\pi}{3}\rho Y\right]\sigma_{11} \\ -\frac{4}{5}\frac{\sqrt{\pi}}{\sqrt{\theta}}\rho^2 Y\left(\theta\frac{dv}{dx}+\frac{1}{10}\frac{d\left(\frac{q}{\rho}\right)}{dx}+\frac{1}{42}\frac{d\left(\frac{m_{111}}{\rho}\right)}{dx}\right) \\ +\frac{\pi}{60}\left(\frac{d^2\left(Y\rho^2\theta\right)}{dx^2}+3Y\frac{d^2\left(\rho^2\theta\right)}{dx^2}-12Y\frac{d\rho}{dx}\frac{d(\rho\theta)}{dx}-\frac{1}{2}\theta\rho^2\frac{d^2Y}{d\rho^2}\frac{d\rho}{dx}\frac{d\rho}{dx}\right) \\ -\frac{2\pi}{15}\chi_3\left[\left(\rho\frac{d^2\rho}{dx^2}+\frac{1}{2}\frac{d\rho}{dx}\frac{d\rho}{dx}\right)-\frac{d\rho}{dx}\frac{d\rho}{dx}\right] \end{array}\right)=0, \tag{3.22}$$

where the external body forces are ignored, and integration reads

$$\left(\begin{array}{c} \rho vv \\ +\left[\rho\theta\left(1+\frac{2\pi}{3}\rho Y\right)-\frac{2\pi}{3}\chi_1\rho^2\right] \\ +\left[1+\frac{2}{5}\frac{2\pi}{3}\rho Y\right]\sigma_{11} \\ -\frac{4}{5}\frac{\sqrt{\pi}}{\sqrt{\theta}}\rho^2 Y\left(\theta\frac{dv}{dx}+\frac{1}{10}\frac{d\left(\frac{q}{\rho}\right)}{dx}+\frac{1}{42}\frac{d\left(\frac{m_{111}}{\rho}\right)}{dx}\right) \\ +\frac{\pi}{60}\left(\frac{d^2\left(Y\rho^2\theta\right)}{dx^2}+3Y\frac{d^2\left(\rho^2\theta\right)}{dx^2}-12Y\frac{d\rho}{dx}\frac{d(\rho\theta)}{dx}-\frac{1}{2}\theta\rho^2\frac{d^2Y}{d\rho^2}\frac{d\rho}{dx}\frac{d\rho}{dx}\right) \\ -\frac{2\pi}{15}\chi_3\left[\left(\rho\frac{d^2\rho}{dx^2}+\frac{1}{2}\frac{d\rho}{dx}\frac{d\rho}{dx}\right)-\frac{d\rho}{dx}\frac{d\rho}{dx}\right] \end{array}\right)=P=constant. \tag{3.23}$$

Here $P$ is the total normal stress in the direction of propagation; it is the sum of the convective momentum, pressure, kinetic stress, and the stresses due to the real gas effects

and the phase change at and in front of the phase interface. Also, with the mass flux $J$ given, $P$ is an unknown for the solution.

**Internal Energy Balance**

$$\frac{d}{dx}\left[\begin{array}{c} \frac{3}{2}\rho v\theta \\ +\left(1+\frac{3}{5}\frac{2\pi}{3}\rho Y\right)q \\ -\frac{2}{3}\rho^2 Y\sqrt{\pi}\sqrt{\theta}\left(\frac{d\theta}{dx}+\frac{2}{5}\frac{d\left(\frac{\sigma_{11}}{\rho}\right)}{dx}+\frac{1}{60\theta}\frac{d\left(\frac{\Delta}{\rho}\right)}{dx}+\frac{1}{35\theta}\frac{d\left(\frac{R_{11}}{\rho}\right)}{dx}\right) \end{array}\right] = -\left[\rho\theta(1+\frac{2\pi}{3}\rho Y)+\rho\theta(1+\frac{2}{5}\frac{2\pi}{3}\rho Y)\sigma_{11}\right]\frac{dv}{dx} \tag{3.24}$$

**Kinetic Stress Balance**

$$\begin{array}{l} \frac{4}{3}\left[\rho\theta\left(1+\frac{2}{5}\frac{2\pi}{3}\rho Y\right)\right]\frac{dv}{dx}+\frac{8}{15}\frac{d}{dx}\left[\left(1+\frac{3}{5}\frac{2\pi}{3}\rho Y\right)q\right] \\ +\frac{d}{dx}\left[\left(1+\frac{6}{35}\frac{2\pi}{3}\rho Y\right)m_{111}\right]+\frac{2\pi}{3}\left[\frac{4}{25}q+\frac{8}{35}m_{111}\right]\frac{1}{\rho}\frac{d\left(\rho^2 Y\right)}{dx} \\ -\sqrt{\pi}\sqrt{\theta}\left[\frac{16}{45}\rho^2\frac{d}{dx}\left(Y\frac{d\theta}{dx}\right)+\frac{32}{45}\rho Y\frac{d\rho}{dx}\frac{d\theta}{dx}\right] \\ -\frac{\sqrt{\pi}}{\sqrt{\theta}}\left[\frac{4}{675}\rho\frac{d}{dx}\left(Y\frac{d\Delta}{dx}\right)-\frac{4}{675}\Delta\frac{d\rho}{dx}\left(Y\frac{d\rho}{dx}\right)\right] \\ -\sqrt{\pi}\sqrt{\theta}\left[\frac{88}{315}\rho\frac{d}{dx}\left(Y\frac{d\sigma_{11}}{dx}\right)-\frac{304}{315}\sigma_{11}\frac{d}{dx}\left(Y\frac{d\rho}{dx}\right)-\frac{6}{35}\rho\sigma_{11}\frac{d^2Y}{dx^2}\right] \\ -\frac{\sqrt{\pi}}{\sqrt{\theta}}\left[\frac{44}{2205}\rho\frac{d}{dx}\left(Y\frac{dR_{11}}{dx}\right)-\frac{2}{45}R_{11}\frac{d}{dx}\left(Y\frac{d\rho}{dx}\right)-\frac{3}{390}\rho R_{11}\frac{d^2Y}{dx^2}\right] \\ \qquad = -\left[\frac{16}{5}\rho\sqrt{\pi\theta}Y\right]\left(\sigma_{11}+\frac{1}{28}\frac{R_{11}}{\theta}\right) \end{array} \tag{3.25}$$

**Kinetic Heat Flux Balance**

$$\begin{array}{l} \frac{5}{2}\rho\theta\left[1+\frac{3}{5}\frac{2\pi}{3}\rho Y\right]\frac{d\theta}{dx} \\ +\theta\frac{d}{dx}\left[\left(1+\frac{3}{5}\frac{2\pi}{3}\rho Y\right)\sigma_{11}\right]+\frac{1}{2}\frac{d}{dx}\left[\left(1+\frac{12}{35}\frac{2\pi}{3}\rho Y\right)R_{11}\right] \\ +\frac{1}{6}\frac{d}{dx}\left[\left(1+\frac{3}{5}\frac{2\pi}{3}\rho Y\right)\Delta\right]-\frac{\sigma_{11}}{\rho}\theta\frac{d}{dx}\left[\left(1+\frac{9}{10}\frac{2\pi}{3}\rho Y\right)\rho\right] \\ +\frac{2\pi}{3}\left[\frac{1}{30}\frac{\Delta}{\rho}+\frac{11}{140}\frac{R_{11}}{\rho}\right]\frac{d\left(\rho^2 Y\right)}{dx} \\ -\sqrt{\pi}\sqrt{\theta}\left[-\frac{19}{5}\theta\frac{d}{dx}\left(\rho^2 Y\frac{dv}{dx}\right)\right] \\ -\sqrt{\pi}\sqrt{\theta}\left[+\frac{27}{50}\rho\frac{d}{dx}\left(Y\frac{dq}{dx}\right)-\frac{37}{30}q\frac{d}{dx}\left(Y\frac{d\rho}{dx}\right)-\frac{8}{75}\rho q\frac{d^2Y}{dx^2}\right] \\ -\sqrt{\pi}\sqrt{\theta}\left[\frac{9}{70}\rho\frac{d}{dx}\left(Y\frac{dm_{111}}{dx}\right)-\frac{1}{6}m_{111}\frac{d}{dx}\left(Y\frac{d\rho}{dx}\right)-\frac{1}{105}\rho m_{111}\frac{d^2Y}{dx^2}\right] \\ \qquad = -\frac{2}{3}\left[\frac{16}{5}\rho\sqrt{\pi\theta}Y\right]q \end{array} \tag{3.26}$$

### $m_{111}$ Balance

$$
\begin{aligned}
&\tfrac{8}{5}\theta\tfrac{d}{dx}\left[\left(1+\tfrac{6}{35}\tfrac{2\pi}{3}\rho Y\right)\sigma_{11}\right]\\
&-\tfrac{8}{5}\tfrac{\theta\sigma_{11}}{\rho}\tfrac{d}{dx}\left[\left(1+\tfrac{2}{5}\tfrac{2\pi}{3}\rho Y\right)\rho\right]\\
&\quad+\tfrac{8}{35}\tfrac{d}{dx}\left[\left(1+\tfrac{12}{35}\tfrac{2\pi}{3}\rho Y\right)R_{11}\right]+\tfrac{124}{1225}\tfrac{2\pi}{3}\tfrac{R_{11}}{\rho}\tfrac{d\left(\rho^2 Y\right)}{dx}\\
&\quad-\sqrt{\pi}\sqrt{\theta}\left[\tfrac{32}{525}\rho\theta Y\tfrac{d\rho}{dx}\tfrac{dv}{dx}+\tfrac{16}{525}\rho^2\theta\tfrac{d}{dx}\left(Y\tfrac{dv}{dx}\right)\right]\\
&-\sqrt{\pi}\sqrt{\theta}\left[\tfrac{72}{875}\rho\tfrac{d}{dx}\left(Y\tfrac{dq}{dx}\right)-\tfrac{8}{75}q\tfrac{d}{dx}\left(Y\tfrac{d\rho}{dx}\right)-\tfrac{16}{2526}\rho q\tfrac{d^2Y}{dx^2}\right]\\
&-\sqrt{\pi}\sqrt{\theta}\left[\tfrac{3}{25}\rho\tfrac{d}{dx}\left(Y\tfrac{dm_{111}}{dx}\right)-\tfrac{37}{35}m_{111}\tfrac{d}{dx}\left(Y\tfrac{d\rho}{dx}\right)-\tfrac{41}{175}\rho m_{111}\tfrac{d^2Y}{dx^2}\right]\\
&\qquad\qquad=-\tfrac{3}{2}\left[\tfrac{16}{5}\rho\sqrt{\pi\theta}Y\right]m_{111}
\end{aligned}
\tag{3.27}
$$

### $\Delta$ Balance

$$
\begin{aligned}
&8\theta\tfrac{d}{dx}\left[\left(1+\tfrac{3}{5}\tfrac{2\pi}{3}\rho Y\right)q\right]\\
&-8\theta\tfrac{q}{\rho}\tfrac{d}{dx}\left[\left(1+\tfrac{4}{5}\tfrac{2\pi}{3}\rho Y\right)\rho\right]\\
&-\sqrt{\pi}\sqrt{\theta}\left[\tfrac{4}{3}\rho^2\theta\tfrac{d}{dx}\left(Y\tfrac{d\theta}{dx}\right)+\tfrac{8}{3}\rho\theta Y\tfrac{d\rho}{dx}\tfrac{d\theta}{dx}\right]\\
&-\sqrt{\pi}\sqrt{\theta}\left[\tfrac{8}{15}\rho^2\theta\tfrac{d}{dx}\left(Y\tfrac{d\left(\frac{\sigma_{11}}{\rho}\right)}{dx}\right)-\tfrac{32}{3}\rho\theta Y\tfrac{d\rho}{dx}\tfrac{d\left(\frac{\sigma_{11}}{\rho}\right)}{dx}\right]\\
&\quad-\sqrt{\pi}\sqrt{\theta}\left[\tfrac{1}{3}\rho\tfrac{d}{dx}\left(Y\tfrac{d\Delta}{dx}\right)-\tfrac{31}{45}\Delta\tfrac{d}{dx}\left(Y\tfrac{d\rho}{dx}\right)-\tfrac{4}{45}\rho\Delta\tfrac{d^2Y}{dx^2}\right]\\
&-\sqrt{\pi}\sqrt{\theta}\left[\tfrac{4}{7}\rho\tfrac{d}{dx}\left(Y\tfrac{dR_{11}}{dx}\right)-\tfrac{76}{105}R_{11}\tfrac{d}{dx}\left(Y\tfrac{d\rho}{dx}\right)-\tfrac{4}{105}\rho R_{11}\tfrac{d^2Y}{dx^2}\right]\\
&\qquad\qquad=-\tfrac{2}{3}\left[\tfrac{16}{5}\rho\sqrt{\pi\theta}Y\right]\Delta
\end{aligned}
\tag{3.28}
$$

### $R_{11}$ balance

$$
\begin{aligned}
&\tfrac{56}{15}\theta\tfrac{d}{dx}\left[\left(1+\tfrac{12}{35}\tfrac{2\pi}{3}\rho Y\right)q\right]\\
&\quad+\tfrac{56}{15}\theta\tfrac{q}{\rho}\tfrac{d}{dx}\left[\left(1+\tfrac{1}{2}\tfrac{2\pi}{3}\rho Y\right)\rho\right]\\
&\qquad+2\theta\tfrac{d}{dx}\left[\left(1+\tfrac{12}{35}\tfrac{2\pi}{3}\rho Y\right)m_{111}\right]-2\tfrac{m_{111}}{\rho}\theta\tfrac{d}{dx}\left[\left(1+\tfrac{11}{14}\tfrac{2\pi}{3}\rho Y\right)\rho\right]\\
&-\sqrt{\pi}\sqrt{\theta}\left[\tfrac{16}{45}\rho^2\theta\tfrac{d}{dx}\left(Y\tfrac{d\theta}{dx}\right)+\tfrac{32}{45}\rho\theta Y\tfrac{d\rho}{dx}\tfrac{d\theta}{dx}\right]\\
&\quad-\sqrt{\pi}\sqrt{\theta}\left[\tfrac{4}{45}\rho\tfrac{d}{dx}\left(Y\tfrac{d\Delta}{dx}\right)-\tfrac{76}{675}\Delta\tfrac{d}{dx}\left(Y\tfrac{d\rho}{dx}\right)-\tfrac{4}{675}\rho\Delta\tfrac{d^2Y}{dx^2}\right]\\
&-\sqrt{\pi}\sqrt{\theta}\left[\tfrac{88}{315}\rho\theta\tfrac{d}{dx}\left(Y\tfrac{d\sigma_{11}}{dx}\right)-\tfrac{28}{45}\theta\sigma_{11}\tfrac{d}{dx}\left(Y\tfrac{d\rho}{dx}\right)-\tfrac{3}{35}\rho\theta\sigma_{11}\tfrac{d^2Y}{dx^2}\right]\\
&-\sqrt{\pi}\sqrt{\theta}\left[\tfrac{44}{175}\rho\tfrac{d}{dx}\left(Y\tfrac{dR_{11}}{dx}\right)-\tfrac{2369}{2205}R_{11}\tfrac{d}{dx}\left(Y\tfrac{d\rho}{dx}\right)-\tfrac{1709}{8820}\rho R_{11}\tfrac{d^2Y}{dx^2}\right]\\
&\qquad\qquad=-\left[\tfrac{16}{5}\rho\sqrt{\pi\theta}Y\right]\left(\tfrac{1}{2}\theta\sigma_{11}+\tfrac{205}{168}R_{11}\right)
\end{aligned}
\tag{3.29}
$$

## 3.4 Model Reduction

The 26-moment equations resolve the interface and the Knudsen layers in front of it. In this research, the 26-moment equations are used to resolve the whole system in all three regions.

At and in front of the interface, where the real gas effects and the contributions due to the phase change are considerable, the added terms will show their influence in resolving the interface in high resolutions; however, they become negligible in bulk phases.

The EV26 equations can be simplified to either 13-moment or NSF equations by reducing the higher-order terms. To better understand the equations and these higher-order terms, this section presents how the 26-moment equations can be simplified to 13-moment and NSF equations.

### 3.4.1 13-Moment Equations

The difference between the 26-moment and 13-moment is the three added higher-order moments of $m_{ijk}$, $\Delta$ and $R_{ij}$ in deriving the 26-moment set of equations. The 26-moment equations are simplified to the 13-moment equations here by eliminating all terms with the higher moment contributions $m_{ijk} = \Delta = R_{ij} = 0$, as well as removing the balance equations of these moments. The 13-moment set of equations is presented below.

**Mass Conservation**

$$\rho v = J \tag{3.30}$$

**Momentum Balance**

$$\left(\begin{array}{c} \rho vv \\ +\left[\rho\theta(1+\frac{2\pi}{3}\rho Y)-\frac{2\pi}{3}\chi_1\rho^2\right] \\ +\left[1+\frac{2}{5}\frac{2\pi}{3}\rho Y\right]\sigma_{11} \\ -\frac{4}{5}\frac{\sqrt{\pi}}{\sqrt{\theta}}\rho^2 Y\left(\theta\frac{dv}{dx}+\frac{1}{10}\frac{d\left(\frac{q}{\rho}\right)}{dx}\right) \\ +\frac{\pi}{60}\left(\frac{d^2\left(Y\rho^2\theta\right)}{dx^2}+3Y\frac{d^2\left(\rho^2\theta\right)}{dx^2}-12Y\frac{d\rho}{dx}\frac{d(\rho\theta)}{dx}-\frac{1}{2}\theta\rho^2\frac{d^2Y}{d\rho^2}\frac{d\rho}{dx}\frac{d\rho}{dx}\right) \\ -\frac{2\pi}{15}\chi_3\left[\left(\rho\frac{d^2\rho}{dx^2}+\frac{1}{2}\frac{d\rho}{dx}\frac{d\rho}{dx}\right)-\frac{d\rho}{dx}\frac{d\rho}{dx}\right] \end{array}\right) = constant = P \tag{3.31}$$

**Internal Energy Balance**

$$\frac{d}{dx}\left[\begin{array}{c} \frac{3}{2}\rho v\theta \\ +\left(1+\frac{3}{5}\frac{2\pi}{3}\rho Y\right)q \\ -\frac{2}{3}\rho^2 Y\sqrt{\pi}\sqrt{\theta}\left(\frac{d\theta}{dx}+\frac{2}{5}\frac{d\left(\frac{\sigma_{11}}{\rho}\right)}{dx}\right) \end{array}\right] = -\left[\rho\theta(1+\frac{2\pi}{3}\rho Y)+\rho\theta(1+\frac{2}{5}\frac{2\pi}{3}\rho Y)\sigma_{11}\right]\frac{dv}{dx} \tag{3.32}$$

**Kinetic Stress Balance**

$$\begin{array}{l} \frac{5}{2}\rho\theta\left[1+\frac{3}{5}\frac{2\pi}{3}\rho Y\right]\frac{d\theta}{dx}+\theta\frac{d}{dx}\left[\left(1+\frac{3}{5}\frac{2\pi}{3}\rho Y\right)\sigma_{11}\right] \\ -\frac{\sigma_{11}}{\rho}\theta\frac{d}{dx}\left[\left(1+\frac{9}{10}\frac{2\pi}{3}\rho Y\right)\rho\right]-\sqrt{\pi}\sqrt{\theta}\left[-\frac{19}{5}\theta\frac{d}{dx}\left(\rho^2 Y\frac{dv}{dx}\right)\right] \\ -\sqrt{\pi}\sqrt{\theta}\left[\ +\frac{27}{50}\rho\frac{d}{dx}\left(Y\frac{dq}{dx}\right)-\frac{37}{30}q\frac{d}{dx}\left(Y\frac{d\rho}{dx}\right)-\frac{8}{75}\rho q\frac{d^2Y}{dx^2}\ \right] \\ \qquad\qquad = -\frac{2}{3}\left[\frac{16}{5}\rho\sqrt{\pi\theta}Y\right]q \end{array} \tag{3.33}$$

**Kinetic Heat Flux Balance**

$$\begin{array}{l} \frac{4}{3}\left[\rho\theta\left(1+\frac{2}{5}\frac{2\pi}{3}\rho Y\right)\right]\frac{dv}{dx}+\frac{8}{15}\frac{d}{dx}\left[\left(1+\frac{3}{5}\frac{2\pi}{3}\rho Y\right)q\right] \\ +\frac{2\pi}{3}\left[\frac{4}{25}q\right]\frac{1}{\rho}\frac{d\rho^2 Y}{dx}-\sqrt{\pi}\sqrt{\theta}\left[\frac{16}{45}\rho^2\frac{d}{dx}\left(Y\frac{d\theta}{dx}\right)+\frac{32}{45}\rho Y\frac{d\rho}{dx}\frac{d\theta}{dx}\right] \\ -\sqrt{\pi}\sqrt{\theta}\left[\frac{88}{315}\rho\frac{d}{dx}\left(Y\frac{d\sigma_{11}}{dx}\right)-\frac{304}{315}\sigma_{11}\frac{d}{dx}\left(Y\frac{d\rho}{dx}\right)-\frac{6}{35}\rho\sigma_{11}\frac{d^2Y}{dx^2}\right] \\ \qquad\qquad = -\left[\frac{16}{5}\rho\sqrt{\pi\theta}Y\right]\sigma_{11} \end{array} \tag{3.34}$$

### 3.4.2 NSF Equations

The 26-moment equations can be simplified to NSF equations.

The mass conservation equation stays the same

$$\rho v = J. \tag{3.35}$$

The kinetic stress and kinetic heat flux balance equations of the 26-moment equations that are found in (3.25) and (3.26), respectively, can be reduced to the NSF equations when only the 1st order terms are kept, and all higher-order terms such as the higher moments vanish. The simplified balances read

$$\tfrac{4}{3}\left[\rho\theta\left(1+\tfrac{2}{5}\tfrac{2\pi}{3}\rho Y\right)\right]\tfrac{dv}{dx} = -\left[\frac{16}{5}\rho\sqrt{\pi\theta}Y\right]\sigma_{11}, \tag{3.36}$$

for the kinetic stress balance, and

$$\tfrac{5}{2}\rho\theta\left[1+\tfrac{3}{5}\tfrac{2\pi}{3}\rho Y\right]\tfrac{d\theta}{dx} = -\frac{2}{3}\left[\frac{16}{5}\rho\sqrt{\pi\theta}Y\right]q, \tag{3.37}$$

for the kinetic heat flux balance.

By eliminating the higher-order contributions of kinetic stress and kinetic heat flux from the momentum and the internal energy balances of the 26-moment, they simplify to

$$\left(\begin{array}{c} \rho vv \\ +\left[\rho\theta(1+\frac{2\pi}{3}\rho Y)-\frac{2\pi}{3}\chi_1\rho^2\right] \\ +\left[1+\frac{2}{5}\frac{2\pi}{3}\rho Y\right]\sigma_{11}-\frac{4}{5}\frac{\sqrt{\pi}}{\sqrt{\theta}}\rho^2 Y\left(\theta\frac{dv}{dx}\right) \\ +\frac{\pi}{60}\left(\frac{d^2\left(Y\rho^2\theta\right)}{dx^2}+3Y\frac{d^2\left(\rho^2\theta\right)}{dx^2}-12Y\frac{d\rho}{dx}\frac{d(\rho\theta)}{dx}-\frac{1}{2}\theta\rho^2\frac{d^2Y}{d\rho^2}\frac{d\rho}{dx}\frac{d\rho}{dx}\right) \\ -\frac{2\pi}{15}\chi_3\left[\left(\rho\frac{d^2\rho}{dx^2}+\frac{1}{2}\frac{d\rho}{dx}\frac{d\rho}{dx}\right)-\frac{d\rho}{dx}\frac{d\rho}{dx}\right] \end{array}\right) = constant = P, \tag{3.38}$$

for the momentum balance, and

$$\frac{d}{dx}\begin{bmatrix} \frac{3}{2}\rho v\theta \\ +\left(1+\frac{3}{5}\frac{2\pi}{3}\rho Y\right)q-\frac{2}{3}\rho^2 Y\sqrt{\pi}\sqrt{\theta}\left(\frac{d\theta}{dx}\right) \end{bmatrix} = -\left[\rho\theta(1+\tfrac{2\pi}{3}\rho Y)+\rho\theta(1+\tfrac{2}{5}\tfrac{2\pi}{3}\rho Y)\sigma_{11}\right]\tfrac{dv}{dx}\ , \tag{3.39}$$

for the internal enrgy balance.

In the bulk phases, where the mass density gradients are negligible, it can be found that the stress and heat flux change with the gradients of velocity and temperature, respectively.

For the stress in bulk phases, equation (3.38) gives

$$S_{11} = \left[1+\frac{2}{5}\frac{2\pi}{3}\rho Y\right]\sigma_{11} - \frac{4}{5}\frac{\sqrt{\pi}}{\sqrt{\theta}}\rho^2 Y\left(\theta\frac{dv}{dx}\right), \tag{3.40}$$

and substituting the kinetic stress $\sigma_{11}$ from equation (3.36), gives viscous stresses in the Navier-Stokes form

$$S_{11} = -\left[\frac{5}{12}\frac{\sqrt{\theta}}{\sqrt{\pi}Y}\left[1+\frac{2}{5}\frac{2\pi}{3}\rho Y\right]^2+\frac{4\sqrt{\pi\theta}}{5}\rho^2 Y\right]\frac{dv}{dx}, \tag{3.41}$$

where the stress changes with the velocity gradient.

For the heat flux in bulk, equation (3.39) gives

$$Q = \left(1+\frac{3}{5}\frac{2\pi}{3}\rho Y\right)q - \frac{2}{3}\rho^2 Y\sqrt{\pi}\sqrt{\theta}\left(\frac{d\theta}{dx}\right), \tag{3.42}$$

and substituting the kinetic heat flux $q$ from equation (3.37), gives the heat flux in the Fourier law form

$$Q = -\left[\frac{75}{64}\frac{\sqrt{\theta}}{\sqrt{\pi}Y}\left[1+\frac{3}{5}\frac{2\pi}{3}\rho Y\right]^2+\frac{2\sqrt{\pi\theta}}{3}\rho^2 Y\right]\frac{d\theta}{dx}, \tag{3.43}$$

where the heat changes with the temperature gradient.

# Chapter 4

# Solving 26-Moment Equations

The 26-moment set of equations is solved numerically for the 1-D steady-system using MATLAB. The solution of the 26-moment equations gives the resolved phase interface in the non-equilibrium evaporation/condensation process in the small-scale system.

## 4.1 Defining the System

The geometry of the system is defined by inputting the total length of the container $L$ and the length of the liquid $L_0$ in the system.

Local equilibrium in the liquid is easily established, while it is established through the Knudsen layer in front of the interface in the vapour. Therefore, for full resolution of the

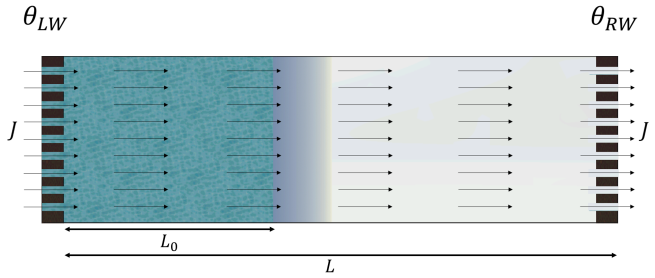


Figure 4.1: Steady-state 1-D non-equilibrium evaporation system with the two temperature boundaries, where $\theta = RT$ and it is the abbreviation of the temperature with the specific energy unit; $L$ and $L_0$ are the total length of the system and length of the liquid, respectively.

system in the non-equilibrium evaporation/condensation process, a larger vapour than the liquid region is chosen, see Figure 4.1.

### 4.1.1 Boundary Values

The other important controlled parameter is the mass flux $J$, which causes either the non-equilibrium evaporation or condensation depending on its direction. The positive mass flux leads to evaporation in the system, and condensation is modelled when the mass flux is negative. The mass withdrawn is added on another side to have the steady-state evaporation/condensation process. When the mass flux is zero, neither evaporation nor condensation occurs in the system.

Temperatures of the boundaries are the next controlling parameters of the system. Boundaries are in contact with the liquid and the vapour, and their temperatures stay constant in the process. The boundary temperatures could be controlled separately, such that the liquid boundary temperature $\theta_{LW}$ and the vapour boundary temperature $\theta_{RW}$ can be set as either identical or different.

Likewise, instead of the temperature boundary on the vapour side, the vapour boundary can be controlled as an adiabatic boundary in another studied configuration, where the heat flux becomes zero in the vapour.

The NSF equations are considered at the boundaries to have the boundary values for the higher moments. Hence, there are no physical walls on the two sides, but just the NSF regions from then on in both directions. It is helpful to check the convergence of the results from 26-moment equations with the NSF equations at boundaries far from the interface.

## 4.2 Methodology of Solving

The 26-moment set of macroscopic equations is solved numerically for the whole system with the defined boundary values using the finite differences with the following strategy:

The continuous domain is discretized.

Figure 4.2 shows how the container is split into the $N$ adjustable nodes in distance $\Delta x$; the first and the last nodes are shown in red to indicate the boundary nodes.

Compared to the interface's thickness, which is on the order of a few particles diameter, the bulk phase regions have significantly greater lengths; however, the system is discretized with the same length of $\Delta x$ in all three regions. As a result, considering enough nodes is necessary for resolving the interface accurately. Figure 4.3 shows the corresponded mass density curve of Figure 4.2 with the considered nodes. In this research, the emphasis is on getting the first results from the 26-moment equations and seeing how they describe the system, not optimizing the code by considering more node density in the interface region than the bulk regions.

The defined boundary conditions are set such that the NSF equations (3.35) to (3.39) hold in the boundary nodes. As a result, for the defined discretized system, the controlled boundary temperatures are considered for the values of the first and the last nodes as

$$\begin{aligned} (\theta)_1 &= \theta_{LW} \\ (\theta)_N &= \theta_{RW} \end{aligned} , \tag{4.1}$$

and for the adiabatic process, the boundaries are

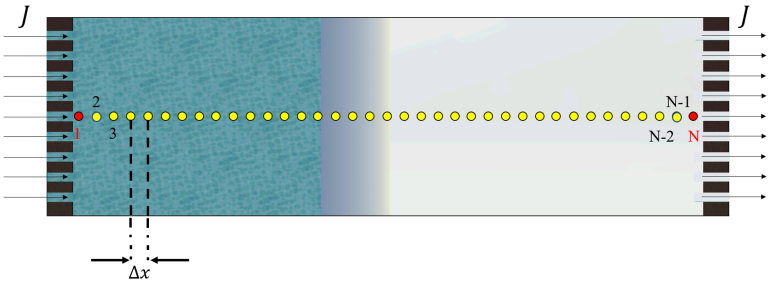


Figure 4.2: Steady-state 1-D system with two temperature boundaries, which is discretized into $N$ adjustable nodes for solving the system numerically using the finite differences.

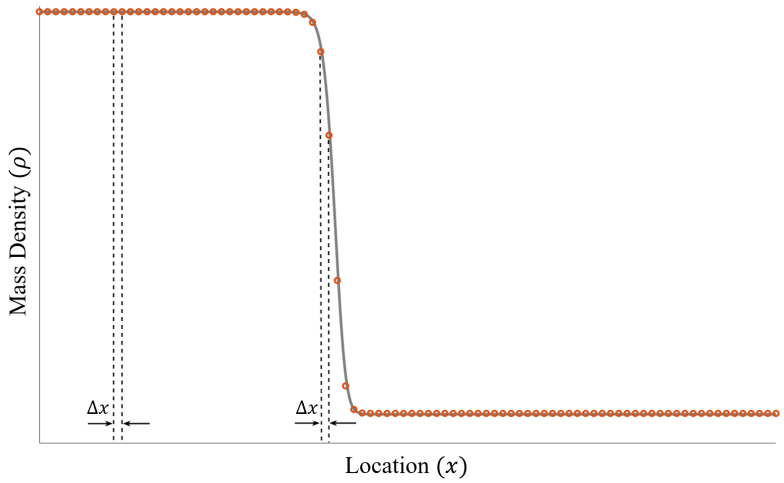


Figure 4.3: Mass density curve of the equilibrium state together with the considered nodes in the system, which shows that the density of nodes at the interface is lower than in the bulk phases.

$$\begin{matrix} (\theta)_1 = \theta_{LW} \\ \left(\frac{d\theta}{dx}\right)_N = 0 \end{matrix} . \tag{4.2}$$

Also, the boundary values of the stress and heat flux are considered from equations (3.41) and (3.43), respectively, and the added higher moments of $m_{111}$, $\Delta$, and $R_{11}$ are zero at the boundary nodes.

By defining the boundary conditions of the boundary nodes in the discretized system, for each of the other nodes in the system, the complete set of 26-moment equations are considered, and equations are solved to calculate the variables.

According to the derived transport equations, it is required to approximate the first and the second derivatives of the variables. The derivatives are approximated from the finite difference method with fourth-order accuracy [62].

## 4.3 Initial Guess

The 26-moment equations are solved for the defined discretized system using the *fsolve* command in MATLAB, which requires the initial guessed values. The *fsolve* command

is a way to solve the non-linear system of equations numerically. It attempts to solve the system of equations by minimizing the sum of the squares of the components, and when this summation becomes zero or near to zero, the system of equations is considered to be solved [63]. For this, $fsolve$ uses the trust regions algorithm, which is a powerful concept in optimization [63].

The trust-region algorithm minimizes the function by substituting the initial guessed value into the function and calculates the sum of the squares. Then, to improve the minimizing procedure by moving to a point with a lower function value, the algorithm approximates the function with a simpler function, which reasonably reflects the behaviour of the desired function in a neighbourhood around the initial guessed value. The considered neighbourhood is known as the trust region. The solver computes a trial step by minimizing over the trust region [63]. Then, if the trial point was leading to a smaller function value, the solver updates the current point to the trial point; otherwise, the current point remains unchanged, and the solver shrinks the trust region and repeats the trial step computation [63]. This procedure repeats until the minimizing procedure of the values in all functions to zero or almost zero has been achieved. Then the calculated points are shown as the numerical solution of the system of the non-linear set of equations. Thus, it needs good initial guessed values to work fast, and give meaningful results.

The appropriate initial guesses that are used for solving the 26-moment equations are found from the corresponding solution of the NSF equations. However, solving the NSF equations needs initial guessed values themselves. Therefore, the corresponding equilibrium state is solved and used as the required initial guess to solve NSF. Likewise, the initial guessed values are required to solve the equilibrium state. The appropriate initial guess for solving the equilibrium state is obtained by using the equal-area rule to find the saturation pressure, and the saturated mass densities at the temperature of the left boundary, which leads to guessing the mass density changes at the interface from a hyperbolic tangent function

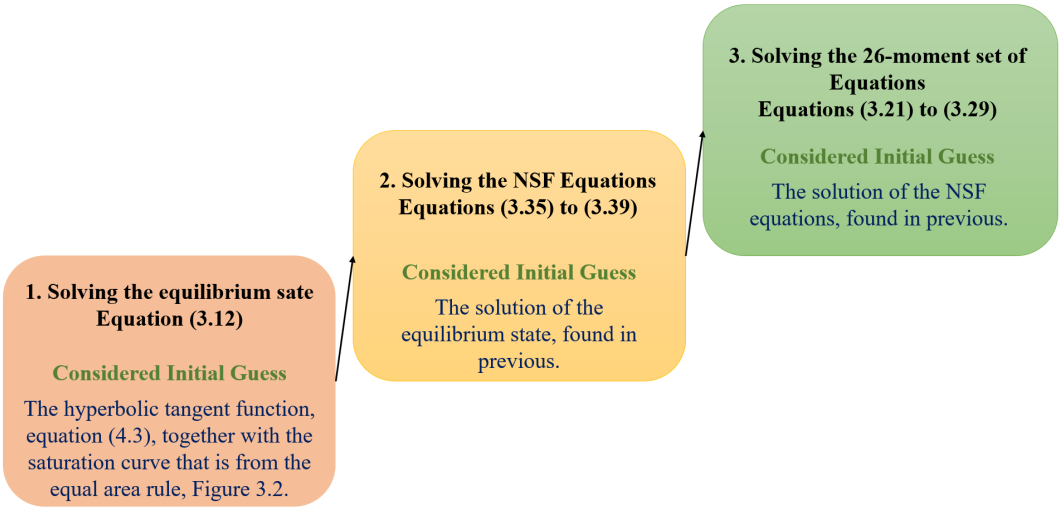


Figure 4.4: The procedure of finding the appropriate guessed values for solving 26-moment equations appropriately which is done in three steps, one after the other.

$$\rho_{guess} = \left[ (1 - \tanh(x - L_0)) \times \left( \frac{\rho_f - \rho_g}{2} \right) \right] + \rho_g, \tag{4.3}$$

where $L_0$ is the length of the liquid.

Hence, the procedure of finding the appropriate initial guessed values for solving the 26-moment equations is done in three steps, one after the other:

1. The equal-area rule and the hyperbolic tangent function, equation (4.3), are used to find the initial guess to solve the equilibrium state.

2. The solution of the equilibrium state is used as the initial guess to solve the NSF equations.

3. The solution of the NSF equations is considered as the required intial guess to solve the 26-moment equations.

Figure 4.4 shows the guessing procedure that is done for solving 26-moment equations.

## 4.4 26-Moment Results

Results from the 26-moment equations are presented and discussed for different processes here.

The 26-moment equations have eight independent variables, see equation (2.11), and their solutions give them through the system. As the overall heat flux $Q$ is required for determining the interface resistivities, see equation (1.1), the results present the overall non-convective heat flux $Q$, found in equation (3.6), instead of the kinetic heat flux $q$.

Solutions are presented for the equilibrium state, the non-equilibrium pure heat transfer process, the forced evaporation/condensation process with two temperature boundaries, and the evaporation/condensation process with the adiabatic vapour boundary. This helps not only to comprehend and discuss the system variables and their changes in the different processes, but it also shows the functionality of the 26-moment equations in describing different processes in the entire system at all three regions.

In this section, the solutions are found and presented for the different cases with the following specifications as the inputs

$$L = 250, L_0 = 40, \theta_{LW} = 0.55. \tag{4.4}$$

### 4.4.1 Equilibrium State

In the global equilibrium, the system is closed $J = 0$, and the boundary temperatures are identical $\theta_{RW} = \theta_{LW} = \theta_W = 0.55$. The equilibrium solution is straightforward, and the 26-moment results are presented in Figure 4.5, similar results were shown already earlier, see Figure 3.3.

As the system is closed, the equilibrium solution gives zero velocity. The boundary temperatures are also the same, which leads to the homogeneous temperature. The stress and the heat flux are zero in the system. The three non-equilibrium higher-order moments

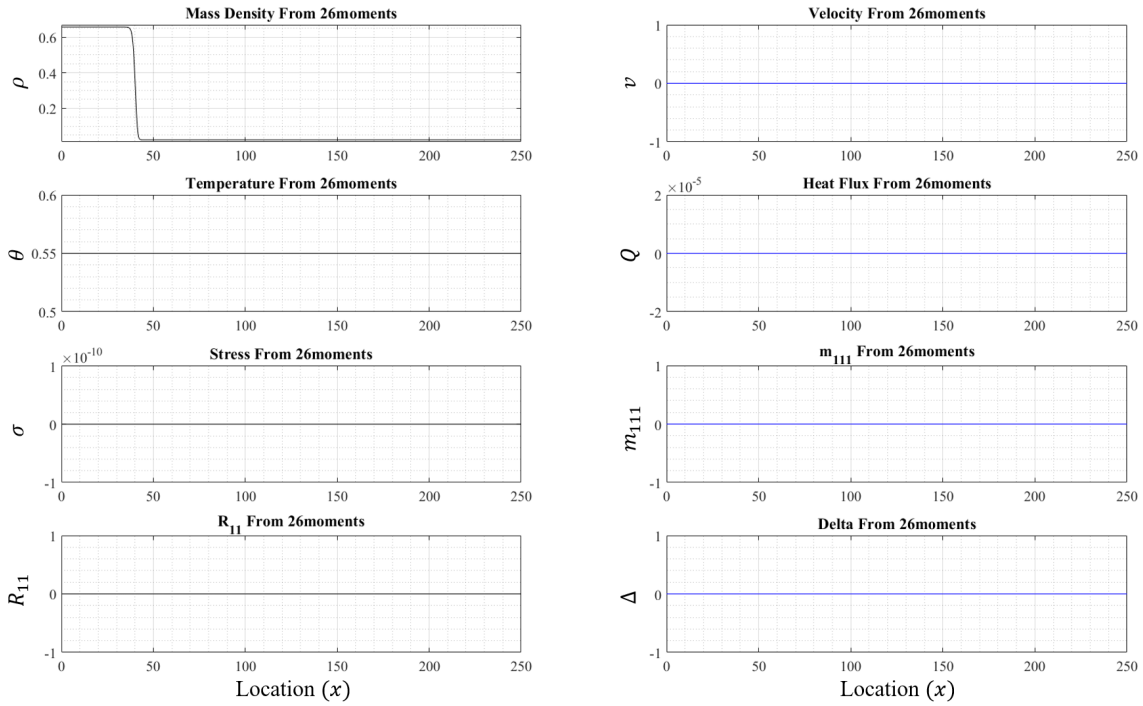


Figure 4.5: Solution of the 26-moment equations for the equilibrium state when $\theta_{RW} = \theta_{LW} = 0.55$. All the non-equilibrium variables are zero, the temperature is homogeneous, and the mass density is the only inhomogeneous variable at the interface due to the phase change .

of $m_{111}$, $\Delta$, and $R_{11}$ are zero.

However, the mass density is the only variable that is inhomogeneous at the interface, and it changes steeply but continuously from the saturated liquid mass density $\rho_f(\theta_W)$ to the saturated vapour mass density $\rho_g(\theta_W)$.

The inhomogeneous mass density at the interface is reasonable due to the phase change. To understand its reason from the equations, it is helpful to look at the 26-moment equations at the equilibrium state, where $v = q = \sigma = m_{111} = \Delta = R_{11} = 0$. It is found in Sec. 3.2 that at the equilibrium state, all the balances become zero except the momentum balance. Therefore, in the global equilibrium, the 26-moment set of equations for the 1-D steady-state system reduces to

$$\left(\begin{array}{c} \left[\rho\theta(1+\frac{2\pi}{3}\rho Y)-\frac{2\pi}{3}\chi_1\rho^2\right] \\ +\frac{\pi\theta}{60}\left(\frac{d^2(Y\rho^2)}{dx^2}+3Y\frac{d^2(\rho^2)}{dx^2}-12Y\frac{d\rho}{dx}\frac{d\rho}{dx}-\frac{1}{2}\theta\rho^2\frac{d^2Y}{d\rho^2}\frac{d\rho}{dx}\frac{d\rho}{dx}\right) \\ -\frac{2\pi}{15}\chi_3\left[\left(\rho\frac{d^2\rho}{dx^2}+\frac{1}{2}\frac{d\rho}{dx}\frac{d\rho}{dx}\right)-\frac{d\rho}{dx}\frac{d\rho}{dx}\right] \end{array}\right) = P = constant, \quad (4.5)$$

which is the simplified momentum balance of equation (3.23). It can be seen that the left hand side of the equation (4.5) should stay constant and equal to the system's pressure anywhere in the system. It is shown in Figure 3.3 that the van-der-Waals-like pressure gives the constat saturation pressure in bulk phases. However, at the interface, it has instabilities. As a result, the last two lines of equation (4.5), which are only functions of the mass density gradients stabilize the pressure in this region. Hence, an inhomogeneous mass density curve is found in the global equilibrium state.

The results show the homogeneous saturation pressure of $p_{sat}(\theta_W = 0.55) = 1.110 \times 10^{-2}$ in the system.

As all the non-equilibrium variables are zero in equilibrium, equation (4.5) that is found by simplifying the 26-moment equations can also be found from the momentum balance of the NSF equation (3.38). As a result, the same equilibrium result will be found by

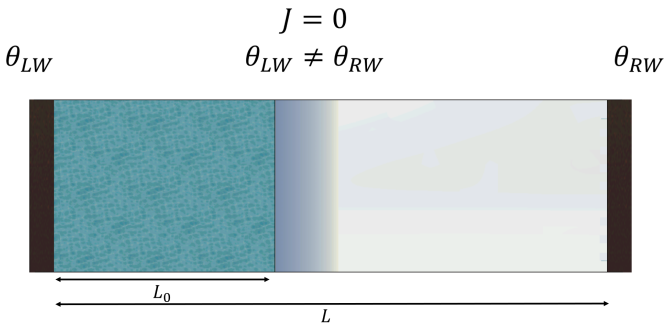


Figure 4.6: Steady-state 1-D non-equilibrium pure heat transfer system with two temperature boundaries, when $J = 0$, and $\theta_{LW} \neq \theta_{RW}$.

solving the NSF equations that consider the capillary stresses, equations (3.35) to (3.39). The solution of the 26-moment equations is found for the equilibrium state as a first test.

### 4.4.2 Pure Heat Transfer

A 1-D steady-state pure heat transfer is observed when the system is closed $J = 0$; while the boundary temperatures are different, so that the system is in a non-equilibrium state, however no evaporation/condensation occurs in the system, see Figure 4.6.

The 26-moment equations are solved for the pure heat transfer process when the vapour boundary temperature is controlled at $\theta_{RW} = 0.5501$, which is slightly higher than the controlled liquid temperature boundary $\theta_{LW} = 0.55$. The slight temperature difference between the two boundaries leads to a non-equilibrium state near equilibrium. As a result, the 26-moment solution can be considered as a benchmark for the processes with greater non-equilibrium strengths.

Figure 4.7 shows the temperature curve together with the mass density curve for the resolved system. Due to the solution's high resolution, the variables' changes from liquid to vapour across the interface are found as continuous but steep variations. On the other hand, in methods like the LIT that consider the NSF equations in liquid and vapour phases, the resolution is not high, and the variable changes from liquid to vapour at the sharp interface are considered as jumps.

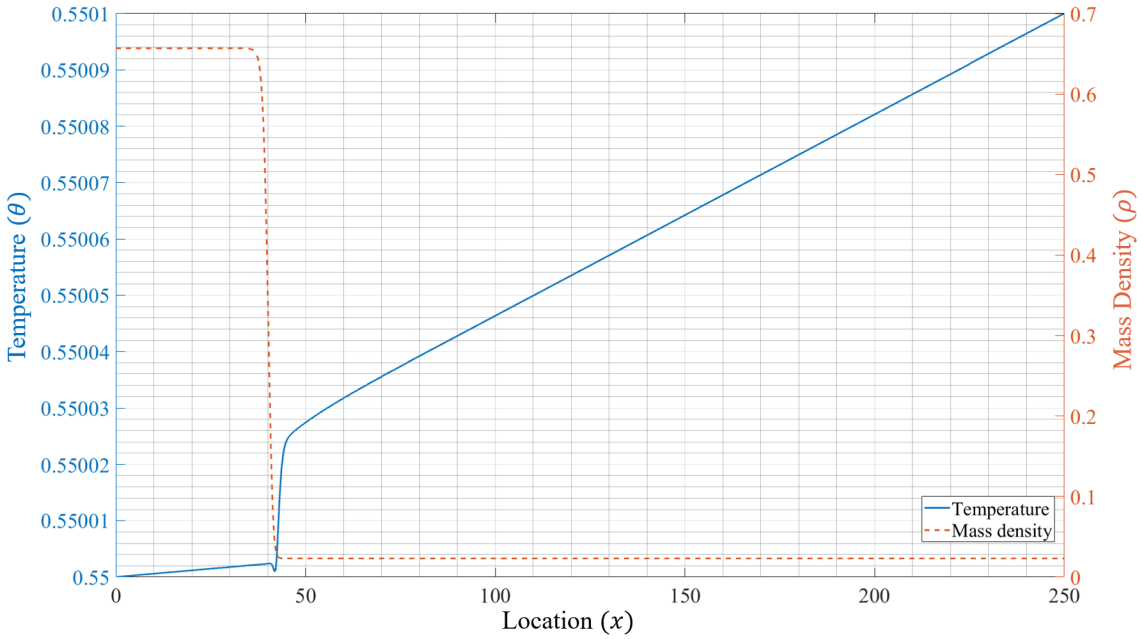


Figure 4.7: Temperature curve from the 26-moment equations in the non-equilibrium pure heat transfer process, together with the mass density when $J = 0$, $\theta_{LW} = 0.55$, and $\theta_{RW} = 0.5501$.

The mass density shows the interface structure, and it is almost the same as the equilibrium solution, shown in Figure 4.5 since the non-equilibrium strength is small.

The temperature changes in Figure 4.8 can be studied in each of the three regions. In the liquid and vapour bulks, the temperature gradient is positive. The temperature gradient is greater in the vapour phase than the liquid due to the greater heat conductivity of the liquid than the vapour. It can be seen that the temperature changes from liquid to vapour in a small length on the order of particle diameter across the interface. The temperature change from liquid to vapour indicates the temperature jump in the sharp interface model that is required for determining the interface resistivities.

The high-resolution solution shows an undershoot in temperature at the resolved interface. The undershoot lives in the interface; as a result, to model the interface from the LIT, which does not resolve the interface, the variations inside the interface region are not considered a part of the jumps, which are defined as the changes from liquid to vapour.

As the undershoot occurs in the thickness on the order of the particle diameter, it is

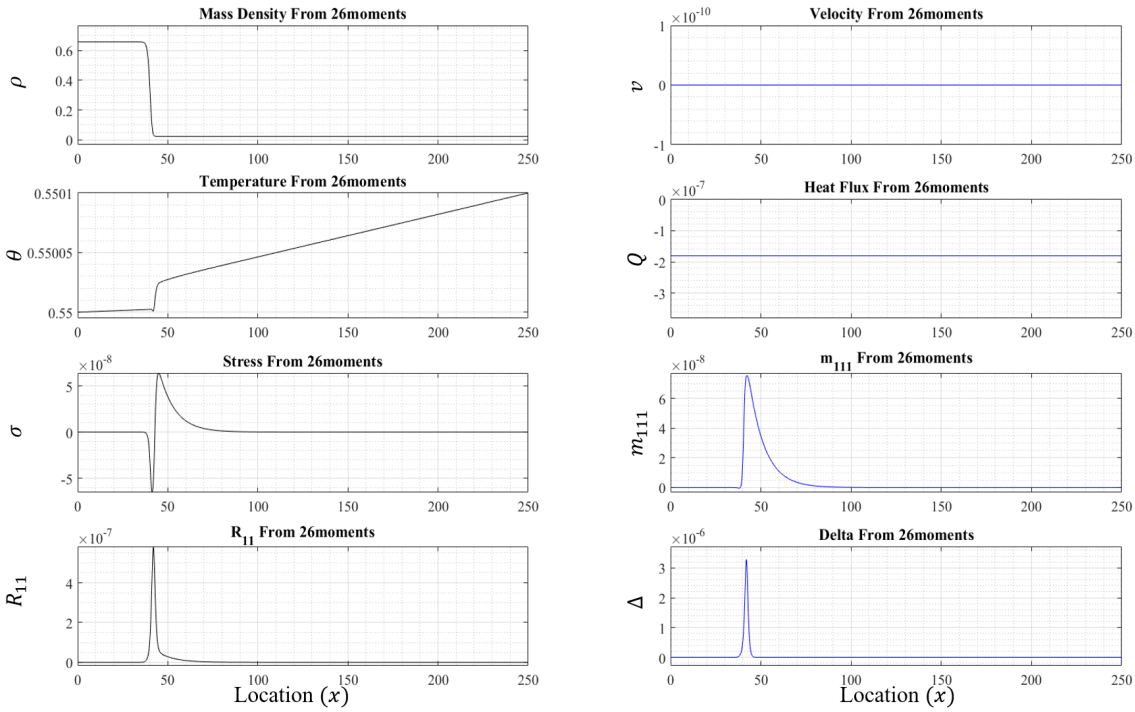


Figure 4.8: Changes of all eight system's variables from the 26-moment equations in the non-equilibrium pure heat transfer process when $J = 0$, $\theta_{LW} = 0.55$, and $\theta_{RW} = 0.5501$.

almost impossible to find out it really happens or not at the interface with measurements. It is shown that the measurements performed by Ward et al. [9–11] give the temperature changes at the interface as a jump between the liquid and vapour temperatures, see Figure 1.1b.

Also, maybe the temperature undershoot is the artifact of the numerics. However, to minimize the chance of this, the solution of the 26-moment equations is tested. For the test, the mass flux in each node is determined from the results to make sure that it stays constant in the system. It is most probable that the overshoot is considered in the 26-moment equations.

Since we are interested in determining the required jump and slip conditions, the resolved system is considered to find the changes from liquid to vapour and will be discussed in Chap. 5.

Figure 4.8 shows the 26-moment solution for all the variables in the defined non-equilibrium pure heat transfer process. It can be seen that all the variables are continuous,

and in the inhomogeneous variables, the steep changes occur at the interface. The system is closed $J = 0$, and the velocity vanishes.

The higher moments curves of $\sigma_{11}$, $m_{111}$, $\Delta$ and $R_{11}$ show that they stay non-zero in the small lengths in the vapour in front of the interface before becoming zero in the vapour bulk region. These results which are more marked and wider for $\sigma_{11}$ and $m_{111}$ visualize the Knudsen layers in front of the interface and indicate the high resolution of the 26-moment solution.

Figure 4.8 shows that the non-convective heat flux is homogeneous, and indicates that the higher-order moments stabilize the non-convective heat flux at and in front of the interface, see equation (3.6).

Finding the homogeneous non-convective heat flux at the interface region shows that the steep changes of variables in the interface region, like the temperature undershoot, work appropriately in defining the system.

Normal stress is constant, and in bulk phases, this is only pressure, which means that the bulk pressures are constant, but due to the non-equilibrium process, pressure differs from the saturation pressure.

Figure 4.9 shows the steady-state heat transfer when the vapour boundary temperature is $\theta_{RW} = 0.5499$, which is slightly lower than the liquid boundary temperature $\theta_{LW} = 0.55$. Comparing the results found in Figure 4.8 with Figure 4.9 shows that the temperature is now decreasing and the non-convective heat flux is positive. Also, the higher-order moments are similar but with opposite signs.

### 4.4.3 Forced Evaporation/Condensation

As shown in Figure 4.10, the forced evaporation/condensation process occurs when the controlled mass flux is non-zero, while the boundaries are controlled either at the same or different temperatures.

The 26-moment results are presented in Figure 4.11 in the forced non-equilibrium evap-

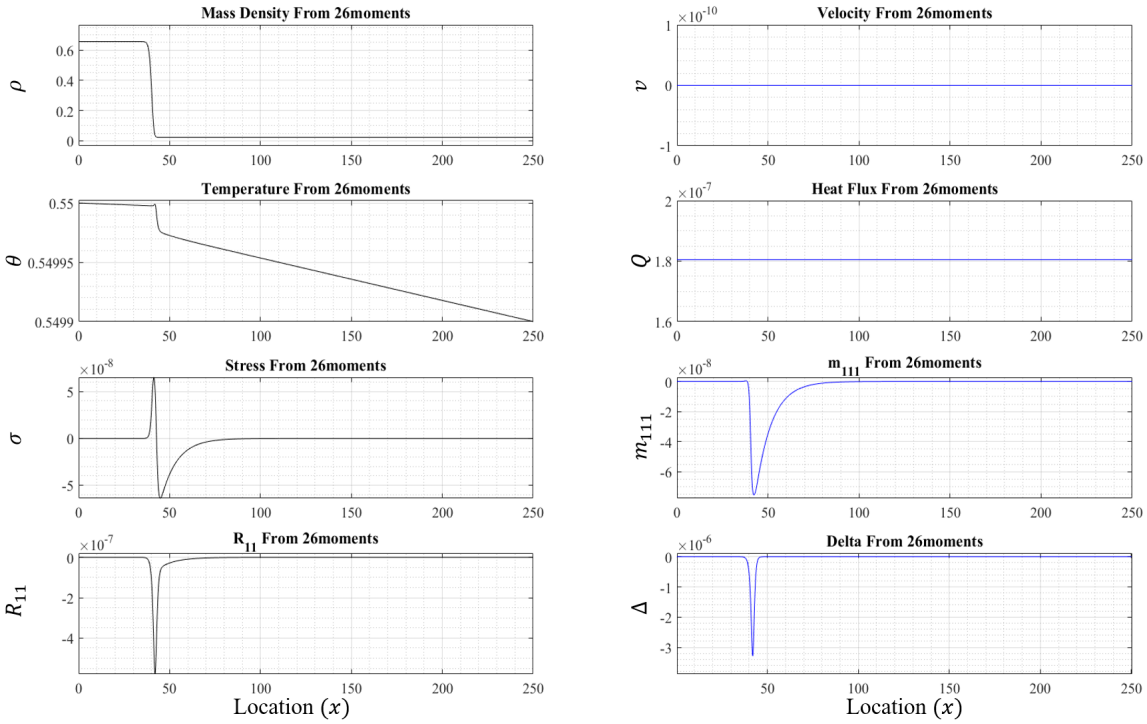


Figure 4.9: Changes of all eight system's variables from 26-moment equations in the non-equilibrium pure heat transfer process when $J = 0$, $\theta_{LW} = 0.55$ and $\theta_{RW} = 0.5499$

oration process when the mass flux is $J = 10^{-5}$, and the boundary temperatures are controlled at $\theta_{RW} = \theta_{LW} = \theta_W = 0.55$ which is relatively far from the critical temperature and pressure is small. The small positive prescribed mass flux leads to non-equilibrium evaporation near the equilibrium that can be used as a benchmark for comparing the results with the results of the experiments.

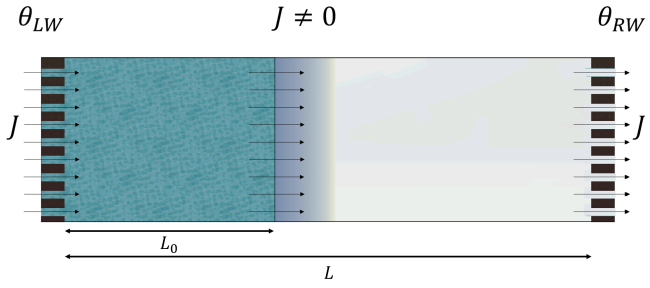


Figure 4.10: Steady-state 1-D non-equilibrium evaporation system with two temperature boundaries, when $J = 10^{-5}$, and $\theta_{LW} = \theta_{RW} = 0.55$

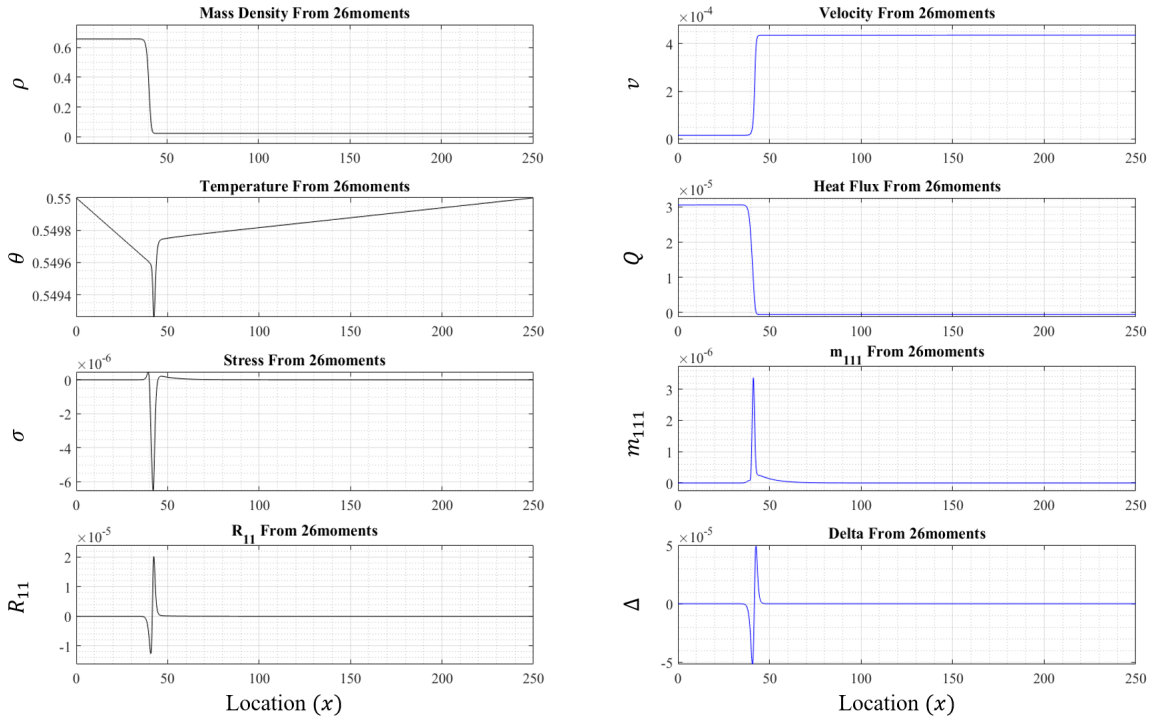


Figure 4.11: Changes of all eight system's variables from 26-moment equations in the non-equilibrium forced evaporation process, when $J = 10^{-5}$, and $\theta_{LW} = \theta_{RW} = 0.55$.

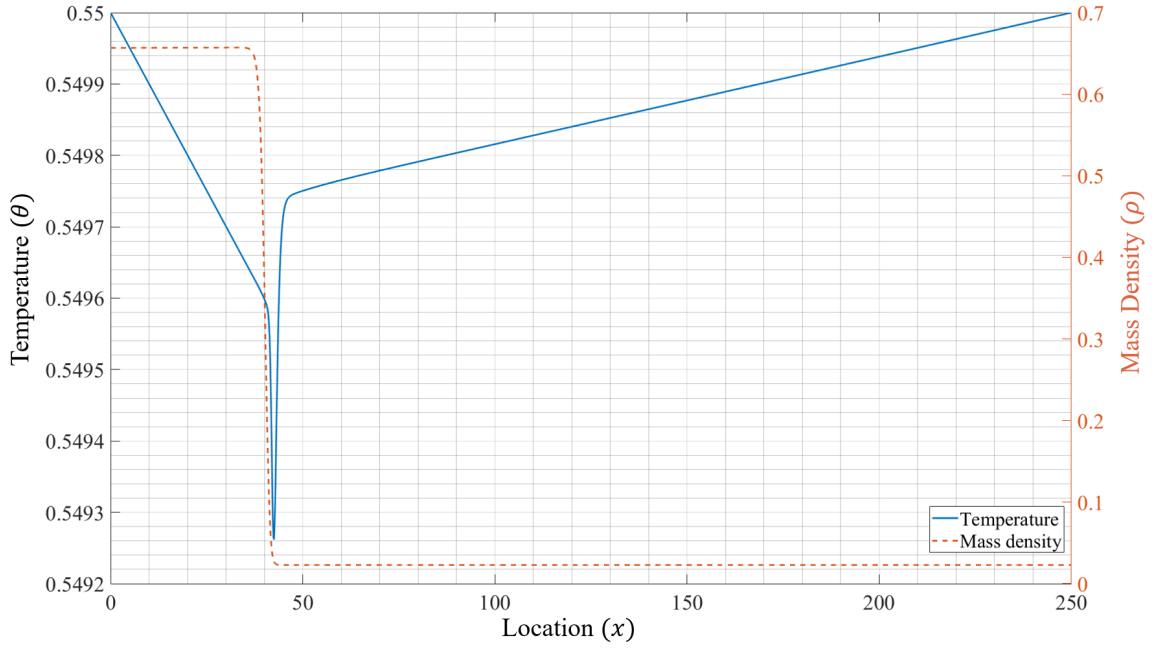


Figure 4.12: Temperature curve from 26-moment equations in the non-equilibrium forced evaporation process, when $J = 10^{-5}$, and $\theta_{LW} = \theta_{RW} = 0.55$.

Since the controlled mass flux is small, the mass density in Figure 4.11 is found similar to the equilibrium solution, shown in Figure 4.5. According to the mass conservation $v = \frac{J}{\rho}$, so the velocity is found greater in the vapour than in the liquid. Similar to the other variables, velocity changes at the interface are continuous but steep.

The non-convective heat flux in Figure 4.11 is positive in the liquid bulk, and its magnitude is greater than the negative heat flux of the vapour bulk. This shows that the heat of evaporation mainly comes from the liquid. As a result, Figure 4.12 shows that the temperature of the liquid phase is reduced more than the temperature of the vapour at the interface. This leads to having a considerable temperature difference from liquid to vapour, which is a temperature jump across the interface.

Also, as it was explained earlier, the undershoot of the temperature lives in the interface region, and it is considered in the 26-moment equations. It is a property of the interface which is found by resolving the interface in high resolution. As a result, it is not a part of the temperature jump from liquid to vapour, which is required for modelling the interface using the LIT with no high resolutions.

According to the visualized interface structure in Figure 4.12, the temperature variations occur more in front of the interface, which shows the importance of the dense vapour effects in the Knudsen layers on the resolved solution.

The Knudsen layers are visualized in higher moments curves, in particular $m_{111}$, which is shown in Figure 4.13.

Figure 4.14 shows the temperature curve found from the 26-moment and the NSF equations. The NSF equations could not resolve the interface and the temperature from the NSF shows the identical temperatures for both phases at the interface. However, the 26-moment equations with many contributions above the NSF resolve the system and predict the jump-like temperature change between the two phases across the interface. Also, the system pressure is found $p = 1.104 \times 10^{-2}$ which is smaller than the saturation pressure.

Comparing the temperature curve shown in Figure 4.12 as a benchmark with the Ward

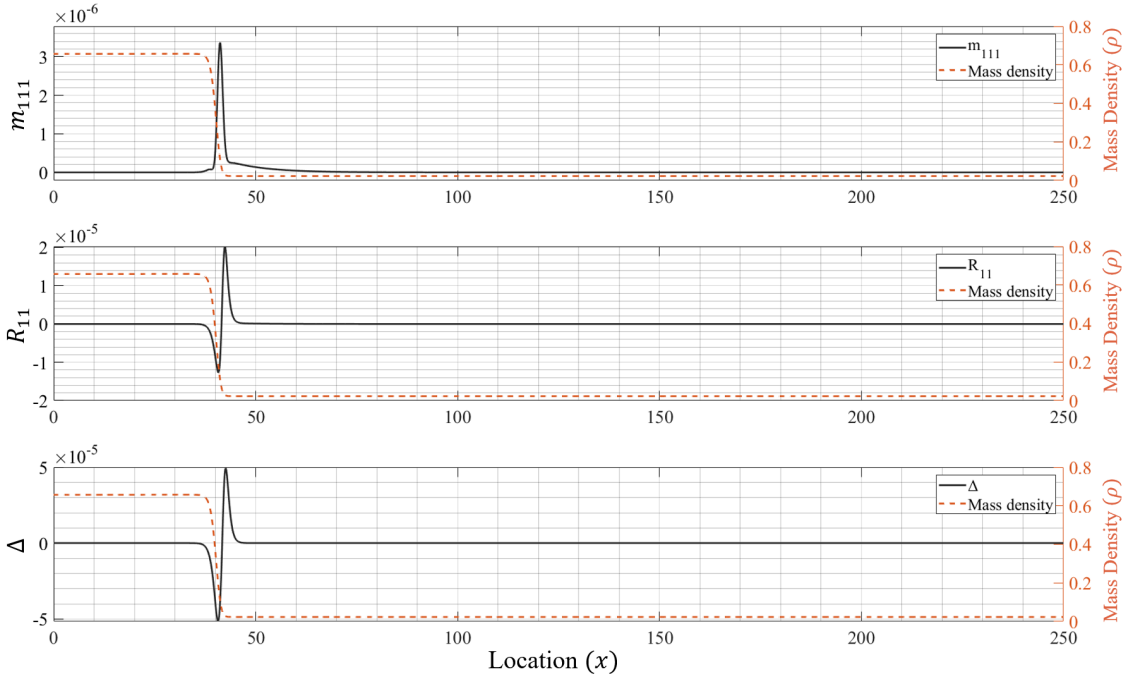


Figure 4.13: The higher-order moments in the non-equilibrium forced evaporation process, when $J = 10^{-5}$ and $\theta_{LW} = \theta_{RW} = 0.55$, together with the mass density curve.

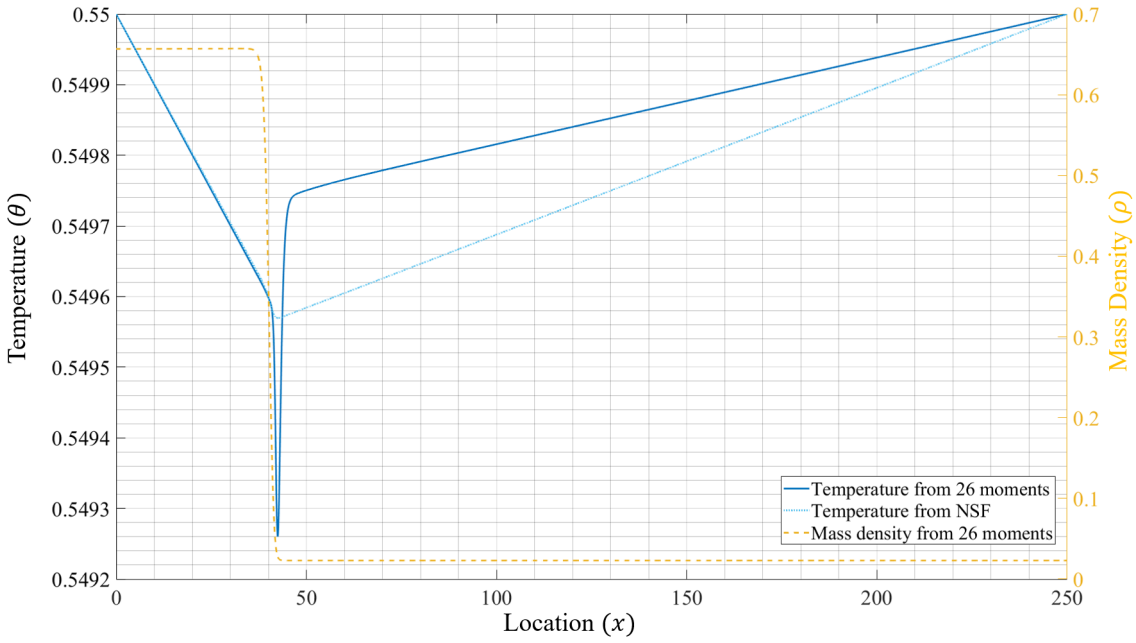


Figure 4.14: Comparing the temperature curve found from the 26-moment equations with the NSF result both in the non-equilibrium forced evaporation process, when $J = 10^{-5}$ and $\theta_{LW} = \theta_{RW} = 0.55$, together with the interface structure. The resolved solution from the 26-moment equations shows the temperature variations from liquid to vapour at the interface. In contrast, the result from NSF equations gives no changes in temperatures of the two phases at the interface.

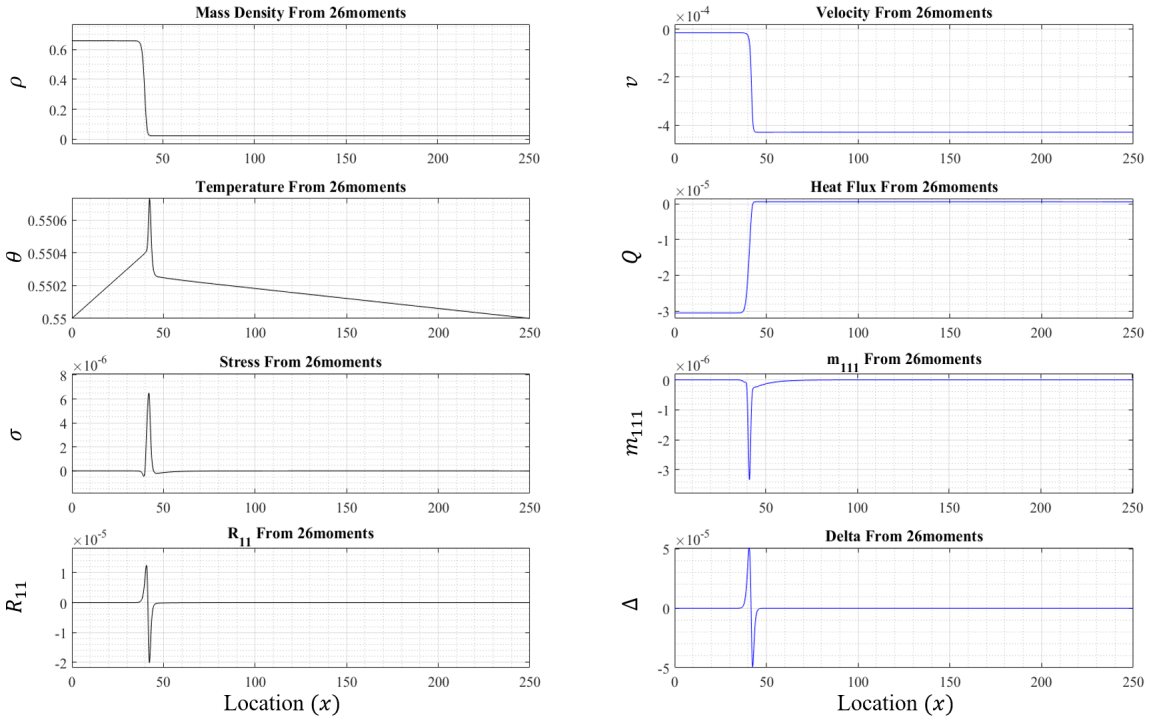


Figure 4.15: Changes of all eight system's variables from the 26-moment equations in the non-equilibrium forced condensation process, when $J = -10^{-5}$, and $\theta_{LW} = \theta_{RW} = 0.55$.

et al. experiment observation, which is also found for low temperatures [10], shown in Figure 1.1b, indicates agreements in principle.

The 26-moment result for the evaporation process with small prescribed mass flux at the relatively low temperature predicts the direction of the temperature changes from liquid to vapour, similar to the experimental results.

The magnitude of the temperature jump at the phase interface from the 26-moment looks larger than the negligible temperature jump that was found based on classical kinetic theory.

The non-equilibrium forced condensation process is modelled by prescribing the negative mass flux of $J = -10^{-5}$ and controlling the boundary temperatures at 0.55. The results are shown in Figure 4.15.

Because of the mass density difference of the two phases, the magnitude of the velocity is greater in the vapour than in the liquid. The non-convective heat flux in Figure 4.15

shows that the heat of condensation is absorbed by the liquid and vapour at the interface differently. The main part of the heat of condensation is absorbed by the liquid and increases the liquid temperature more than the vapour temperature at the interface. Also, the system pressure is found $p = 1.118 \times 10^{-2}$, which is greater than the saturation pressure.

As discussed, the Knudsen layers can be found in the higher-order moment curves, shown in Figure 4.15.

### 4.4.4 Adiabatic Vapour Boundary

The 26-moment equations are solved in the forced evaporation process with the adiabatic vapour boundary. The results are found by replacing the temperature boundary on the vapour side with the adiabatic boundary that is presented in equation 4.2.

The 26-moment equations are solved and presented in Figure 4.16 when the controlled mass flux is $J = 10^{-5}$. As shown in Figure 4.16, the adiabatic vapour boundary leads to a flat temperature profile in bulk vapour and zero non-convective heat flux in this region. The bulk vapour region temperature in the adiabatic process is constant and it is almost equal to the vapour temperature at the interface.

For the small prescribed mass flux and at the relatively low controlled temperature of the liquid boundary, the temperature curve shows that the liquid has a lower temperature than the vapour at the interface.

The solution of the 26-moment equations for the adiabatic vapour process is compared with the DSMC results found by Frezzotti et al. for a similar adiabatic evaporation process [34]. However, there are some differences between the system that is studied in this research and the system studied by Frezzotti et al. [34].

In Frezzotti et al. simulation setup, a liquid film is initially at the equilibrium with its vapour phases that are considered on both sides [34]. This means that the liquid film is at the center of the two vapour phases. Each of the vapour phases is delimited by a perfectly reflecting piston that can move. The evaporation process starts when both pistons

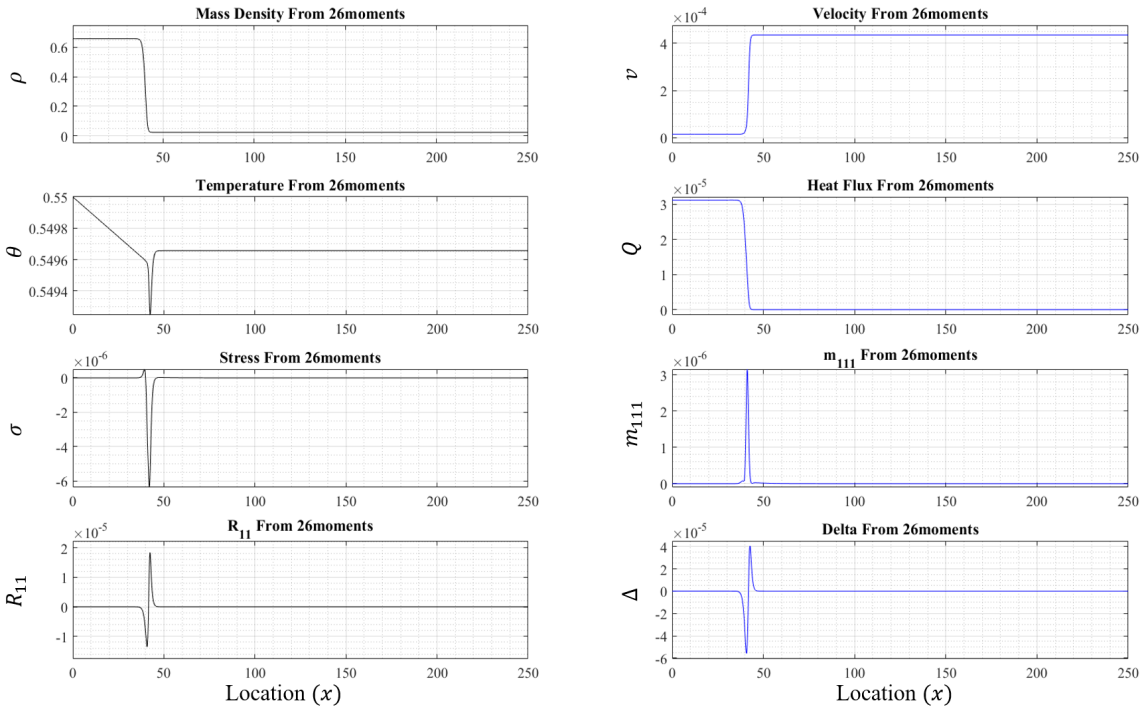


Figure 4.16: Changes of all eight system's variables from 26-moment equations in non-equilibrium adiabatic forced evaporation process, when $J = 10^{-5}$, and the liquid boundary temperature is controlled at $\theta_{LW} = 0.55$.

move with the constant speeds of $\pm V_p$ to the right and the left sides, respectively [34]. In the evaporation process, the liquid length becomes thinner due to the evaporation, and the process is unsteady because of the motion of the interfaces and pistons [34]. However, Frezzotti et al. found that the temperature of the liquid at the interface starts to stay constant after an initial rapid decrease [34]. As a result, they assumed that the process could be considered as a steady-state process after reaching this approximately constant interface temperature [34].

The 26-moment equations are solved for the relatively large mass flux of $J = 9 \times 10^{-4}$, and the liquid temperature boundary of 0.55. Figure 4.17 compares the temperatures from the moment equations with the DSMC results. The figure shows that the temperature curves are not fully similar, however, they both show the same direction of the temperature changes from liquid to vapour across the interface.

Furthermore, Figure 4.17 shows some differences between the temperature curves found

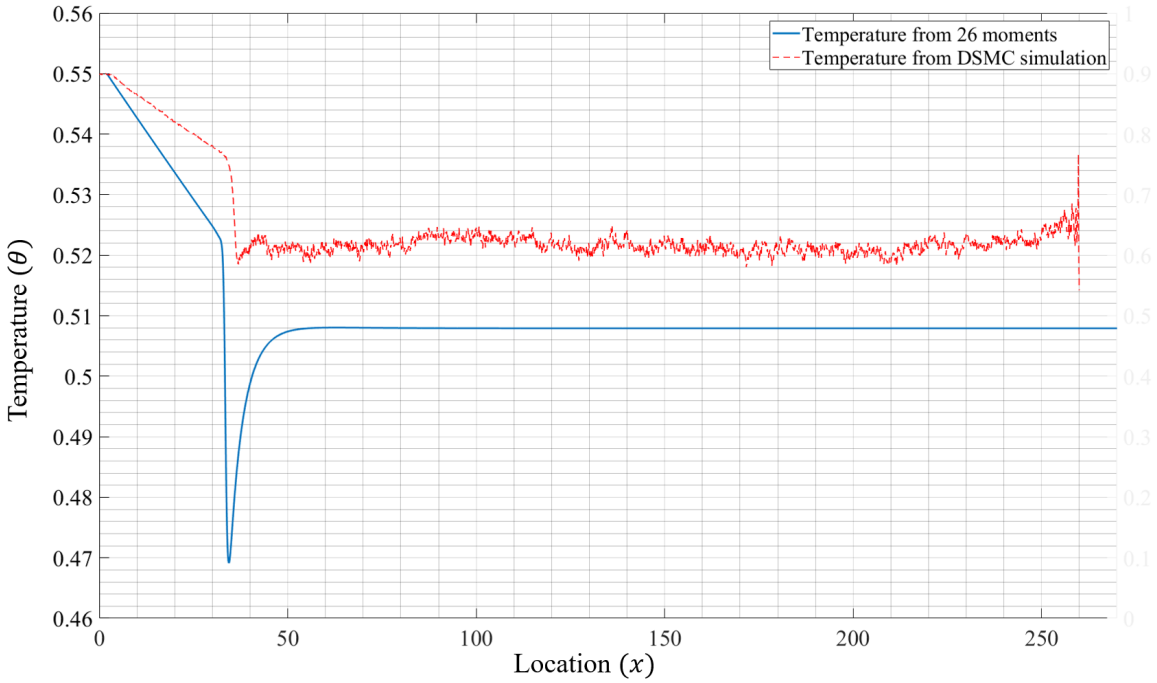


Figure 4.17: Comparing the temperature curve found from the 26-moment equations in the non-equilibrium evaporation process with the adiabatic vapour boundary, when $J = 9 \times 10^{-4}$, and $\theta_{LW} = 0.55$, with the DSMC results found by Frezzotti et al. [34] for a similar process. The results from the two methods are not fully the same, mainly due to the differences in the two systems' setups, but they both show the same direction of the temperature jump at the interface.

from the two methods. The temperature from the moment equations has a larger slope than the DSMC results in liquid bulk. In vapour bulk, the scattered DSMC result shows a greater temperature than the predicted temperature from the 26-moment equations. The temperature undershoot in the interface region is greater in the 26-moment results than the DSMC results.

These differences might be because of the different setups of the two methods; for instance, due to the moving liquid-vapour interface in the DSMC simulation, finding the exact corresponding $L_0$, as one of the required inputs for solving the 26-moment equations was not possible. Also, maybe the steady-state process was not fully reached in the DSMC results, and the process should be continued for a longer time before considering it as a steady-state process. Besides, the 26-moment equations are partly-linearized for the small deviations from the equilibrium and Taylor series are used for approximating the Enkog term. Therefore, it is possible that for the relatively large mass flux of $J = 9 \times 10^{-4}$, the linearizations lead to some error.

Comparing the directions of the temperature changes found in Figure 4.17 with Figure 4.16, shows that the temperature jump direction has been changed by the relatively large controlled mass flux. For the relatively large mass flux of $J = 9 \times 10^{-4}$, the liquid temperature is higher than the vapour temperature, which was in the opposite direction for the smaller controlled mass flux of $J = 10^{-5}$ that was shown in Figure 4.16.

From the interface resistivities point of view, this change in the direction of the temperature variations at the resolved interface shows that the off-diagonal interface resistivities might change not in magnitude only depending on the system's properties but also in their signs. The interface resistivities will be discussed in detail in Chp. 5.

### 4.4.5 Higher Moments

It is seen in the 26-moment results that the higher moments visualize the Knudsen layers in front of the interface. Here the higher-order moments are compared in the processes

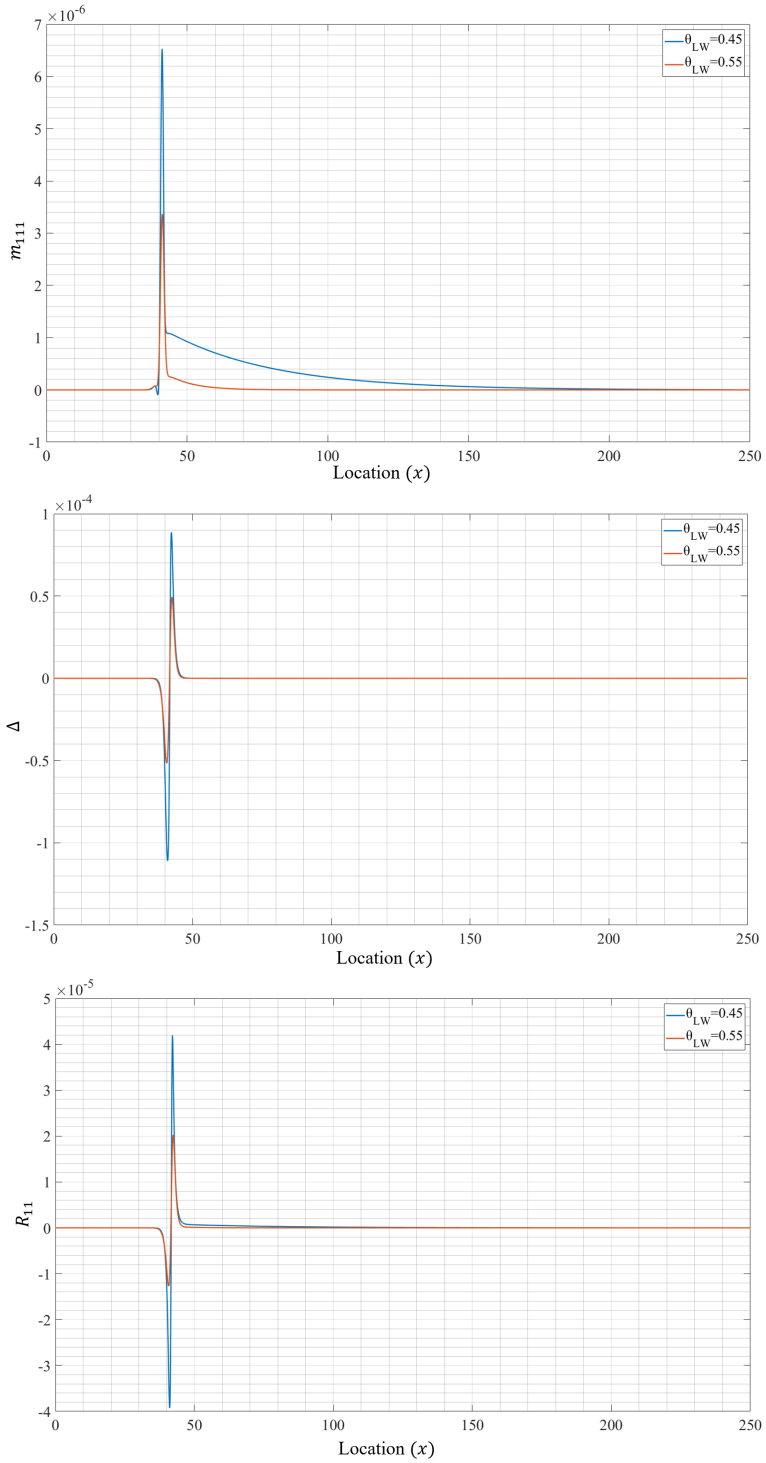


Figure 4.18: Comparing the higher-order moments found from the 26-moment equations in non-equilibrium forced evaporation process when $J = 10^{-5}$, at two identical boundary temperatures of $\theta = 0.45$ and $\theta = 0.55$.

with different boundary temperatures and mass fluxes. The effects of interface temperature and mass fluxes on the interface conditions will discuss in more detail in Chap. 5 with determining the interface resistivities.

At the low temperatures, as shown in Figure 3.2, pressure is lower, and the mean free path is larger.

Figure 4.18, shows a comparison between the higher moments at two temperatures of $\theta_{LW} = 0.45$ and $\theta_{LW} = 0.55$, with the same controlled mass flux of $J = 10^{-5}$. At the interface, all the three added higher moments show around doubled values at the lower temperature of $\theta_{LW} = 0.45$ than $\theta_{LW} = 0.55$. At the lower temperature, the transition layers are wider than at the higher temperature. This shows that the real gas effects remained considerable for a greater distance in front of the interface at the lower temperature. The differences are considerable in $m_{111}$, while only minor changes are observed in $R_{11}$ and $\Delta$.

In order to visualize the non-equilibrium strength effects on the interface conditions, the higher-order moments are compared for different controlled mass fluxes when the boundary temperatures are kept at 0.55.

The higher-order moments in Figure 4.19, show the importance of the strength of the non-equilibrium process. At the interface, the magnitudes of the higher-order moments are greater for the larger mass fluxes. For the larger mass fluxes, the transition layers are wider than at the higher temperature.

The higher-order moments affect the other system variables, in particular the temperature. Figure 4.20 shows the temperature curves for the three different controlled mass fluxes. It can be seen that the jump-like changes and the temperature of the two phases at the interface are changed for different systems.

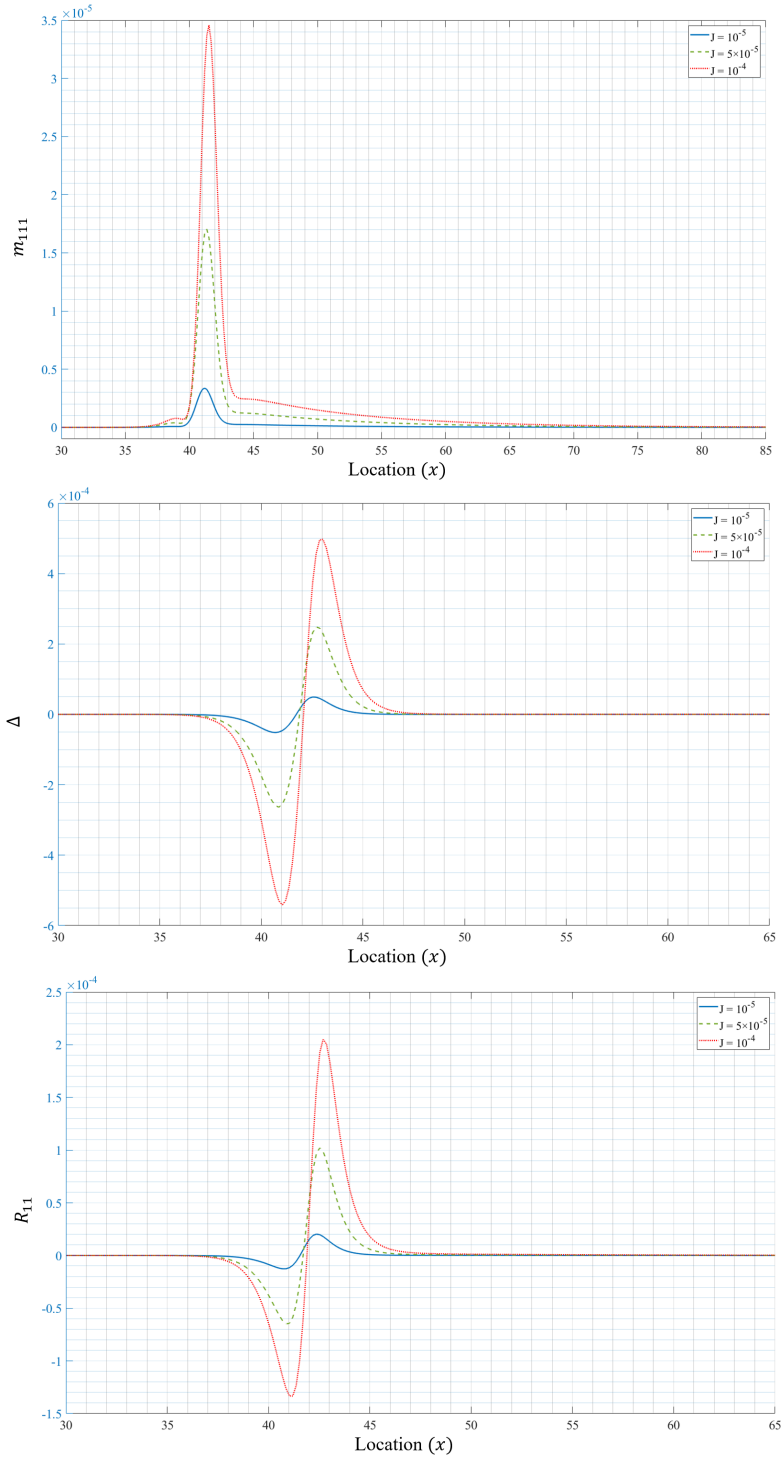


Figure 4.19: Comparing the higher-order moments found from the 26-moment equations in non-equilibrium forced evaporation with identical temperature boundaries at $\theta_{LW} = \theta_{RW} = 0.55$, for three different mass fluxes.

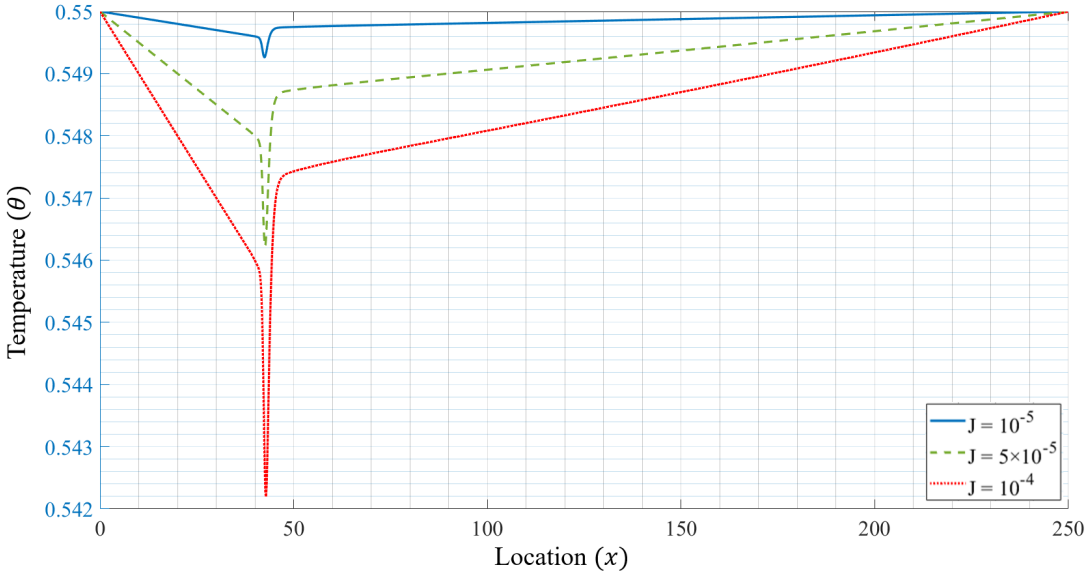


Figure 4.20: Comparing the temperature curves found from the 26-moment equations in non-equilibrium forced evaporation with identical temperature boundaries at $\theta_{LW} = \theta_{RW} = 0.55$, for three different controlled mass fluxes. The changes in the magnitude of the steep variations of the temperature at the interface in processes with different temperatures of the interface and the controlled mass fluxes can be seen clearly.

# Chapter 5

# Interface Resistivities

The resolved interface, which is found by solving the 26-moment equations, shows that the thickness of the interface plus the Knudsen layers, where the system's variables change continuously and steeply, is on the order of ten particle diameters. Therefore, when resolving the interface in high resolutions is required, the 26-moment set of macroscopic equations can be used as an alternative method to the costly and time-consuming methods like MD or DSMC.

However, typically, in the experiments and simulations, resolving the interface in high resolutions is not required, and it is sufficient to consider the changes of the variables from liquid to vapour as jumps at the sharp interface.

The sharp interface method, based on the LIT, can be used to model the interface if the interface resistivities are available [20, 21]. Determining the interface resistivities is challenging and the classical macroscopic thermodynamics can not calculate them. Hence, the resolved liquid-vapour interface that is found by solving the 26-moment equations is used to determine the interface resistivities from the LIT by extracting the jump and slip conditions.

In this chapter, the interface resistivities are determined based on the solution of the 26-moment equations for the LIT as functions of the liquid's temperature at the interface

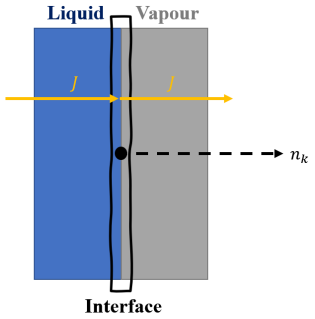


Figure 5.1: The schematic of the sharp interface. Based on the LIT, the NSF equations are valid in each phase, while jump and slip conditions need to be considered at the interface

and the non-equilibrium strength.

## 5.1 Linear Irreversible Thermodynamics (LIT)

In order to model the interface, the LIT method formulates the entropy production at the interface. For this, bulk phases are assumed at the local equilibrium, which means that the NSF equations are valid in each of the two phases. While at the sharp interface, jump and slip conditions need to be considered. Therefore, for the two phases at the interface, the NSF conservation laws are written with the jump conditions to find the entropy production $\sigma_S$ in the general form of

$$\sigma_S = \sum_A X_A J_A \geqslant 0, \tag{5.1}$$

where $X_A$ is the thermodynamic forces, and $J_A$ denotes the thermodynamic fluxes.

As shown in Figure 5.1, for the 1-D steady-state system with the normal $n$ that points to the vapour, the entropy production $\sigma_S$ can be formulated by writing the NSF balances in the jump form of

$$[\![\vartheta]\!] = \vartheta_V - \vartheta_L, \tag{5.2}$$

where $\vartheta$ is an arbitrary property, and $[\![\vartheta]\!]$ is the difference between the vapour $V$ and the

liquid $L$ properties at the interface. The NSF equations are written at the interface by ignoring the viscous stresses at the interface and choosing a viewpoint resting with the interface, which means that the velocities are measured relative to the interface.

The mass conservation reads

$$[\![\rho v]\!]\, n = 0 \Longrightarrow J_V - J_L = 0 \Longrightarrow J_V = J_L = J. \tag{5.3}$$

The momentum balance reads

$$[\![\rho vv + p]\!]\, n = 0 \Longrightarrow J\,[\![v]\!] + [\![p]\!]\, n = 0 \Longrightarrow p_V - p_L = 0 \Longrightarrow p_V = p_L = p, \tag{5.4}$$

where due to the smallness of the velocity at the interface, the term $Jv$ which is quadratic with the velocity is extremely small, and it is ignored.

The internal energy balance reads

$$[\![\rho hv + Q]\!] = 0 \Longrightarrow J\,[\![h]\!]\, n + [\![Q]\!] = 0 \Longrightarrow Jh_V + Q_V = Jh_L + Q_L, \tag{5.5}$$

where $h(\rho,\theta)$ is the enthalpy.

Finally, the entropy balance reads

$$\left[\!\!\left[\rho sv + \frac{Q}{\theta}\right]\!\!\right] n = \sigma_S \geqslant 0 \Longrightarrow J\,[\![s]\!]\, n + \left[\!\!\left[\frac{Q}{\theta}\right]\!\!\right] = \sigma_S \geqslant 0 \Longrightarrow J\,(s_V - s_L) + \frac{Q_V}{\theta_V} - \frac{Q_L}{\theta_L} = \sigma_S \geqslant 0, \tag{5.6}$$

where $s(\rho,\theta)$ is the entropy, and from the Gibbs free energy, we have

$$g(\rho,\theta) = h(\rho,\theta) - \theta s(\rho,\theta), \tag{5.7}$$

which is used to rewite the entropy balance as

Table 5.1: The thermodynamic fluxes and their corresponding forces that are found by formulating the entropy production at the interface from writing the NSF equations in their jump form.

| **Force** $(X_B)$ | **Flux** $(J_A)$ | **Description** |
|---|---|---|
| $\frac{g_L}{\theta_L} - \frac{g_V}{\theta_V} + h_V \left(\frac{1}{\theta_V} - \frac{1}{\theta_L}\right)$ | $J$ | Mass flux |
| $\frac{1}{\theta_V} - \frac{1}{\theta_L}$ | $Q_V$ | Heat flux |

$$J\left(\frac{h_V - g_V}{\theta_V} - \frac{h_L - g_L}{\theta_L}\right) + \frac{Q_V}{\theta_V} - \frac{Q_L}{\theta_L} = \sigma_S \geqslant 0. \tag{5.8}$$

In equation (5.8), the liquid heat flux $Q_L$ can be eliminated using the internal energy balance, equation (5.5), which reads

$$J\left[\frac{g_L}{\theta_L} - \frac{g_V}{\theta_V} + h_V\left(\frac{1}{\theta_V} - \frac{1}{\theta_L}\right)\right] + Q_V\left(\frac{1}{\theta_V} - \frac{1}{\theta_L}\right) = \sigma_S \geqslant 0, \tag{5.9}$$

and compared to the equation (5.1), it gives the thermodynamic fluxes and their corresponding forces that are shown in Table 5.1. The forces are deviations from the equilibrium state, e.g., the temperature difference between the two phases in non-equilibrium since the temperature is homogeneous in the equilibrium state. The fluxes are driving the system towards the disturbed equilibrium, e.g., the heat flux $Q_V$ to equilibrate the temperature.

From equation (5.9) and the second law of thermodynamics, forces vanish in equilibrium and then the fluxes vanish, and for the non-equilibrium states, the entropy generation must be positive.

The LIT connects forces and fluxes linearly with the matrix of dimensionless interface resistivities. More detailed descriptions of the LIT can be found in [20, 21]. The LIT formulation reads

$$\begin{bmatrix} \rho_V \sqrt{\frac{\theta_L}{2\pi}} \left[\frac{g_L}{\theta_L} - \frac{g_V}{\theta_V} + h_V\left(\frac{1}{\theta_V} - \frac{1}{\theta_L}\right)\right] \\ \rho_V \sqrt{\frac{\theta_L}{2\pi}} \left[\frac{\theta_L}{\theta_V} - 1\right] \end{bmatrix} = \begin{bmatrix} r_{11} & r_{12} \\ r_{21} & r_{22} \end{bmatrix} \begin{bmatrix} J \\ \frac{Q_V}{\theta_L} \end{bmatrix}, \tag{5.10}$$

where $r_{\alpha\beta}$ are the dimensionless interface resistivities and to guarantee the positive entropy production, the resistivities matrix needs to be positive definite. The LIT assumes that the $r_{\alpha\beta}$ depend only on the local state, i.e., on $\rho$ and $\theta$, not on the fluxes.

The first force in the matrix of forces is non-linear and contains the enthalpy and the Gibbs free energies. This force can be written as a function of the mass densities and the temperatures of the two phases at the interface.

Note that, based on the LIT, each phase is assumed to be in local equilibrium. The enthalpy is $h(\rho,\theta) = u(\rho,\theta) + \frac{p(\rho,\theta)}{\rho}$, where $u$ is the specific internal energy and the system's equilibrium pressure is the van-der-Waals-like pressure $p = \left[\rho\theta\left(1 + \frac{2\pi}{3}\rho Y(\rho)\right) - \frac{2\pi}{3}\chi_1\rho^2\right]$. Also, in equilibrium, the internal energy is the three-halfs of the temperature, plus the Vlasov term as a correction for the real gas effects [25]

$$u(\rho,\theta) = \frac{3}{2}\theta - \frac{2\pi}{3}\chi_1\rho. \tag{5.11}$$

To determine the Gibbs free energy, equation (5.7), it is required to determine the entropy. The entropy can be calculated using the Gibbs equation. We have

$$ds = \frac{1}{\theta}du - \frac{p}{\theta\rho^2}d\rho, \tag{5.12}$$

and substituting the internal energy from equation (5.11), and the van-der-Waals-like pressure from equation (3.13), reads

$$ds = \frac{1}{\theta}\left(\frac{3}{2}d\theta + \frac{2\pi}{3}\chi_1 d\rho\right) - \left(\frac{1}{\rho} + \frac{2\pi}{3}Y(\rho) - \frac{\frac{2\pi}{3}\chi_1}{\theta}\right)d\rho, \tag{5.13}$$

and the integration reads

$$s - s_0 = \frac{3}{2}\ln\left(\frac{\theta}{\theta_0}\right) - \ln\left(\frac{\rho}{\rho_0}\right) - \left[\frac{3 - \frac{\pi}{3}\rho}{\left(1 - \frac{\pi}{6}\rho\right)^2} - \frac{3 - \frac{\pi}{3}\rho_0}{\left(1 - \frac{\pi}{6}\rho_0\right)^2}\right], \tag{5.14}$$

where $s_0$, $\theta_0$, and $\rho_0$ define a reference state. Substituting the defined enthalpy and entropy

when $s_0 = 0$ in equation (5.7), gives the Gibbs free energy

$$g(\rho,\theta) = \theta\left[\frac{5}{2} + \frac{2\pi}{3}\rho Y - \frac{4\pi}{3}\chi_1\frac{\rho}{\theta} - \frac{3}{2}\ln\left(\frac{\theta}{\theta_0}\right) + \ln\left(\frac{\rho}{\rho_0}\right) + \frac{3-\frac{\pi}{3}\rho}{\left(1-\frac{\pi}{6}\rho\right)^2} - \frac{3-\frac{\pi}{3}\rho_0}{\left(1-\frac{\pi}{6}\rho_0\right)^2}\right], \tag{5.15}$$

that shows how the non-ideal contributions of the Enskog and Vlasov terms correct the ideal gas limitations through $Y$ and $\chi_1$, respectively.

Hence, the first thermodynamic force in equation (5.10) can be written as a function of temperature and density, as

$$\rho_V\sqrt{\tfrac{\theta_L}{2\pi}}\left[\tfrac{g_L}{\theta_L} - \tfrac{g_V}{\theta_V} + h_V\left(\tfrac{1}{\theta_V} - \tfrac{1}{\theta_L}\right)\right] =$$

$$\rho_V\sqrt{\tfrac{\theta_L}{2\pi}}\begin{bmatrix} +\left(\frac{5}{2}\right)\left(1-\frac{\theta_V}{\theta_L}\right) - \frac{3}{2}\ln\left(\frac{\theta_L}{\theta_V}\right) + \ln\left(\frac{\rho_L}{\rho_V}\right) \\ +\frac{2\pi}{3}\left(Y_L\rho_L - Y_V\rho_V\frac{\theta_V}{\theta_L}\right) - \frac{4\pi}{3}\chi_1\left(\frac{\rho_L-\rho_V}{\theta_L}\right) \\ +\frac{3-\rho_L\frac{\pi}{3}}{\left(1-\rho_L\frac{\pi}{6}\right)^2} - \frac{3-\rho_V\frac{\pi}{3}}{\left(1-\rho_V\frac{\pi}{6}\right)^2} \end{bmatrix}. \tag{5.16}$$

For the small deviations from the equilibrium, where $\Delta\theta = \theta_V - \theta_L$ and $\Delta p = p - p_{sat}(\theta_L)$ are small, the non-linear forces of (5.10) can be linearized with $\left(\frac{\partial g}{\partial p}\right)_\theta = v$ and $\left(\frac{\partial g}{\partial \theta}\right)_p = -s$ , from the Gibbs equation, to yield

$$\begin{bmatrix} -\left(1-\frac{\rho_g}{\rho_f}\right)\frac{\Delta p}{\sqrt{2\pi\theta_L}} \\ -\frac{\rho_g}{\sqrt{2\pi\theta_L}}\Delta\theta \end{bmatrix} = \begin{bmatrix} r_{11} & r_{12} \\ r_{21} & r_{22} \end{bmatrix}\begin{bmatrix} J \\ \frac{Q_V}{\theta_L} \end{bmatrix}. \tag{5.17}$$

## 5.2 Interface Location

Based on the LIT, the NSF equations are assumed valid for each phase, while the jump and slip conditions are considered at the sharp interface. It is found that for determining the interface resistivities from either (5.10) or (5.17), the values of the thermodynamic forces and fluxes at the interface are needed. Hence, the resolved interface found from the 26-

moment equations is used to find the required interface variables. However, as discussed in Chap. 4, the resolved interface gives the continuous steep changes of the variables at the interface. As a result, to extract the required interface variables for the LIT from the resolved interface, a point needs to be chosen as the interface location.

Frezzotti et al. suggested the point with the maximum absolute value of the mass density gradient as the interface location [34], and this is used in this research, too. However, other locations like the liquid length $L_0$ could be chosen as the sharp interface location.

Choosing a different point could affect the extracted jump and slip conditions, and it might lead to determining different values of the interface resistivities from the LIT.

## 5.3 Extracting the Interface Variables

By choosing the interface location, the 26-moment can be used to extract the variables at the sharp interface. As the LIT has nothing to do with the Knudsen layers, the required interface variables should be determined by extrapolating the results outside of the Knudsen layers. Therefore, the solution of the 26-moment equations in the bulk phases can be used to find the corresponding NSF solution for the extrapolation.

In general, in the forced evaporation/condensation process with two temperature boundaries, according to the first law of thermodynamics, the NSF solutions for the temperature and heat flux in the vapour bulk are curved [7]. However, they can be approximated as linear functions for the relatively small mass fluxes. The linear extrapolations are used to determine the interface variables from the 26-moment solutions of the forced evaporation process instead of extrapolating the NSF solutions.

For larger mass fluxes, the linear extrapolations become inaccurate in determining the interface variables based on 26-moment results for the forced evaporation/condensation process with two temperature boundaries. In these cases, the interface resistivities are determined based on the solution of the 26-moment equations for the adiabatic evapora-

tion/condensation processes. The adiabatic vapour boundary process is helpful because the non-convective heat flux of the vapour vanishes, and temperature is a flat line on the vapour side for any controlled mass fluxes. As a result, the linear extrapolation works even for the large mass fluxes. However, due to the zero vapour heat flux in this process, only two of the interface resistivities can be determined by solving equation (5.10).

The result from the forced evaporation/condensation process with two temperature boundaries can be used to determine the resistivities for large mass fluxes if more accurate extrapolations have been used. The exponential extrapolations or extrapolating the corresponding NSF solution could be helpful.

### 5.3.1 Linear Extrapolations

The matrix of the fluxes in (5.10) and (5.17) are the same. The mass flux $J$ is straightforward because it is an input parameter.

The other required flux is the non-convective heat flux of the vapour phase at the interface $Q_V$. For the small mass fluxes, heat transfer is mainly non-convective, and since the total heat flux is constant, then the non-convective heat flux stays constant in bulk phases, and as shown in Figure 5.2, extrapolation of the heat flux is trivial. Also, for the adiabatic vapour boundary, the non-convective heat flux of the vapour vanishes.

To determine the forces of either (5.10) or (5.17), the temperatures and densities of the two phases at the interface are required, where (5.10) needs the actual mass densities, and (5.17) requires the saturated mass densities for the corresponding temperature of the liquid at the interface. Also, for solving equation (5.17) the pressure deviation from the equilibrium is needed.

Temperatures of the interface are found from linear extrapolation of the 26-moment temperature curve. Figure 5.3a shows the linear extrapolations of the forced evaporation results which are useful for small mass fluxes. Figure 5.3b shows the linear extrapolations of the temperature from the adiabatic process results and are valid for any controlled mass

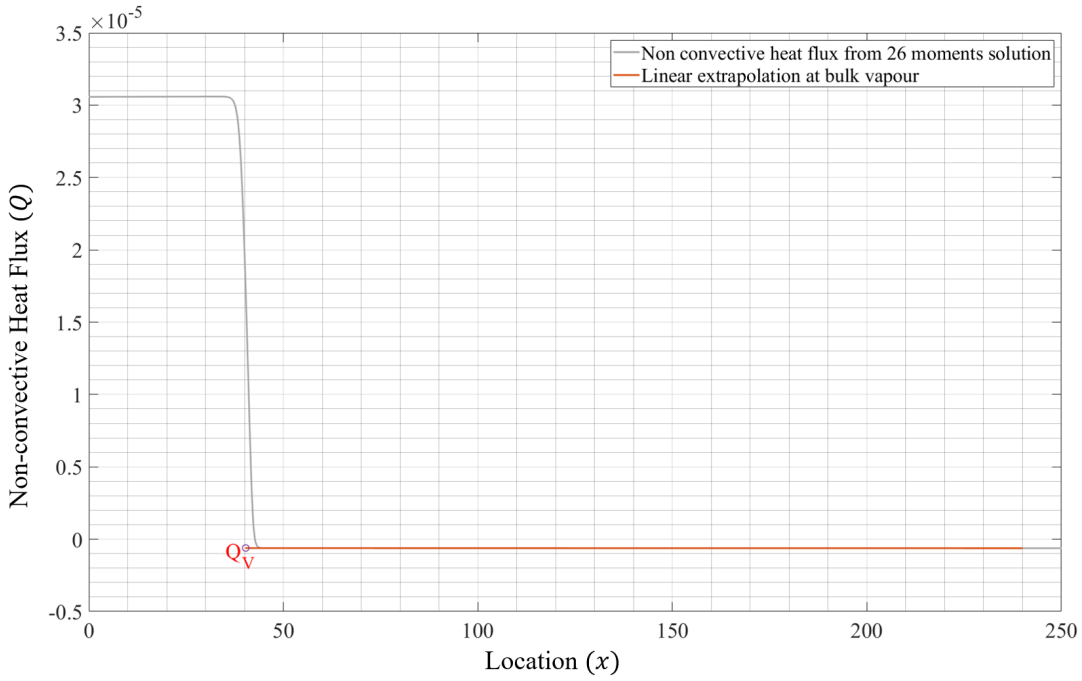


Figure 5.2: The non-convective heat flux curve, which is found by solving 26-moment equations in the evaporation process with two temperature boundaries, when $J = 10^{-5}$, and $\theta_{LW} = \theta_{RW} = 0.55$, together with the linear extrapolation of the non-convective heat flux on the vapour side for extracting the heat flux of the vapour at the interface.

flux. As a result, the liquid temperature $\theta_L$, vapour temperature $\theta_V$, and the corresponding interface temperature jump $\Delta\theta = \theta_V - \theta_L$ can be extracted.

The liquid and vapour densities $\rho_L$ and $\rho_V$ are found by solving the thermal equation of state (3.13) using the system's pressure and each of the two extrapolated interface temperatures. For the linearized forces, the saturated mass densities of the two phases at the liquid temperature are found from the equilibrium solutions. The pressure deviation from the equilibrium state $\Delta p = p - p_{sat}(\theta_L)$ is calculated by subtracting the saturation pressure from the system's pressure.

## 5.4 Interface Resistivities

In order to determine the four interface resistivities from the forced evaporation process, shown in Figure 4.10, solutions of the 26-moment equations for two configurations are

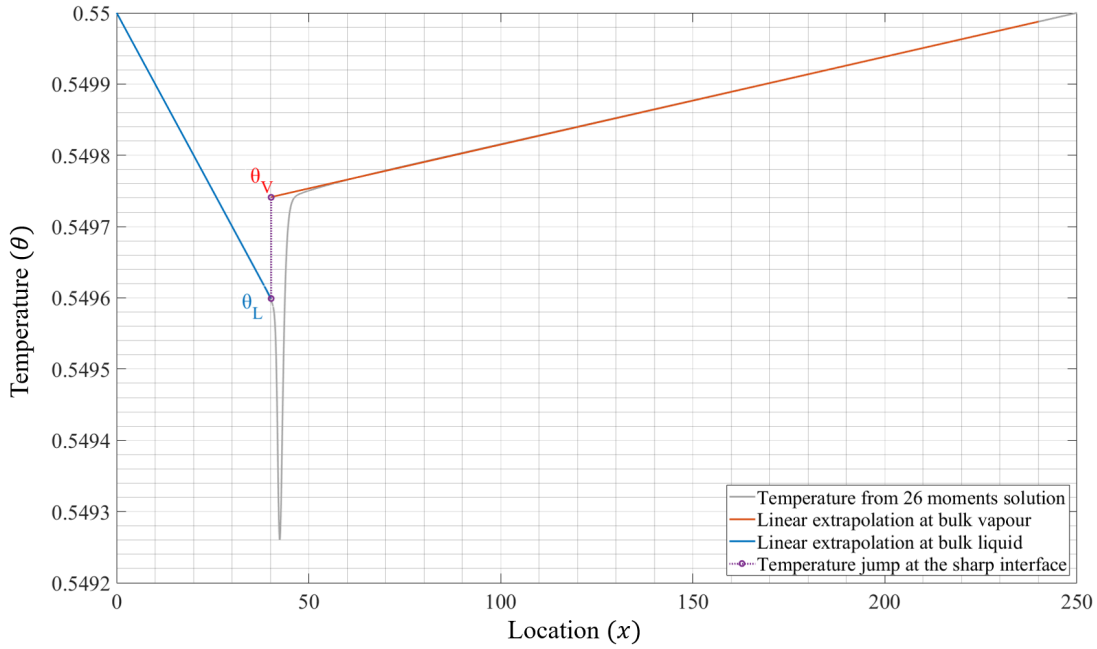


(a)

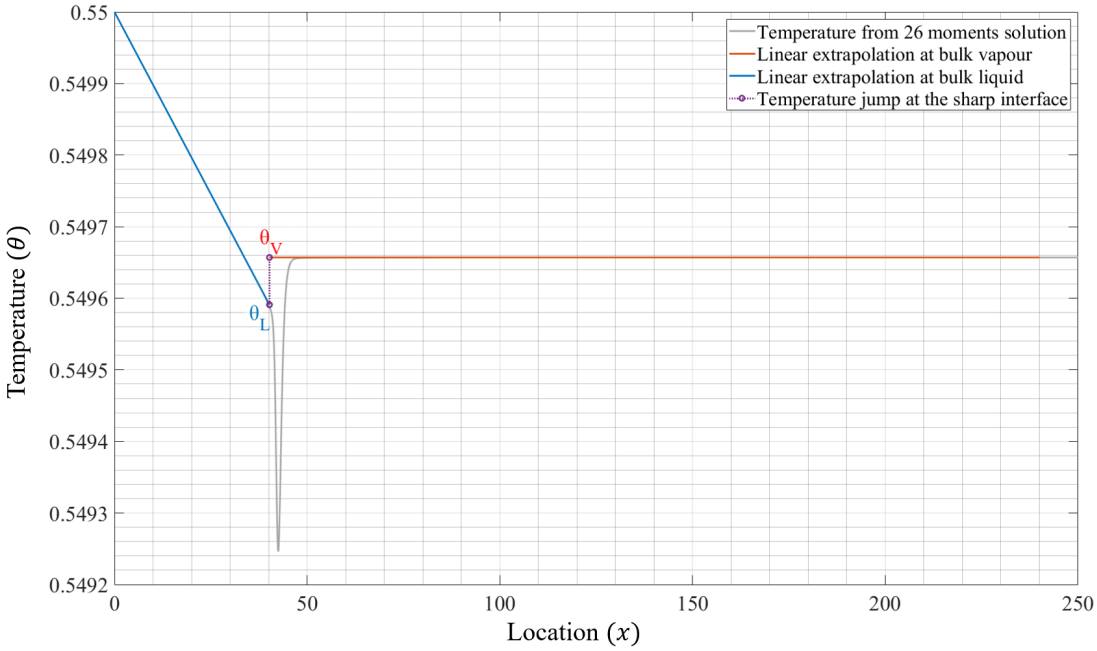


(b)

Figure 5.3: The temperature curve found by solving 26-moment equations together with the linear extrapolations of the temperature on both liquid and vapour sides for extracting the temperature jump at the sharp interface. (a) The linear extrapolated temperatures in the evaporation process with two temperature boundaries, when $J = 10^{-5}$, and $\theta_{LW} = \theta_{RW} = 0.55$. (b) The linear extrapolated temperatures in the evaporation process with the adiabatic vapour boundary, when $J = 10^{-5}$, and $\theta_{LW} = 0.55$.

required. The two processes $A$ and $B$ with similar properties, except the slightly different vapour boundary temperatures, are solved to determine a set of interface resistivities from either equation (5.10) or equation (5.17). The system of equations can be written as

$$\begin{aligned}
(X_1)_A &= r_{11}J + r_{12}\left(\tfrac{Q_V}{\theta_L}\right)_A \\
(X_2)_A &= r_{21}J + r_{22}\left(\tfrac{Q_V}{\theta_L}\right)_A \\
(X_1)_B &= r_{11}J + r_{12}\left(\tfrac{Q_V}{\theta_L}\right)_B \\
(X_2)_B &= r_{21}J + r_{22}\left(\tfrac{Q_V}{\theta_L}\right)_B,
\end{aligned} \tag{5.18}$$

where $X_1$ and $X_2$ are the two thermodynamics forces, either linearized or non-linear. In configuration $A$, the vapour boundary temperature is $(\theta_{RW})_A = \theta_{LW} + \left(10^{-5}\right)$, and the vapour boundary temperature in configuration $B$ is $(\theta_{RW})_B = \theta_{LW} + \left(2 \times 10^{-5}\right)$. The slight boundary temperature difference in the two configurations leads to almost the same liquid temperature at the interface.

All four interface resistivities are found for the relatively small mass fluxes at different liquid temperatures of the interface by solving the equation (5.18).

Figure 5.4 shows the EV interface resistivities for $J = 10^{-6}$, based on both linearized and non-linear thermodynamic forces. Due to the relatively small strength of the non-equilibrium processes, it is seen that the results from the linearized and non-linear forces are almost the same. It is found clearly that the resistivities are functions of the liquid temperature at the interface.

At the lower temperatures, liquid and vapour mass densities are more different than the larger temperatures, which appears to increase the diagonal resistivities. The larger mean free path at the low temperatures leads to wider Knudsen layers; each of the four resistivities has a greater magnitude than those at the higher temperatures.

Figure 5.4 shows a sign-change in the off-diagonal resistivities $r_{12}$ and $r_{21}$ at the relatively large temperature of $\theta_L > 0.6$, which defined the possible change in temperature jump direction at the phase interface.

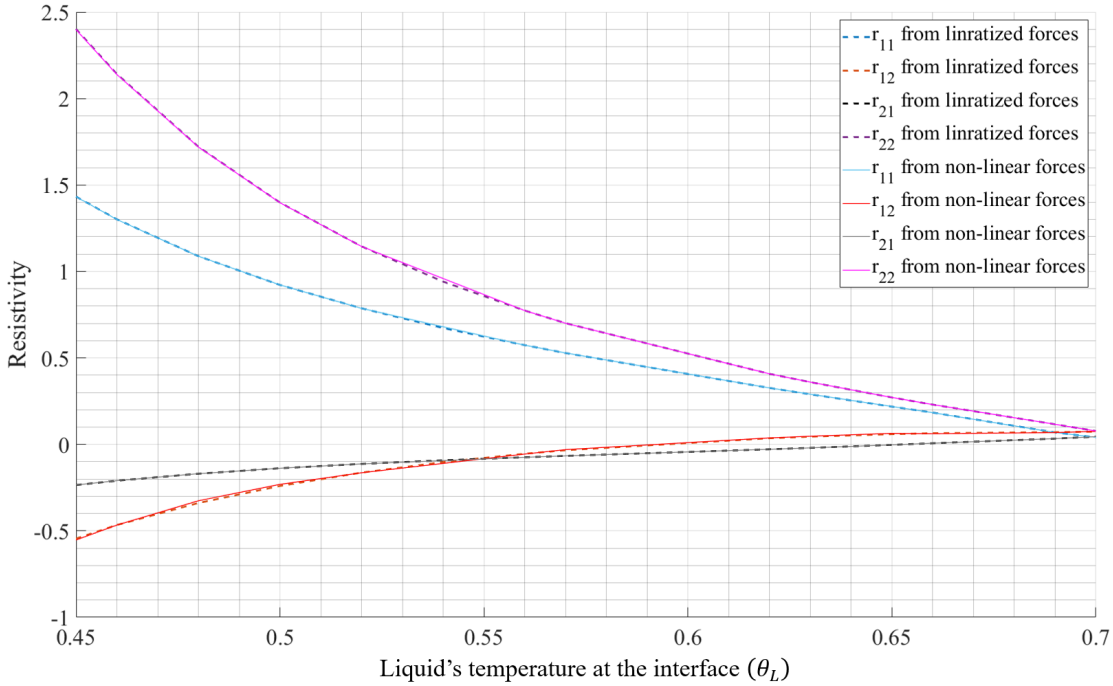


Figure 5.4: The four EV interface resistivities from the LIT with either the linearized or the non-linear thermodynamic forces based on the solutions of the 26-moment equations in the evaporation process with two temperature boundaries at different temperatures of the liquid at the interface and constant mass flux of $J = 10^{-6}$.

After determining the resistivities for the slight deviations from the equilibrium and showing their dependence on the interface temperature, to study the mass flux effects on resistivities, the mass flux is increased. The interface resistivities are determined and visualized in Figure 5.5 when the controlled mass flux is increased to $J = 10^{-5}$.

It can be seen that the resistivities from the linearized and the non-linear forces are still similar to each other. However, compared to the determined EV resistivities for $J = 10^{-6}$, shown in Figure 5.4, there are more deviations here for $J = 10^{-5}$, in particular at lower temperatures.

Comparing Figures 5.4 and 5.5 shows similar changes in magnitudes of all the resistivities by increasing the liquid temperature, especially at lower temperatures.

The negative values of $r_{22}$ at large temperatures $\theta_L > 0.66$ imply violating the positive definiteness of the resistivity matrix. This might happened due to the linear extrapolations inaccuracy in determining the interface variables for larger fluxes. To prevent the calculations errors due to the linear extrapolations, for larger mass fluxes, the resistivities are not determined from the forced evaporation/condensation results with the two temperature boundaries.

To visualize the changes of the resistivities with the mass fluxes, Figure 5.6 shows each of them according to the liquid's temperatures at the interface up to $\theta_L = 0.65$ for the two different mass fluxes based on non-linear forces. In Figure 5.6, the axes lengths for all the resistivities are the same for a better comparison.

It can be seen in Figure 5.6 that the changes of the diagonal resistivities with the mass flux are more considerable than the changes for the off-diagonal resistivities. At the same time, changes of $r_{11}$ and $r_{21}$ with mass flux are more significant at lower temperatures, while in relatively large temperatures, the EV resistivities show similar values.

Finding that the resistivities are changing with the mass flux means that the realm of LIT has been left at the interface since no dependence on the fluxes was assumed in the LIT formulation. However, it might happen due to the breakdown of the linear extrapola-

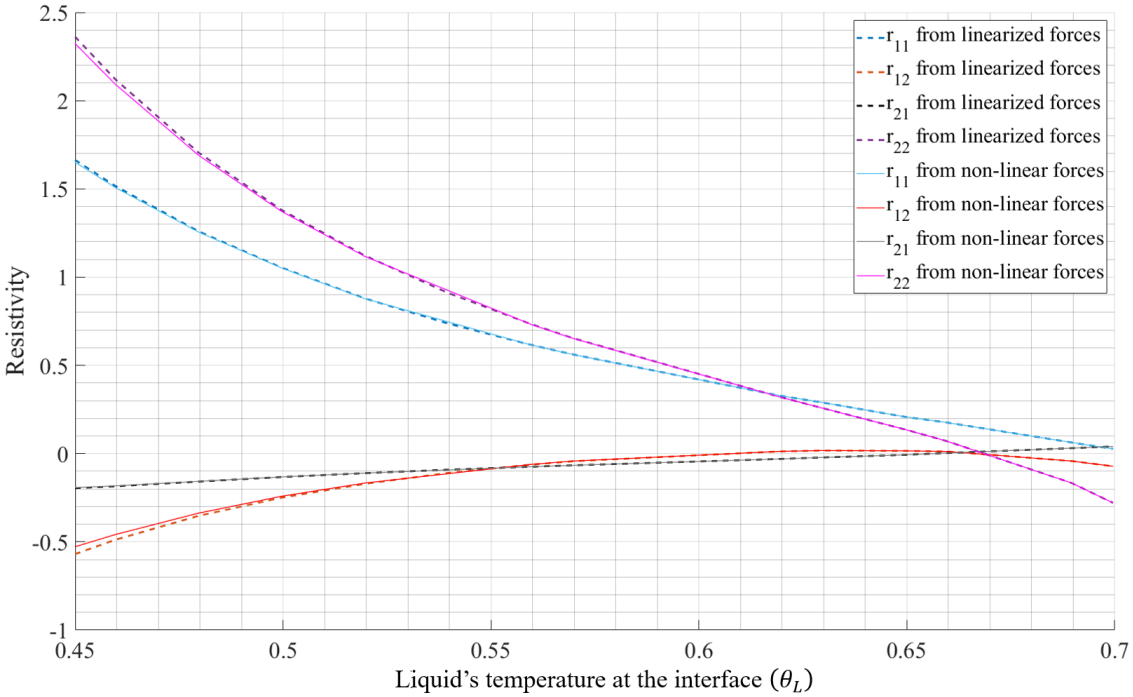


Figure 5.5: The four EV interface resistivities from the LIT with either linearized or the non-linear thermodynamic forces based on the solutions of the 26-moment equations in the evaporation process with two temperature boundaries at different temperatures of the liquid at the interface and the constant mass flux of $J = 10^{-5}$.

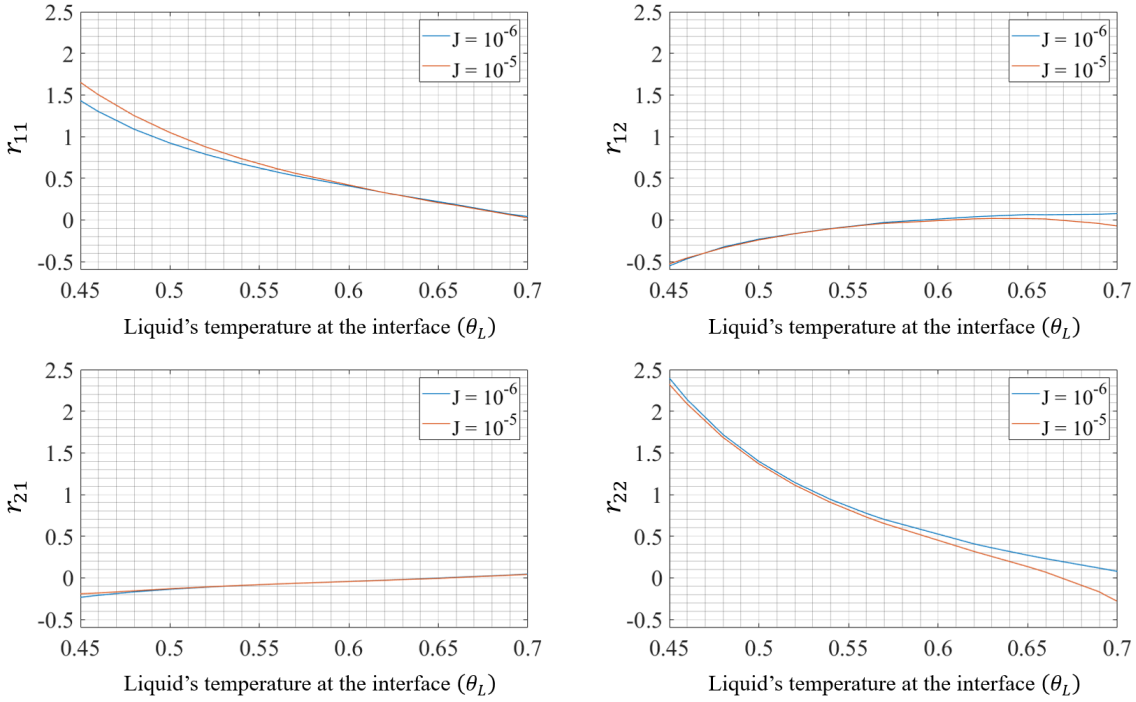


Figure 5.6: The four EV interface resistivities from the LIT with non-linear thermodynamic forces based on the solutions of the 26-moment equations in the evaporation process with two temperature boundaries at different temperatures of the liquid at the interface and two different mass fluxes of $J = 10^{-6}, 10^{-5}$.

tion, and more results should be found to evaluate the possible dependence of the interface resistivities on the non-equilibrium strength.

To have a more explicit overview of the interface resistivities, they are tabulated in Table 5.2 based on the non-linear forces. The table shows the interface resistivities for the different mass fluxes and the liquid temperatures of the interface.

The symmetricity of the off-diagonal resistivities that is found by Onsager [64, 65] is also interesting to be studied. Figure 5.6 shows that the off-diagonal resistivities are not fully symmetric, especially at lower temperatures. Table 5.2 shows that for the temperatures between $0.53 \leq \theta \leq 0.55$, the off-diagonal resistivities are approximately symmetric, while symmetric results are not found at the lower and higher temperatures. However, the results can be considered roughly symmetric for a wider range of the temperatures, particularly at the middle temperatures, relative to the magnitude of the diagonal resistivities.

One possible reason for not having the fully symmetric off-diagonal resistivities might be the inappropriate selection of the interface location, which is considered as the point with the largest mass density gradient. Hence, one could consider choosing the location of the sharp interface such that the off-diagonal are symmetric.

Comparing the determined EV resistivities in Table 5.2 with the suggested constant resistivities from the classical kinetic theory, shown in equation (1.2), indicates significant differences in both magnitude and sign.

In equation (1.2) that is found based on the ideal gas assumptions, which is valid at temperatures well below the critical temperature, considering the unity condensation probability gives $r_{11}$ and $r_{22}$ equal to 0.59956 and 0.294, respectively. While at the low temperatures, the EV diagonal resistivities are larger than these kinetic theory interface resistivities.

In contrast, at the large temperatures, it can be seen in Table 5.2 that the EV diagonal resistivities are both smaller than 0.59956 and 0.294, respectively.

It is interesting to compare the determined EV off-diagonal resistivities with the constant and identical value of 0.126, suggested by the classical kinetic theories in equation

Table 5.2: The four interface resistivities are tabulated based on the temperature of the liquid at the interface for two different mass fluxes of $J = 10^{-6}, 10^{-5}$.

| | $J = 10^{-6}$ | | | | $J = 10^{-5}$ | | | |
|---|---|---|---|---|---|---|---|---|
| $\theta_L$ | $r_{11}$ | $r_{12}$ | $r_{21}$ | $r_{22}$ | $r_{11}$ | $r_{12}$ | $r_{21}$ | $r_{22}$ |
| 0.45 | 1.43037095 | -0.549554757 | -0.233689159 | 2.39086698 | 1.648971239 | -0.525431416 | -0.192218612 | 2.31971792 |
| 0.46 | 1.298755063 | -0.464629425 | -0.209198009 | 2.13575083 | 1.501003872 | -0.454792588 | -0.182297428 | 2.091814159 |
| 0.47 | 1.191764083 | -0.394387445 | -0.188958794 | 1.923154038 | 1.377527655 | -0.394471792 | -0.169541621 | 1.884955752 |
| 0.48 | 1.086471373 | -0.324145465 | -0.169229812 | 1.716226493 | 1.24996958 | -0.335341538 | -0.156785813 | 1.685840708 |
| 0.49 | 1.004954437 | -0.277714325 | -0.153582688 | 1.554652931 | 1.150984513 | -0.287719856 | -0.144313468 | 1.526548673 |
| 0.50 | 0.92173923 | -0.230092644 | -0.137595409 | 1.393079369 | 1.045876659 | -0.240098175 | -0.131841123 | 1.371681416 |
| 0.51 | 0.85380845 | -0.196757467 | -0.125349834 | 1.268355918 | 0.960157633 | -0.20200083 | -0.12078609 | 1.238938053 |
| 0.52 | 0.785877669 | -0.16342229 | -0.112764104 | 1.140797843 | 0.874438606 | -0.165490874 | -0.101227185 | 1.110619469 |
| 0.53 | 0.733231314 | -0.13643667 | -0.103239768 | 1.050089878 | 0.809128872 | -0.139298949 | -0.092156388 | 1.017699115 |
| 0.54 | 0.67888669 | -0.109451051 | -0.093362832 | 0.95654729 | 0.743819137 | -0.113107024 | -0.083085592 | 0.924778761 |
| 0.55 | 0.626240335 | -0.082465431 | -0.083628319 | 0.867256637 | 0.679529867 | -0.0869151 | -0.074014795 | 0.82300885 |
| 0.56 | 0.57359398 | -0.002302268 | -0.074326604 | 0.769462113 | 0.613199668 | -0.05992948 | -0.066077848 | 0.730088496 |
| 0.57 | 0.529438973 | -0.054867257 | -0.06599281 | 0.698596515 | 0.55809458 | -0.041674502 | -0.058991289 | 0.650442478 |
| 0.58 | 0.488680504 | -0.030088496 | -0.05867948 | 0.639069414 | 0.511153208 | -0.031356471 | -0.051621267 | 0.588495575 |
| 0.59 | 0.447922036 | -0.015634218 | -0.051196073 | 0.579542312 | 0.46727323 | -0.020244746 | -0.044534707 | 0.517699115 |
| 0.60 | 0.407163568 | 0.01120944 | -0.043372511 | 0.522849834 | 0.417270465 | -0.00913302 | -0.037164685 | 0.451327434 |
| 0.61 | 0.366405099 | 0.024631268 | -0.035889104 | 0.463322732 | 0.373390487 | 0.001978706 | -0.021432522 | 0.384955752 |
| 0.62 | 0.32916053 | 0.038053097 | -0.028065542 | 0.403795631 | 0.326449115 | 0.013090431 | -0.014204231 | 0.318584071 |
| 0.63 | 0.289982971 | 0.047345133 | -0.02024198 | 0.358441648 | 0.286650996 | 0.017058905 | 0.003370437 | 0.256637168 |
| 0.64 | 0.254319311 | 0.056637168 | -0.011397954 | 0.313087666 | 0.245832412 | 0.01626521 | 0.012724696 | 0.194690265 |
| 0.65 | 0.218655652 | 0.063864307 | -0.002894082 | 0.267733684 | 0.205013827 | 0.015471515 | 0.022078955 | 0.132743363 |
| 0.66 | 0.184690261 | 0.062831858 | 0.006630254 | 0.228048949 | 0.175420354 | 0.011503042 | 0.031149751 | 0.066371681 |
| 0.67 | 0.145630063 | 0.063864307 | 0.015474281 | 0.188364215 | 0.135622235 | -0.006751936 | -0.11039823 | -0.013274336 |
| 0.68 | 0.108268133 | 0.066961652 | 0.024318308 | 0.151514104 | 0.099905973 | -0.025006914 | -0.030014749 | -0.088495575 |
| 0.69 | 0.069207934 | 0.069026549 | 0.033502489 | 0.114663993 | 0.060107854 | -0.043261892 | -0.006415929 | -0.172566372 |

(1.2). The magnitude of the determined off-diagonal resistivities at low temperatures are greater than 0.126 and smaller at relatively large temperatures. The other considerable difference is in their signs. For temperatures less than 0.6, Table 5.2 shows negative values for $r_{12}$ and $r_{21}$, while classical kinetic studies suggested the positive values for them. This change in the signs leads to a different temperature jump direction at the phase interface.

The effect of the off-diagonal resistivities' sign on the direction of the temperature jump can be seen clearly from equation (5.17) that reads

$$\Delta\theta = \frac{\sqrt{2\pi\theta_L}}{\rho_g}\left(-r_{21}J - r_{22}\frac{Q_V}{\theta_L}\right), \tag{5.19}$$

where $\frac{\sqrt{2\pi\theta_L}}{\rho_g}$ is positive; $J > 0$ and $Q_V < 0$ in the evaporation process. As a result, for $r_{22} > 0$, the negative off-diagonal resistiviy $r_{21} < 0$ gives the positive temperature jump $\Delta\theta = \theta_V - \theta_L > 0$, while the positive off-diagonal resistiviy $r_{21} > 0$ might give the negative temperature jump $\Delta\theta = \theta_V - \theta_L < 0$. In adiabatic evaporation, where $Q_V = 0$, the change in temperature jump direction with the sign of $r_{21}$ is even more evident from equation (5.19).

The determined negative signs for the off-diagonal resistivities at low temperatures with relatively small mass flux will predict the temperature jump's correct direction as it was observed in Ward et al. experiment [11].

These results show that determining the interface resistivities from the 26-moment equations is a promising alternative way to make the theoretical predictions of the interface mechanisms in agreement with the experimental results in principle.

The presented EV resistivities show that they are functions of the interface temperatures. It is seen that changing the mass flux also affects the values of the resistivities. However, due to the limitations in using the linear extrapolations, the resistivities are found for two small mass fluxes based on the results from the evaporation process with two temperature boundaries.

More results are found here from the adiabatic process, which helps to study the resis-

tivity changes with the mass flux that is the question of linearity of the interface conditions. Due to the zero non-convective vapour heat flux, either equation (5.10) or equation (5.17) simplifies to

$$\begin{aligned} r_{11} &= \frac{X_1}{J} \\ r_{21} &= \frac{X_2}{J}, \end{aligned} \tag{5.20}$$

which shows that only the resistivities $r_{11}$ and $r_{21}$ can be determined from this process, and one adiabatic process suffices.

Figure 5.7 shows the EV resistivities and compares them based on the linearized and non-linear forces for the three relatively large controlled mass fluxes.

It can be seen in Figure 5.7 that increasing the non-equilibrium strength by prescribing larger mass fluxes leads to more significant deviations between the results found from the non-linear and linearized forces. As a result, it is appropriate to consider the results from the non-linear forces.

Figure 5.7 shows that the resistivities change with increasing mass flux. These results are in agreement with the resistivities found from the forced evaporation process with two temperature boundaries for the smaller mass fluxes, see Figure 5.6.

To have better comparison and see the effects of the mass flux clearly, Figure 5.8, shows the two EV resistivities for the six different mass fluxes based on the non-linear forces. The two EV resistivities from the adiabatic process are tabulated in Tables 5.3 and 5.4 for different temperatures of the liquid at the interface and mass fluxes.

Tables show the positive values of the $r_{11}$ at any temperatures and mass fluxes, in agreement with the positive definiteness of the resistivity matrix. Values of $r_{21}$ are mostly negative that means in the evaporation process, the temperature of the liquid is less than the vapour temperature; however, it becomes positive at some temperatures or mass fluxes which implies that the jump direction might change depending on the process.

The temperature curves for the two controlled mass fluxes and the same controlled

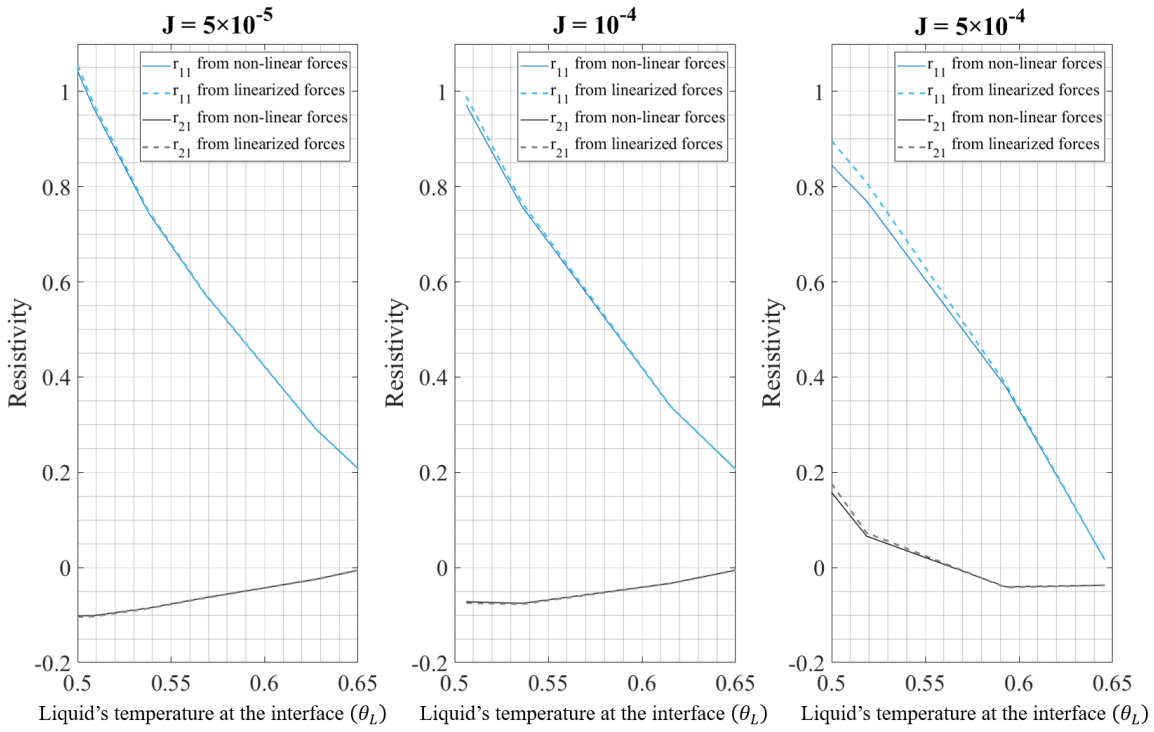


Figure 5.7: The two EV interface resistivities from the LIT with the linearized and the non-linear thermodynamic forces based on the solutions of the 26-moment equations in the evaporation process with the adiabatic vapour boundary at different temperatures of the liquid at the interface and three different mass fluxes of $J = 10^{-5}, 10^{-4}, 5 \times 10^{-4}$.

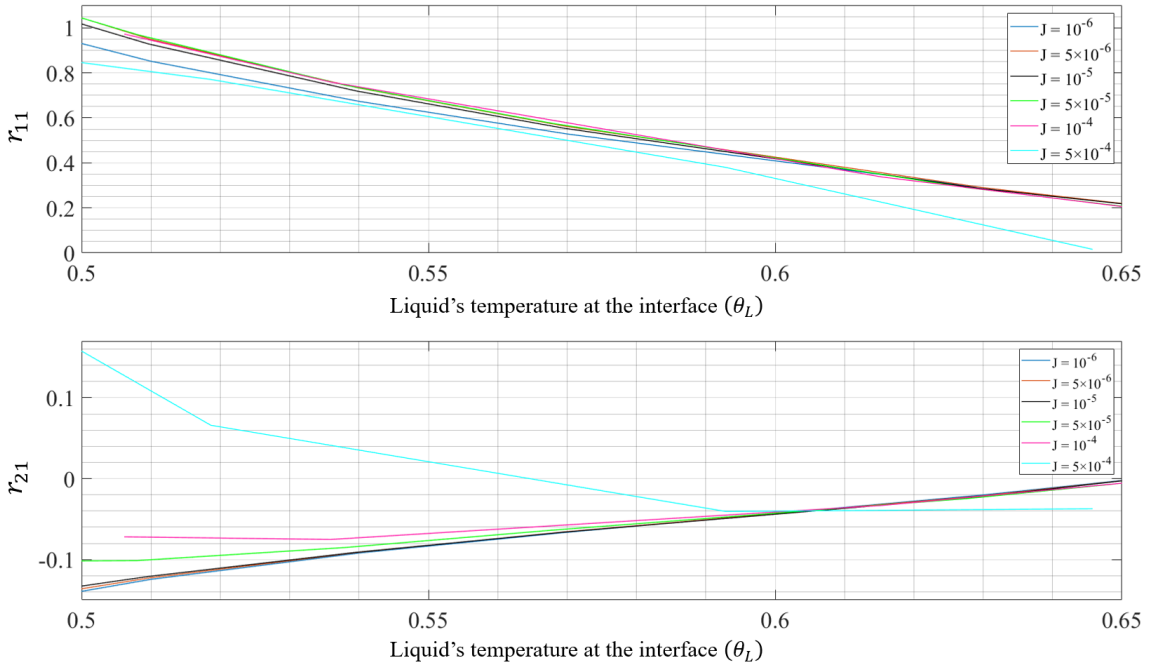


Figure 5.8: The two interface resistivities from the LIT with the non-linear thermodynamic forces based on the solutions of the 26-moment equations in the evaporation process with the adiabatic vapour boundary at different temperatures of the liquid at the interface and six different mass fluxes of $J = 10^{-6}, 5\times10^{-6}, 10^{-5}, 5\times10^{-5}, 10^{-4}, 5\times10^{-4}$.

temperature of the liquid boundary are shown in Figure 5.9. The liquid temperatures at the interface are approximately 0.545 and 0.525 for $J = 10^{-4}$ and $J = 5\times10^{-4}$, respectively. Finding the off-diagonal values for each temperature and mass flux from Table 5.4, gives a negative value for $(J = 10^{-4}, \theta_L = 0.545)$, and a positive value for $(J = 5\times10^{-4}, \theta_L = 0.525)$ that shows why the different jump direction shown in Figure 5.9. This change in temperature jump direction by prescribing the relatively large mass fluxes also is found in the DSMC simulations; see Figure 4.17. Both the temperature of the liquid at the interface and the non-equilibrium strength might change the temperature jump direction.

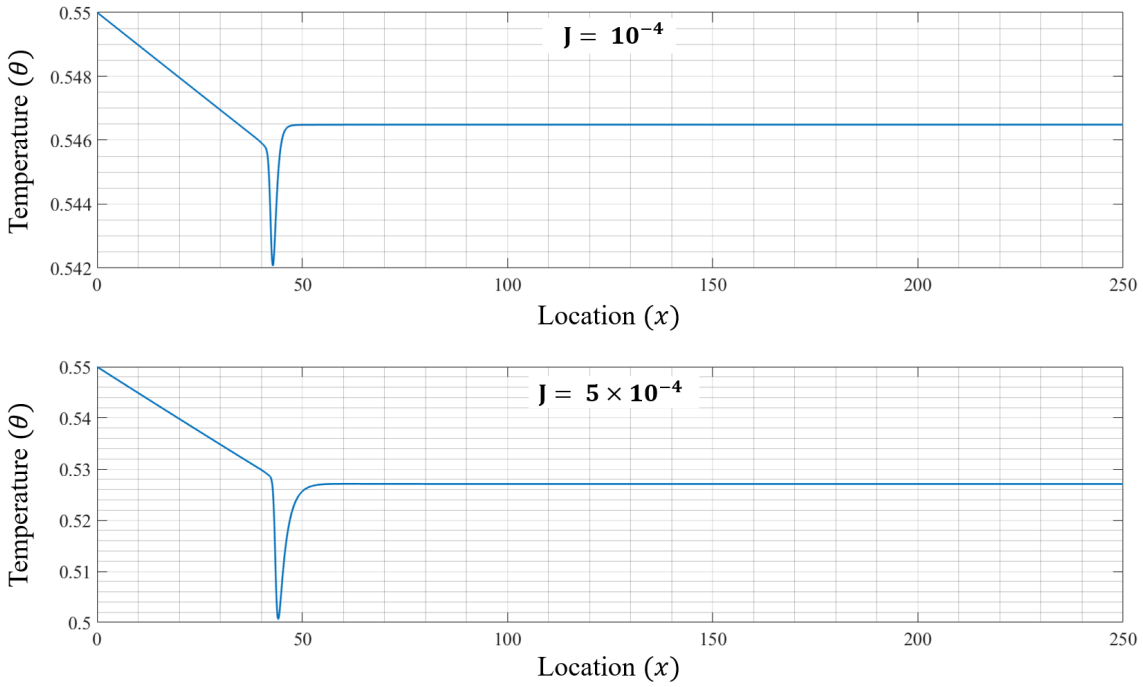


Figure 5.9: The change in the temperature jump direction at the interface found in the temperature curves from the 26-moment equations in the evaporation process with the adiabatic vapour boundary at $\theta_{LW} = 0.55$ for two different mass fluxes of $J = 10^{-4}, 5 \times 10^{-4}$.

The interface resistivities depend on the temperature of the liquid at the interface. Determining the non-constant resistivities for the different non-equilibrium strengths shows that the non-equilibrium strength might also matter, see Figure 5.8. While based on the LIT, which connects the thermodynamic forces and fluxes linearly, the mass fluxes should not affect the interface resistivities, and either the LIT or the transport equations need to be revised.

Table 5.3: The two interface resistivities are tabulated based on the temperatures of the liquid at the interface for three different mass fluxes of $J = 10^{-6}, 5\times10^{-6}, 10^{-5}$.

| | $J = 10^{-6}$ | | $J = 5\times10^{-6}$ | | $J = 10^{-5}$ | |
|---|---|---|---|---|---|---|
| $\theta_L$ | $r_{11}$ | $r_{21}$ | $r_{11}$ | $r_{21}$ | $r_{11}$ | $r_{21}$ |
| 0.45 | 1.429417865 | -0.234199392 | 1.63366427 | -0.216001106 | 1.575544919 | - |
| 0.46 | 1.317166759 | -0.21242948 | 1.501003872 | -0.198823285 | 1.450552283 | -0.174076775 |
| 0.47 | 1.201514104 | -0.190659569 | 1.364261615 | -0.181135232 | 1.324653903 | -0.165856375 |
| 0.48 | 1.087562223 | -0.169229812 | 1.233642146 | -0.163787334 | 1.201472754 | -0.157635974 |
| 0.49 | 1.009326604 | -0.154262998 | 1.137718473 | -0.149670907 | 1.108181149 | -0.145163643 |
| 0.50 | 0.92939021 | -0.139296184 | 1.041794801 | -0.13623479 | 1.015795287 | -0.132974773 |
| 0.51 | 0.853705752 | -0.124669524 | 0.947912058 | -0.122123894 | 0.925220913 | -0.120502442 |
| 0.52 | 0.791627489 | -0.113784569 | 0.874438606 | -0.112083794 | 0.857290133 | -0.110581269 |
| 0.53 | 0.732100387 | -0.102899613 | 0.803006084 | -0.101368916 | 0.785736377 | -0.100660096 |
| 0.54 | 0.672573285 | -0.092014657 | 0.729532633 | -0.090824115 | 0.716899853 | -0.090738923 |
| 0.55 | 0.624951604 | -0.083510785 | 0.674336283 | -0.082320243 | 0.663460972 | -0.082374631 |
| 0.56 | 0.575629148 | -0.075006914 | 0.615240597 | -0.073986449 | 0.606399116 | -0.07401466 |
| 0.57 | 0.528007467 | -0.066503042 | 0.560135509 | -0.0653125 | 0.552054492 | -0.06579426 |
| 0.58 | 0.488889657 | -0.05867948 | 0.513194137 | -0.057829093 | 0.506767305 | -0.058775811 |
| 0.59 | 0.448141438 | -0.051196073 | 0.468293695 | -0.049835454 | 0.464197349 | -0.051337694 |
| 0.60 | 0.408953263 | -0.043362832 | 0.423393252 | -0.043372511 | 0.418004418 | -0.04396768 |
| 0.61 | 0.369835454 | -0.035548949 | 0.37849281 | -0.035840708 | 0.375434462 | -0.036597666 |
| 0.62 | 0.329016869 | -0.027725387 | 0.333592367 | -0.028235619 | 0.329241532 | -0.029511114 |
| 0.63 | 0.28989906 | -0.02024198 | 0.288691925 | -0.020752212 | 0.286671576 | -0.021902655 |
| 0.64 | 0.254182799 | -0.011057799 | 0.251955199 | -0.011568031 | 0.25134757 | -0.012219927 |
| 0.65 | 0.218466538 | -0.002213772 | 0.217259403 | -0.00238385 | 0.218740795 | -0.002582216 |
| 0.66 | 0.186151825 | 0.006630254 | 0.182563606 | 0.006630254 | 0.187039764 | 0.007338957 |
| 0.67 | 0.152136338 | 0.017699115 | 0.145826881 | 0.017004978 | 0.152621502 | 0.017827054 |
| 0.68 | 0.118120852 | 0.027719856 | 0.109090155 | 0.026869469 | 0.117297496 | 0.028598613 |

Table 5.4: The two interface resistivities are tabulated based on the temperatures of the liquid at the interface for three different mass fluxes of $J = 5 \times 10^{-5}, 10^{-4}, 5 \times 10^{-4}$

| | $J = 5 \times 10^{-5}$ | | $J = 10^{-4}$ | | $J = 5 \times 10^{-4}$ | |
|---|---|---|---|---|---|---|
| $\theta_L$ | $r_{11}$ | $r_{21}$ | $r_{11}$ | $r_{21}$ | $r_{11}$ | $r_{21}$ |
| 0.45 | - | - | - | - | - | - |
| 0.46 | - | - | - | - | - | - |
| 0.47 | 1.331742257 | -0.077920354 | - | - | - | - |
| 0.48 | 1.233324115 | -0.091617257 | - | - | - | - |
| 0.49 | 1.133628319 | -0.102502212 | - | - | - | - |
| 0.50 | 1.042837389 | -0.101828909 | - | - | - | - |
| 0.51 | 0.955530973 | -0.100325221 | 0.946006637 | -0.07243031 | 0.844095686 | 0.156488523 |
| 0.52 | 0.879336283 | -0.094882743 | 0.872193031 | -0.073518805 | 0.804410951 | 0.107591261 |
| 0.53 | 0.804728982 | -0.089621681 | 0.803141593 | -0.074607301 | 0.763025442 | 0.064675516 |
| 0.54 | 0.73329646 | -0.083816372 | 0.738058628 | -0.073065265 | 0.710868363 | 0.049056278 |
| 0.55 | 0.673769358 | -0.076559735 | 0.685674779 | -0.067804204 | 0.657577434 | 0.034883158 |
| 0.56 | 0.61821073 | -0.069303097 | 0.630909845 | -0.062452434 | 0.605420354 | 0.020426576 |
| 0.57 | 0.566620575 | -0.062409292 | 0.57931969 | -0.057191372 | 0.553263274 | 0.006253457 |
| 0.58 | 0.517411504 | -0.055811209 | 0.526935841 | -0.051839602 | 0.49940542 | -0.008203125 |
| 0.59 | 0.467408739 | -0.049347345 | 0.472964602 | -0.046533186 | 0.447248341 | -0.022345133 |
| 0.60 | 0.422168142 | -0.042831858 | 0.420580752 | -0.041181416 | 0.393957412 | -0.036725664 |
| 0.61 | 0.372165376 | -0.036285398 | 0.366609513 | -0.036056416 | 0.330461836 | -0.040044248 |
| 0.62 | 0.326924779 | -0.029852507 | 0.319781527 | -0.029298673 | 0.261863938 | -0.03966745 |
| 0.63 | 0.280096792 | -0.022679204 | 0.281684181 | -0.02140708 | 0.193832965 | -0.039100525 |
| 0.64 | 0.244380531 | -0.014152655 | 0.243586836 | -0.013470133 | 0.124668142 | -0.038533601 |
| 0.65 | 0.207870575 | -0.005535398 | 0.205489491 | -0.005533186 | 0.054936394 | -0.037831858 |
| 0.66 | 0.172948009 | 0.003716814 | - | - | - | - |
| 0.67 | 0.142787611 | 0.015599558 | - | - | - | - |
| 0.68 | 0.112627212 | 0.027573009 | - | - | - | - |

# Chapter 6

# Conclusion

## 6.1 Summary

The interface resistivities are required to model the jump and slip conditions at the interface using the sharp interface method. This research aimed to give a full picture of the resistivities that predict the jump and slip conditions at the phase interface in the non-equilibrium evaporation/condensation process to find a better agreement with the experimental results. For this, resolving the interface in high resolutions that visualizes the changes of the variables from one phase to another across the interface is required.

Here, to find the required resolved interface in the evaporation/condensation process, the 26-moment set of macroscopic equations is solved numerically. Compared to the microscopic methods such as the MD or the DSMC, the 26-moment set of equations is solved faster and cheaper for different processes and system configurations.

The resolved interface visualized the phase interface in high resolutions that gave the continuous changes of variables at the interface and the Knudsen layers in front of the interface.

Although the previous theoretical studies based on classical kinetic theory could not predict the temperature jump observed in the experiments neither in magnitude nor the

direction, the solution of the 26-moment equations, which considered a model, showed promising results in describing the system's behaviour in principle. However, the solutions were not found for an actual substance.

The resolved temperature found from the 26-moment equations predicts the temperature jump direction correctly as observed in experiments; also, the magnitude of the predicted temperature jump was considerably greater than the previous studies and in a better agreement with the experiments.

The variations of the variables at and in front of the interface occurred in a thickness of a few particle diameters, making them like jumps. Hence, for the LIT and based on the moment equations results, the interface resistivities are determined and tabulated based on the temperature of the liquid at the interface for different controlled mass fluxes.

Determining the wide range of EV resistivities based on the properties of the system developed the understanding about them and showed they changed by the temperature of the interface and maybe the strength of the process. However, the studies based on classical kinetic theory determined only a set of interface resistivities, and it was assumed that it is constant.

In this research, all four resistivities are determined based on the forced evaporation processes with two temperature boundaries for small mass fluxes.

The EV resistivities at the small controlled mass flux of $J = 10^{-6}$ are considered as a benchmark.

It is found from the 26-moment results that at the lower temperatures, due to the lower pressure and greater difference between the liquid and vapour densities at the interface, the interface is wider, affecting the interface behaviour. As a result, the EV resistivities change with temperature.

The kinetic theory resistivities suggests $r_{11} = 0.59956$, while the EV resistivities at $\theta_L = 0.45$ and $\theta_L = 0.69$ with controlled mass flux of $J = 10^{-6}$, are $r_{11} \simeq 1.43$ and $r_{11} \simeq 0.118$, respectively.

According to the kinetic theory resistivities, $r_{22}$ is 0.294 , while the EV resistivities at $\theta_L = 0.45$ and $\theta_L = 0.69$ for $J = 10^{-6}$ are 2.39 and 0.114, respectively.

The symmetric off-diagonal resistivities of the kinetic theory resistivities are $r_{12} = r_{21} = 0.126$. While the EV resistivities are not fully symmetric, and it might be due to the inappropriate choice of the interface locations. At $\theta_L = 0.55$, the determined values of $r_{12}$ and $r_{21}$ are $-0.08247$ and $-0.08363$, respectively, and they are almost symmetric. At the other temperatures, the determined values of the off-diagonal resistivities have greater differences. However, relative to the magnitude of the diagonal resistivities, the symmetricity of the off-diagonal resistivities can be assumed for a wider range of temperatures.

At $\theta_L = 0.45$, $r_{12} = -0.54955$ and $r_{21} = -0.23369$, where their magnitudes are greater than the kinetic theory resistivities, respectively. The difference between the signs of the off-diagonal resistivities shows the possibility of having different temperature jump directions. Also, at $\theta_L = 0.69$, $r_{12} = 0.06903$ and $r_{21} = 0.03350$, and they are smaller than the corresponding kinetic theory resistivities.

The effects of the non-equilibrium strength on the resistivities are studied by changing the mass flux from $J = 10^{-6}$ to $J = 5 \times 10^{-4}$. For this, the solution of the adiabatic process is used to ensure that no calculation errors occurred due to the linear extrapolations. However, since in adiabatic process $Q_V = 0$, only $r_{11}$ and $r_{21}$ are determined.

The determined $r_{11}$ at $\theta_L = 0.55$ is 0.62495 and 0.60542 for the smallest and the largest controlled mass fluxes, respectively, which shows a decay of 3.12 percent. Moreover, the determined $r_{21}$ at $\theta_L = 0.55$ is $-0.08351$ and 0.02043 for the smallest and the largest controlled mass fluxes, respectively, which shows a decay of 75 percent in its magnitude as well a sign change.

Overall, a wider picture of the interface resistivities is found for different temperatures of the interface and different mass fluxes based on the results from the 26-moment equations. This clearly showed that they could not be considered as constant values. All four interface resistivities changed with the liquid's temperature at the interface. At lower tem-

peratures, the magnitudes of all four resistivities were greater than their values at the higher temperatures.

The EV resistivities for the different mass fluxes showed they change with the mass flux. This means the LIT realm at the interface has been left because LIT connects the forces and fluxes linearly with the resistivities. This showed that the LIT assumption that connects the thermodynamic forces and fluxes linearly might need to be modified to consider non-equilibrium strengths effects at the interface.

## 6.2 Future Work

To further develop modelling of the phase interface, some future work can be done to continue this study. These developments in determining the interface resistivities can be done in the three main following sections

- Optimizing the MATLAB code
- Extracting the interface variables from the current solutions of the 26-moment equations
- Adding more non-linear terms or moments to the transport equations derived from the EV equation

The MATLAB code used in this research considered the same distance $\Delta x$ between the nodes in the system. It can be optimized by adding variable grid spacing that considers more nodes for the interface region than bulk phases.

Extracting the interface variables from the resolved solutions of the 26-moment equations more accurately can be another work in the future. For example, the exponential extrapolations can be used instead of the linear extrapolations that lead to the calculation error in larger mass fluxes in the forced evaporation process with two temperature boundaries. This exponential curve fitting will solve the problem of finding the complete sets

of interface resistivities from the forced evaporation process with larger controlled mass fluxes.

Also, most reliably, the 26-moment results in the bulk phases can be used to find the NSF solutions and extrapolate them to determine the required interface variables.

Finding the interface variables by choosing different interface locations, for instance, at $L_0$, could be helpful to check the possibility of determining symmetric off-diagonal resistivities.

Some future works could also be done about having the more detailed sets of the macroscopic equations. One possible thing that can be done is to add more non-linear terms to the current set of 26-moment equations to study the non-equilibrium effects at and in front of the interface in even higher resolutions that might affect the results.

Finally, According to the LIT, the interface resistivities should not change with the mass flux. However, it is found that the mass flux affects the resistivities values. As a result, this research concludes with a question of whether the LIT assumptions that connect the thermodynamics forces and fluxes linearly need to be modified to consider the effects of the non-equilibrium strength on the interface resistivities?

# Bibliography


[1] R. Hoyst, M. Litniewski, D. Jakubczyk, K. Kolwas, M. Kolwas, K. Kowalski, S. Migacz, S. Palesa, and M. Zientara. Evaporation of freely suspended single droplets: experimental, theoretical and computational simulations. *Reports on Progress in Physics*, 76(3):034601, 2013.

[2] R. Marek and J. Straub. Analysis of the evaporation coefficient and the condensation coefficient of water. *International Journal of Heat and Mass Transfer*, 44(1):39–53, 2001.

[3] I. W. Eames, N. J. Marr, and H. Sabir. The evaporation coefficient of water: a review. *International Journal of Heat and Mass Transfer*, 40(12):2963–2973, 1997.

[4] G. T. Barnes. Insoluble monolayers and the evaporation coefficient of water. *Journal of Colloid and Interface Science*, 65(3):566–572, 1978.

[5] T. Alty and C. A. Mackay. The accommodation coefficient and the evaporation coefficient of water. *Proceedings of the Royal Society of London. Series A-Mathematical and Physical Sciences*, 149(866):104–116, 1935.

[6] A. H. Persad and C. A. Ward. Expressions for the evaporation and condensation coefficients in the Hertz-Knudsen relation. *Chemical Reviews*, 116(14):7727–7767, 2016.

[7] Maurice Bond and Henning Struchtrup. Mean evaporation and condensation coefficients based on energy dependent condensation probability. *Physical Review E*, 70(6):061605, 2004.

[8] R. W. Schrage. *A Theoretical Study of Interphase Mass Transfer*. Columbia University Press, editor. Columbia University Press, 1953.

[9] C. A. Ward and D. Stanga. Interfacial conditions during evaporation or condensation of water. *Physical Review E*, 64(5):051509, 2001.

[10] G. Fang and C. A. Ward. Temperature measured close to the interface of an evaporating liquid. *Physical Review E*, 59(1):417, 1999.

[11] G. Fang and C. A. Ward. Examination of the statistical rate theory expression for liquid evaporation rates. *Physical Review E*, 59(1):441, 1999.

[12] Young-Ping Pao. Temperature and density jumps in the kinetic theory of gases and vapors. *The Physics of Fluids*, 14(7):1340–1346, 1971.

[13] J. R. Thomas. Temperature slip problem with arbitrary accommodation at the surface. *The Physics of Fluids*, 16(7):1162–1164, 1973.

[14] J. W. Cipolla Jr, H. Lang, and S. Km Loyalka. Kinetic theory of condensation and evaporation. II. *The Journal of Chemical Physics*, 61(1):69–77, 1974.

[15] K. Aoki and C. Cercignani. Evaporation and condensation on two parallel plates at finite Reynolds numbers. *The Physics of Fluids*, 26(5):1163–1164, 1983.

[16] M. M. Awad, A. S. Dalkilic, and S. Wongwises. A critical review on condensation heat transfer in microchannels and minichannels. *Journal of Nanotechnology in Engineering and Medicine*, 5(1), 2014.

[17] Vinicius Braga Leite, Denize Kalempa, and Irina Graur. Kinetic modelling of evaporation and condensation phenomena around a spherical droplet. *International Journal of Heat and Mass Transfer*, 166:120719, 2021.

[18] Alexander Felix Beckmann, Anirudh Singh Rana, Manuel Torrilhon, and Henning Struchtrup. Evaporation Boundary Conditions for the Linear R13 Equations Based on the Onsager Theory. *Entropy*, 20(9):680, 2018.

[19] Henning Struchtrup. *Thermodynamics and Energy Conversion*. Springer, editor. Springer, 2014.

[20] D. C. Venerus and H. C. Ottinger. *A Modern Course in Transport Phenomena*. Cambridge University Press, 2018.

[21] S. Kjelstrup, D. Bedeaux, E. Johannessen, and J. Gross. *Non-Equilibrium Thermodynamics for Engineers*. Amanda Yun, editor. World Scientific Publishing Co. Pte. Ltd., 2017.

[22] S. R. De Groot and P. Mazur. *Non-equilibrium Thermodynamics*. Dover Publication, editor. Dover Publication, 2013.

[23] D. Bedeaux. Nonequilibrium thermodynamics and statistical physics of surfaces. *ACADEMIA*, 1986.

[24] Maurice Bond. *Non-equilibrium Evaporation and Condensation*. Master's thesis, Masters thesis, University of Victoria, 2004.

[25] H. Struchtrup and A. Frezzotti. Macroscopic ModelsDerived from the Enskog Vlasov Equation. Derievation of the closed set of 26moments equations.

[26] J. W. Cipolla, H. Lang, and S. K. Loyalka. Kinetic theory of condensation and evaporation. II. *The Journal of Chemical Physics*, 61(1):69–77, 1974.

[27] D. Bedeaux, L. J. F. Hermans, and T. Ytrehus. Slow evaporation and condensation. *Physica A: Statistical Mechanics and its Applications*, 169(2):263–280, 1990.

[28] Signe Kjelstrup and Dick Bedeaux. *Non-equilibrium Thermodynamics of Heterogeneous Systems*. World Scientific, editor. World Scientific, 2008.

[29] G. Schmidt and H. Wenzel. A modified van der Waals type equation of state. *Chemical Engineering Science*, 35(7):1503–1512, 1980.

[30] Henning Struchtrup. *Macroscopic Transport Equations for Rarefied Gas Flows*. Springer, editor. Springer, 2005, pages 145–160.

[31] Nishanth Dongari, Ashutosh Sharma, and Franz Durst. Pressure-driven diffusive gas flows in micro-channels: from the Knudsen to the continuum regimes. *Microfluidics and Nanofluidics*, 6(5):679–692, 2009.

[32] Matthias Heinen and Jadran Vrabec. Evaporation sampled by stationary molecular dynamics simulation. *The Journal of Chemical Physics*, 151(4):044704, 2019.

[33] E. S. Benilov and M. S. Benilov. The Enskog–Vlasov equation: a kinetic model describing gas, liquid, and solid. *Journal of Statistical Mechanics: Theory and Experiment*, 2019(10):103205, 2019.

[34] A. Frezzotti, Paolo Barbante, and Livio Gibelli. Direct Simulation Monte Carlo applications to liquid-vapor flows. *Physics of Fluids*, 31(6):062103, 2019.

[35] Jose Maria Montanero and Andres Santos. Monte Carlo simulation method for the Enskog equation. *Physical Review E*, 54(1):438, 1996.

[36] Carlo Cercignani. *The Boltzmann Equation*. Springer, editor. Springer, 1988, pages 40–103.

[37] H. Struchtrup and A. Frezzotti. Grads 13 moments approximation for Enskog-Vlasov equation. In *AIP Conference*, number 1, page 10. AIP Publishing LLC, 2019.

[38] Stewart Harris. *An Introduction to the Theory of the Boltzmann Equation*. Courier Corporation, editor. Courier Corporation, 2004.

[39] Peter C. Riedi. *Thermal Physics: an Introduction to Thermodynamics, Statistical Mechanics and Kinetic Theory*. Macmillan International Higher Education, editor. Macmillan International Higher Education, 2016.

[40] Carlo Cercignani. *Rarefied Gas Dynamics: From Basic Concepts to Actual Calculations*. Cambridge University Press, editor, volume 21. Cambridge University Press, 2000.

[41] Francis Weston Sears, Gerhard L. Salinger, and John E. Lee. *Thermodynamics, Kinetic Theory, and Statistical Thermodynamics*. Addison-Wesley, editor. Addison-Wesley, 1975.

[42] Carlo Cercignani. Strong evaporation of a polyatomic gas. *Progress in Astronautics and Aeronautics*, 74:305–320, 1981.

[43] Carlo Cercignani, W. Fiszdon, and Aldo Frezzotti. The paradox of the inverted temperature profiles between an evaporating and a condensing surface. *The Physics of Fluids*, 28(11):3237–3240, 1985.

[44] Takeo Soga. A kinetic theory analysis of evaporation and condensation of a diatomic gas. *The Physics of Fluids*, 28(5):1280–1285, 1985.

[45] L. Boltzmann. Weitere studien über das wärmegleichgewicht unter gasmolekülen, sitzungs. akad. wiss. wein 66 (1872), 275–370; english: further studies on the thermal equilibrium of gas molecules. *Kinetic Theory*, 2:88–174, 1872.

[46] Anatoli Aleksandrovich Vlasov. Many particle theory and its application to plasma. *Arkiv Mat. Astr. Fys*, 1961.

[47] D. Enskog. The numerical calculation of phenomena in fairly dense gases. *Arkiv Mat. Astr. Fys*, 16(1):1–60, 1921.

[48] Pierre M. V. Rsibois, Marcel DeLeener, and M. F. DeLeener. *Classical Kinetic Theory of Fluids*. John Wiley and Sons, editors. John Wiley and Sons, 1977.

[49] Norman F. Carnahan and Kenneth E. Starling. Equation of state for nonattracting rigid spheres. *The Journal of Chemical Physics*, 51(2):635–636, 1969.

[50] J. E. Jones. On the determination of molecular fields. From the variation of the viscosity of a gas with temperature. *Proceedings of the Royal Society of London. Series A, Containing Papers of a Mathematical and Physical Character*, 106(738):441–462, 1924.

[51] Xipeng Wang, Simón Ramírez-Hinestrosa, Jure Dobnikar, and Daan Frenkel. The Lennard-Jones potential: when (not) to use it. *Physical Chemistry Chemical Physics*, 22(19):10624–10633, 2020.

[52] Sydney Chapman. VI. On the law of distribution of molecular velocities, and on the theory of viscosity and thermal conduction, in a non-uniform simple monatomic gas. *Philosophical Transactions of the Royal Society of London. Series A, Containing Papers of a Mathematical or Physical Character*, 216(538-548):279–348, 1916.

[53] Sydney Chapman. V. On the kinetic theory of a gas. Part II A composite monatomic gas: diffusion, viscosity, and thermal conduction. *Philosophical Transactions of the Royal Society of London. Series A, Containing Papers of a Mathematical or Physical Character*, 217(549-560):115–197, 1918.

[54] S. Reinecke and G. M. Kremer. Method of moments of Grad. *Physical Review A*, 42(2):815, 1990.

[55] Pierre Comon, Gene Golub, Lek-Heng Lim, and Bernard Mourrain. Symmetric tensors and symmetric tensor rank. *SIAM Journal on Matrix Analysis and Applications*, 30(3):1254–1279, 2008.

[56] Harold Grad. *Principles of the Kinetic Theory of Gases*. Springer, editor. Springer, 1958, pages 205–294.

[57] Harold Grad. On the kinetic theory of rarefied gases. *Communications on Pure and Applied Mathematics*, 2(4):331–407, 1949.

[58] Arnold Sommerfeld. *Lectures on Theoretical Physics*. Academic Press, editor. Academic Press, 1956.

[59] V. Torrilhon. Modeling Nonequilibrium Gas Flow Based on Moment Equations. *Annual Review of Fluid Mechanics*, 2016.

[60] E. C. Aifantis and J. B. Serrin. The mechanical theory of fluid interfaces and Maxwell's rule. *Journal of colloid and interface science*, 96(2):517–529, 1983.

[61] Göran Bergqvist and Paul Lankinen. Algebraic and differential Rainich conditions for symmetric trace-free tensors of higher rank. *Proceedings of the Royal Society A: Mathematical, Physical and Engineering Sciences*, 461(2059):2181–2195, 2005.

[62] Randall J. LeVeque. *Finite difference methods for ordinary and partial differential equations: steady-state and time-dependent problems*. SIAM, editor. SIAM, 2007.

[63] MATLAB. *version 9.10 (R2021a)*. MATLAB, editor. The MathWorks Inc., Natick, Massachusetts, 2021.

[64] Lars Onsager. Reciprocal relations in irreversible processes. i. *Physical Review*, 37(4):405, 1931.

[65] Lars Onsager. Reciprocal relations in irreversible processes. II. *Physical Review*, 38(12):2265, 1931.